This is to certify that the
dissertation entitled
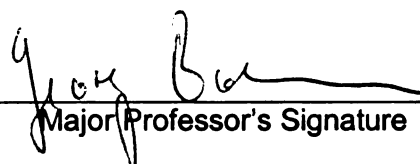
HIGH-PRECISION MASS MEASUREMENTS OF N ≈ Z ≈ 34
NUCLIDES FOR RP-PROCESS SIMULATIONS AND
DEVELOPMENTS FOR THE LEBIT FACILITY

presented by

Joshua J. Savory

has been accepted towards fulfillment
of the requirements for the

_____Ph.D_____   degree in   _____Physics and Astronomy_____

_____
Major Professor's Signature

_____8 - 2 0 - 2 0 0 9_____

Date

MSU is an Affirmative Action/Equal Opportunity Employer

PLACE IN RETURN BOX to remove this checkout from your record.
TO AVOID FINES return on or before date due.
MAY BE RECALLED with earlier due date if requested.

DATE DUE	DATE DUE	DATE DUE

HIGH-PRECISION MASS MEASUREMENT OF $N \approx Z \approx 34$ NUCLIDES FOR RP-PROCESS SIMULATIONS AND DEVELOPMENTS FOR THE LEBIT FACILITY

By

Joshua J. Savory

A DISSERTATION

Submitted to
Michigan State University
in partial fulfillment of the requirements
for the degree of

DOCTOR OF PHILOSOPHY

Physics and Astronomy

2009

ABSTRACT

HIGH-PRECISION MASS MEASUREMENT OF N ≈ Z ≈ 34 NUCLIDES FOR RP-PROCESS SIMULATIONS AND DEVELOPMENTS FOR THE LEBIT FACILITY

By

Joshua J. Savory

The Low Energy Beam and Ion Trap (LEBIT) facility at the National Superconducting Cyclotron Laboratory (NSCL) performs high precision mass measurements of rare isotopes. Within this work mass measurements in the $N \approx Z \approx 34$ region were performed by Penning trap mass spectrometry. Mass measurements of nuclei in this region are important for understanding the rp process, a driving mechanism behind type I x-ray bursts. The masses measured were ^{68}Se, ^{70}Se, ^{70m}Br, and ^{71}Br and experimental uncertainties ranging from 0.5 keV for ^{68}Se to 15 keV for ^{70m}Br were achieved. Using the LEBIT results along with theoretical Coulomb displacement energies [1] more reliable mass predictions were obtained for ^{70}Kr and ^{71}Kr. The new and improved data were used as input for rp process network calculations. An increase in the effective lifetime of the waiting point nucleus ^{68}Se was observed, thus confirming it as a large source of delay in the rp process. More precise information was also obtained on the luminosity during a type I x-ray burst and on the distribution of the final abundances after a burst.

Beam manipulation and detection are an important part of the high precision mass measurement process performed at the LEBIT facility. Several upgrades to the LEBIT facility for improved beam quality, control, and observation are presented. The properties of ion pulses ejected from the facility's beam cooler and buncher were investigated and optimized for improved contaminant ion detection and removal.

To increase the ion detection efficiency after the Penning trap a multichannel plate detector was implemented in a Daly detector configuration. These upgrades were instrumental in moving the LEBIT facility towards measurements of nuclei with lower yields and higher levels of contaminant.

ACKNOWLEDGMENTS

First off, I would like to thank all of the staff at the NSCL who helped me to realize the research presented in this work. Without the expertise of the cyclotron operators and the A1900 group the rare isotope beams necessary for the completion of this experiment couldn't have been produced.

In the preparation of this thesis, special thanks goes to Ania Kwiatkowski and Ryan Ringle who read through it numerous times along with Pete Schury and V. A. Shchepunov who performed several important simulations for this work. I would also like to thank my fellow graduate students and close friends (Dan Brown, Jon Deluater, Greg Pang, Micha Kilburn, and Josh Veazey) who provided the moral support and camaraderie necessary to complete this project. On a personal note, I am extremely grateful to my parents who instilled me with a sense of curiosity and taught me the importance of hard work and to my wife for her undying support and patience.

Most importantly, I would like to acknowledge the efforts of all members of the LEBIT group both past and present. I would also like to express my sincere gratitude to Stefan Schwarz for taking the time to answer all my technical questions and to Dave Morrissey for the excellent career advice. Finally, I would like to thank my advisor Georg Bollen for teaching me what it means to be a researcher and encouraging me to reach beyond my goals.

Contents

List of Tables

List of Figures

Images in this dissertation are presented in color.

Chapter 1

Introduction

One of the important challenges for today's scientists is understanding the origin of the elements. Specifically, in the February 2002 issue of *Discover Magazine* understanding "the precise origin of the heavier elements from iron to uranium" was listed as one of the top 11 unanswered questions in physics [19]. In 1957, three nucleosynthesis processes (the slow neutron capture process or s process, the rapid neutron capture process or r process, and the proton process or p process) were proposed by Burbidge, Burbidge, Fowler, and Hoyle (BBFH) to explain the abundance of these elements [20]. The s process moves along the valley of stability and is believed to produce approximately half the abundance of the elements heavier than iron. The r process occurs in neutron-rich nuclei, but the exact location and contribution of this process is still under debate. Combined these two capture processes can explain the production of most heavy nuclei; however neither can explain the abundance of some rare proton-rich nuclei, called the p-nuclei, observed in nature. The creation of these nuclei was attributed to a then unknown p process by BBFH.

Two possible sites for a p process are core-collapse supernovas and type I x-ray bursts. During core-collapse supernovae, heavy proton-rich nuclei ($70 < A < 200$) are believed to be produced through photodisintegration reactions on seed nuclei from an r process or s process [21]. This series of photodisintegration reactions is

1

referred to as the γ process and can produce all of the p-nuclei except for ^{92,94}Mo and ^{96,98}Ru. Another possible production site for some of the p-nuclei is during type I x-ray bursts where quantifiable amounts of ^{92,94}Mo and ^{96,98}Ru could be produced, but the ejection mechanism from such a burst is still in question [22]. In these bursts heavy nuclei are created through a series of proton capture reactions and β decays in what is known as the rapid proton capture process or rp process [23–25]. The possible contributions of a type I x-ray bursts to galactic nucleosynthesis could be determined through burst simulations provided that the required input data is available. Possibly more significant is the information that could be gained about the structure and location of neutron stars through the comparisons of simulated and observed type I x-ray bursts. The goal of the measurements presented in this dissertation was to improve our understanding of the rp process and type I x-ray bursts through high-precision mass measurements of proton-rich nuclei in the N $\approx$ Z $\approx$ 34 region.

1.1 Type I X-Ray Bursts

A binary star system consisting of a neutron star accreting matter from an expanded companion star and releasing x-rays is known as an x-ray binary. An artistic representation of a binary system and the material transfer between the two stars is shown in Figure 1.1. The luminosity of this system is due to the gravitational potential energy released as the accreted matter falls onto the neutron star's surface. In an accreting neutron star binary system, a thermonuclear burning of the accreted layer may occur if the rate of accretion is $\lesssim 10^{-8}$ solar masses per year and if the accreted material is rich in hydrogen and helium [7]. The resulting thermonuclear explosion is known as a type I x-ray burst and is marked by an observable increase in the emitted x-ray luminosity as a function of time, often called the light curve. The luminosity emitted during a burst ranges from 10^{37}-10^{39} erg/s with burst durations on the order of 10-100 s and repetitions on a time scale of hours or days.
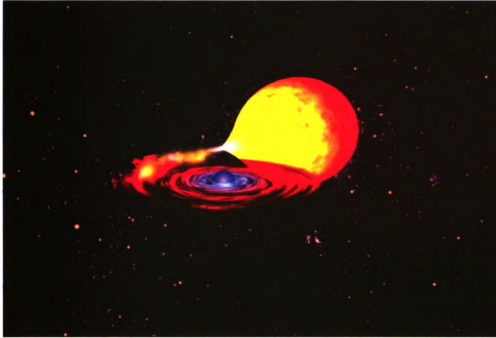
Figure 1.1: An artistic view of an accreting neutron star binary system from which an x-ray burst can originate. Image credit and copyright: NASA.

Type I x-ray bursts are initiated when the temperature and the density in the accreted layer on a neutron star become high enough to favor the triple alpha reaction and allow a breakout from the hot CNO cycle. The burst starts with a burning of helium in a series of (α,p) (p,γ) reactions in what is known as the αp process. As the burst proceeds towards heavier nuclei, alpha capture becomes less favorable due to the Coulomb barrier. At this point, the burst continues through a rapid burning of hydrogen in a series of (p,γ) reactions or proton captures and β decays known as the rp process [24]. The rp process proceeds along a proton-capture chain until a nucleus is reached that has a photodisintegration reaction rate significantly larger than its proton capture reaction rate. The burst can proceed past this point only through a β decay or a double proton capture. The nuclei at which this occur are known as the "waiting points" of the burst.

The time it takes to proceed beyond a waiting point nucleus, the effective lifetime, determines the extent to which the waiting point alters the final abundance distribu-

tion and the observable x-ray light curve of the burst. In the $N \approx Z \approx 34$ region the most prominent waiting point nuclei are ^{64}Ge ($T_{1/2} = 63.7$ s), ^{68}Se ($T_{1/2} = 35.5$ s), and ^{72}Kr ($T_{1/2} = 17.6$ s) due to their relatively long β decay half-lives. These nuclei along with a proposed path for the capture processes involved in a type I x-ray burst are shown in Figure 1.2. The effective lifetimes of ^{64}Ge, ^{68}Se, and ^{72}Kr were previously shown to have a strong impact on the shape and the duration of the light curve emitted during a type I x-ray burst [1,7,24,25]. The long lifetimes of these nuclei are a likely explanation for observed light curves with an extended burst duration ($>$ 10 s) or tail. Such light curves are used as an indicator for a burst with an initial hydrogen content in the neutron star's surface sufficient to fuel an rp process beyond $A = 64$.

In the most powerful bursts the maximum expected luminosity, the Eddington luminosity, is reached. The Eddington luminosity (F_{edd}) of a burst is defined as the radiation flux at which the inward gravitational force is balanced by outward radiation force and given by

$$F_{edd} = \frac{1}{4\pi D^2} \frac{4\pi GMc}{0.2(1 + X)} \sqrt{1 - \frac{2GM}{Rc^2}} \qquad (1.1)$$

where G is the gravitational constant, M is the mass of the neutron star, X is the initial hydrogen mass fraction, c is speed of light, D is the distance between the neutron star and the observer, and R is the radius of the neutron star [26]. During bursts where the Eddington luminosity is reached the excess energy is converted into kinetic energy, which causes an expansion in the outer layers of the neutron star. These highly luminous bursts are known as photospheric radius expansion (PRE) bursts. Previously observed PRE bursts were used to extract important qualities about the involved neutron stars [27,28]. Through an analysis of PRE burst's light curves from the low-mass x-ray binary 4U 1636-536, the distance to its neutron star was determined [28]. In this analysis variations in the burst's observed peak flux were attributed to changes in the composition of the neutron star's crust. The brightest
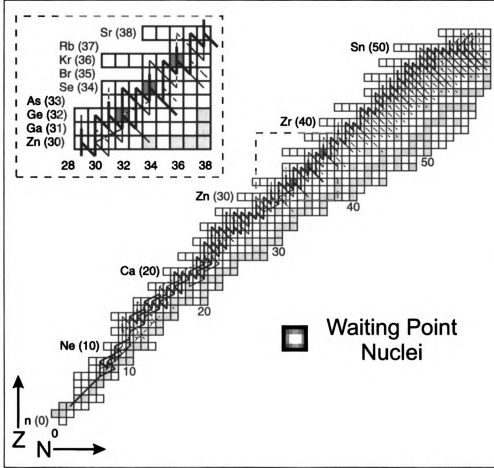
Figure 1.2: Proposed capture path of a type I x-ray burst. In the inset, a close up of the $N \approx Z \approx 34$ region is shown, and the waiting point nuclei are highlighted.

bursts were assumed to correspond to a crust composed purely of helium ($X = 0$) whereas the faintest burst were associated with a crust composed of a solar fraction of hydrogen and helium ($X = 0.7$). In another binary system, the EXO 07482676 neutron star's equation of state was determined using the luminosity, redshift of O and Fe absorption lines, and the ratio of the thermal flux and the colour temperature from observed PRE bursts [27]. In this determination, one the largest uncertainties was the value of hydrogen mass fraction (X) which was permitted to vary between $0 \leq X \leq 1$ [27]. Both analyses [27,28] would benefit from a quantitative determination of the PRE burst's initial hydrogen content.

Through comparisons of observed and simulated type I x-ray burst light curves,

a quantitative interpretation of burst tails in terms of the initial hydrogen content may be possible. In general, a reliable modeling of the rp process is also important to predict the composition of the burst's ashes. This composition is required to perform crust model calculations [29] and to predict possible contributions to galactic nucleosynthesis from small amounts of matter ejected in some burst models [22]. To properly model the rp process and to perform the quantitative analysis necessary to determine the initial hydrogen content of a type I x-ray burst, a precise knowledge of the nuclear physics of the reaction network is required.

A reliable modeling of burst tails depends very sensitively on the effective lifetime of the waiting point nuclei ^{64}Ge, ^{68}Se, and ^{72}Kr and thus also on their proton separation energies ($S_{(N,Z)}$). During the explosion, an equilibrium develops between proton capture and photodisintegration. The ratio of these rates determines to a large extent the degree to which the double proton capture channel can bypass the β decay of the waiting point nuclei. The importance of proton separation energies in modeling the rp process can be seen by looking at the abundance ratio of the two consecutive nuclei (N, Z) and (N, Z+1) in a capture chain where an equilibrium has developed between proton capture and photodisintegration. This ratio is given by the Saha equation

$$\frac{Y_{(N,Z+1)}}{Y_{(N,Z)}} = \rho \frac{G_{(N,Z+1)}}{2G_{(N,Z)}} \left(\frac{A_{(N,Z+1)}}{A_{(N,Z)}} \frac{2\pi\hbar^2}{m_\mu k_b T} \right)^{3/2} exp\left(\frac{S_{(N,Z+1)}}{k_b T} \right) \qquad (1.2)$$

where Y is the abundance, ρ is the proton density, G is the partition function, A is the mass number, M_μ is the atomic mass unit, k_b is the Boltzmann constant, and T is the temperature [30]. As shown in the Saha equation, this abundance ratio has an exponential dependence on the nuclei's proton separation energy. To determine the proton separation energy, mass measurements of both nuclei involved in the reaction are required. Masses are also important in calculating the resonance energy of an excited state which is another important parameter in type I x-ray burst models, especially for nuclei with a low density of states [30]. In order to reliably model the

rp process mass measurements of $^{64-66}$Ge, $^{68-70}$Se, and $^{72-74}$Kr with uncertainties on the order of 10 keV or less [25, 30] are necessary.

1.2 Mass Measurements of Rare Isotopes Important for the rp Process

The mass measurements of nuclei in the $N \approx Z \approx 34$ region required to model the rp process are difficult due to their proximity to the proton-dripline and their low production rates. Despite this fact, multiple mass measurements of nuclei in this region have been performed [5, 6, 8–14, 31–35]. The techniques used to perform these measurements can be divided into two categories: indirect and direct measurements. The difference being that indirect measurements, such as decay or reaction measurements, provides a mass difference between the initial and final nuclei, whereas direct measurement, such as cyclotron frequency or time-of-flight measurements, provides a mass ratio of two nuclei.

1.2.1 Indirect Measurements

For a long time, indirect mass measurements were the most prevalent way of measuring masses. The most common indirect mass measurement is to measure the energy of the particles emitted from a decaying nucleus. Through such a measurement the Q value of the decay can be obtained. In the $N \approx Z \approx 34$ region, the Q value of several nuclei were determined through β^+ spectrum end-point measurements at Yale [13] and at Argonne National Laboratory [9, 14]. To determine the mass of a nucleus from such an indirect measurement the mass difference to a nucleus with a well known mass is required. For nuclei far from stability the chain of measurements required to reach a well-known nucleus may result in a large cumulative error. However, for extremely short-lived ($\ll 1\ \mu s$) or unbound nuclei, such as ^{69}Br, indirect measurements

7

are often the only possibility. A breakup reaction experiment was in fact conducted at the National Superconducting Cyclotron Laboratory (NSCL) to measure the mass of ^{69}Br [36]. In this experiment, the Q value of the ^{68}Se(p,γ)^{69}Br reaction was determined by a complete kinematic reconstruction of the ^{69}Br decay products.

1.2.2 Direct Measurements

Direct mass measurements are preferable as they avoid the large cumulative errors often associated with indirect measurements. Time-of-flight mass measurements are one of the more popular direct mass measurement techniques as the masses of short-lived nuclei can be measured quickly to avoid substantial decay losses. In this method, a high precision measurement of an ion's time-of-flight, distance traveled, and energy are combined to calculate the mass. The precision obtained in a time-of-flight measurement is directly related with the length of the ions' flight path and typically the resolution is on the order $\frac{\delta m}{m} = 10^{-4}\text{-}10^{-6}$ [37]. In the $N \approx Z \approx 34$ region, time-of-flight mass measurements have been performed using a cyclotron [10,31] and a mass spectrometer [8,12] at GANIL, and a storage ring [11] at GSI.

The highest precision mass measurements are performed at present with Penning trap mass spectrometers. This method (used in this work) is based on a high precision measurement of an ion's cyclotron frequency, $\omega_c = qB/m$, in a strong and well known magnetic field B where q and m are the ion's charge and mass, respectively. Mass measurements of radioactive isotopes performed with Penning traps have reached accuracies of $\frac{\delta m}{m} = 10^{-8}$ and better [38,39]. With reduced precision, measurements have been performed recently on nuclei with half-lives as short as 8.8 ms [40]. With stable isotopes, Penning trap mass measurements with precisions as high as $\frac{\delta m}{m} = 10^{-11}$ have been achieved [41]. For this dissertation, high-precision mass measurements of the $N \approx Z \approx 34$ nuclei ^{68}Se, ^{70}Se, ^{70m}Br and ^{71}Br were performed by Penning trap mass spectrometery with the Low Energy Beam and Ion Trap (LEBIT) facility [4]. Previously Penning trap mass measurements in this region have been performed at

the Canadian Penning Trap (CPT) [32], ISOLTRAP [33–35], and also at LEBIT [5].

1.3   Outline for this Thesis

The two aspects of this dissertation are to present Penning trap mass measurements of ^{68}Se, ^{70}Se, ^{70m}Br, and ^{71}Br and to discuss the impact of these results on type I x-ray burst network calculations. The chapters of this dissertation are organized in the following manner: In Chapter 2, the design and operation of the LEBIT facility is presented. The experimental procedures and results of the experiment are given in Chapter 3. In Chapter 4, rp process simulations and the impact of the measurements on these simulations will be discussed. In addition to this part of the work, several technical aspects were explored to improve the overall performance and operation of the LEBIT facility. Chapter 5 focuses on the design and operation of a multichannel-plate detector implemented in a Daly detector configuration for improved ion detection efficiencies. In Chapters 6 and 7, the optimization of the facility's beam cooler and buncher and the simulation of a multipass time-of-flight mass spectrometer for improved contaminant ion suppression capabilities is presented. The final chapter provides a summary of this dissertation.

Chapter 2

The Low Energy Beam and Ion Trap Facility

The Low Energy Beam and Ion Trap (LEBIT) facility was constructed to perform high-precision mass measurements of rare isotopes produced at the National Superconducting Cyclotron Laboratory (NSCL) at Michigan State University. At the NSCL (shown in Figure 2.1) radioactive beams are created by projectile fragmentation. In the electron cyclotron resonance (ECR) ion source a stable primary ion beam is created. The two cyclotrons shown in Figure 2.1, the K500 and the K1200, are coupled to accelerate this beam to a kinetic energy of approximately 80-150 MeV/u. Rare isotopes are produced by fragmentation of this primary beam in a thin beryllium target. The ions of interest are then separated in-flight from the other primary beam frag-
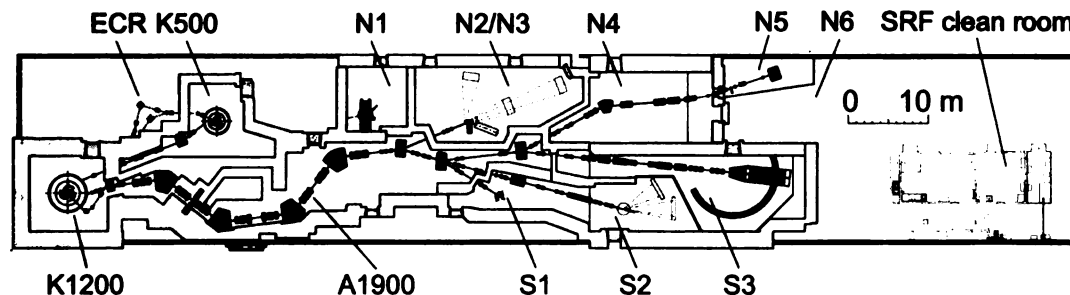
Figure 2.1: Overview of the National Superconducting Cyclotron Laboratory's experimental area. LEBIT is located in the N4 and N5 vaults.

mentation products in the A1900 fragment separator [42] by their magnetic rigidity and then continue on at high velocity to one of the experimental vaults (S1-3, N1-6). The LEBIT facility (shown in Figure 2.2) is located in the N4 and N5 vaults.

LEBIT is at present the only facility that can perform Penning-trap mass measurements of rare isotopes produced by projectile fragmentation [5, 38, 39, 43]. Most high-precision Penning-trap measurements are carried out at isotope-separation-online (ISOL) facilities where low-energy high-quality rare isotope beams are extracted from a thick target. However, the use of rare isotopes produced by projectile fragmentation is advantageous as all isotopes lighter than the projectile are created in a chemically independent manner without decay losses (due to the production technique); thus, the LEBIT facility can access isotopes that are difficult to obtain at other facilities. In order for the LEBIT facility to perform high-precision mass measurements of the high-energy beams produced at the NSCL, a gas stopping technique is employed to slow down and capture the fast ions.

Figure 2.2 gives an overview of the LEBIT facility, the main components of which are a gas stopping station [5, 44], a beam cooler and buncher [45], and a high-precision Penning-trap mass spectrometer [46, 47]. The gas stopping station's purpose is to efficiently stop and thermalize the high-energy rare isotope beam [44]. The beam cooler and buncher converts this continuous ion beam into a low-emittance pulsed beam [45]. The Penning-trap mass spectrometer is used to capture these ion pulses and to determine their mass through a measurement of the ions' cyclotron frequency [5, 38, 48–50].

An electrostatic lens and deflector system is used transport the ions between the main components of the LEBIT facility. Along the facility's beam line are several beam observations boxes (BOBs) which contain different charged particle detectors i.e. Faraday cups (in BOBs 1-3,5,&6), micro-channel plate detectors (in BOBs 3,5,&6), silicon detectors (in BOBs 1,4,&6), and a channeltron (in BOB 6). For beam tuning and test measurements a test ion source [51] is available, which can produce stable
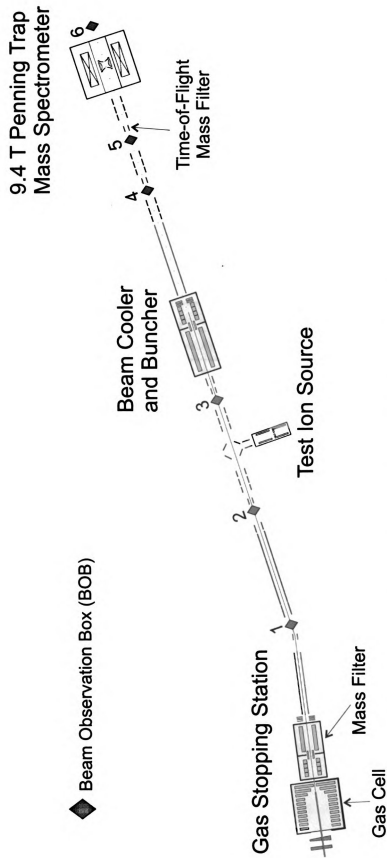
Figure 2.2: Schematic layout of the LEBIT facility.

alkali (Na, K, Rb, Cs) and noble gas (Ne, Ar, Kr) beams.

With the exception of a few parameters the LEBIT facility is fully remote controlled using a LabVIEW-based server along with a Programable Logic Controller hardware interface. A description of this control system and several upgrades implemented during the course of this work are presented in Appendix A.

2.1   The Gas Stopping Station
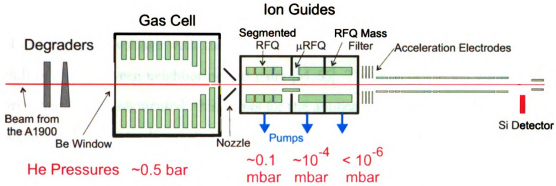
Figure 2.3: Schematic configuration of the gas stopping station.

The conversion of the high energy rare isotope beam produced at the NSCL into a thermalized low energy beam necessary for capture in the LEBIT Penning trap is made in the facility's gas stopping station (Figure 2.3). Before stopping these ions in the gas cell their energy is reduced to a few MeV/u. This is accomplished by passing the beam through variable thickness glass plate degraders. In addition, a wedge shaped degrader placed at the dispersive focus of a magnetic system is used to reduce the beam's energy spread [52, 53]. The beam's energy is further degraded as the ions enter the gas cell through a 0.5 mm thick beryllium window.

The gas cell itself consists of a 51 cm long chamber that is typically filled with 500 mbar of ultra high-purity helium gas. Once in the gas cell, the excess kinetic energy of the incoming ions is removed by collisions with the helium gas [53]. During the stopping process the ions undergo charge exchange reactions with the helium

gas, but they will only reach a 1+ or 2+ charge state due to helium's high first ionization energy. The ions are extracted from the gas cell by the combination of an electric gradient created by a set of electrodes inside the chamber and helium gas flow through a nozzle located at the end of the gas cell.

The sections following the gas cell have the purpose to transport the ions from the high pressure region directly after the gas cell into the ultra-high vacuum (UHV) system of LEBIT. This is achieved by the combination of a radio frequency quadrupole (RFQ) ion guide with a differential pumping system that was discussed in detail in [54]. In an RFQ ion guide, radial confinement is provided through the application of an oscillating voltage with the same amplitude and frequency but with a phase shift of $180°$ between neighboring rod pairs [54, 55]. The rods of the ion guide in the first chamber are segmented, this allows for the application of a DC voltage along the segments in order to drag ions through this intermediate pressure region with $P \approx 10^{-1}$ mbar. Between the first and second chamber a small RFQ (μRFQ) is used to restrict the gas flow and efficiently transport ions into the next section of the ion guides located in two vacuum chambers where pressures of less then 10^{-5} mbar and 10^{-7} mbar are achieved. This ion guide section can be operated as an RFQ mass filter [56]. Mass selection is accomplished by applying the appropriate combination of DC and RF quadrupole fields [57]. With this system a mass resolving power of approximately $\frac{m}{\Delta m} = 50$ with minimal losses is achievable. Mass filter operation is used to suppress unwanted contaminants (mostly stable molecular ions) that are produced in the gas cell in addition to the desired ions. This separation is necessary in order to achieve the high purity beams required to perform high-precision mass measurements in the Penning trap. Radioactive ions transported through the mass filter can be detected by their β decay after stopping on a retractable silicon detector. Mass scans of the ion guide performed with observation of the beam on this detector have proven to be very useful for identifying the isotope of interest's form (atomic or molecular) and charge state. After the RFQ mass filter, a set of electrodes were used to accelerate

the ions to a kinetic energy of 5 keV and to transport the beam through the shielding wall into a low background area.

2.2   The RFQ Beam Cooler and Buncher

Beam Cooler and Buncher
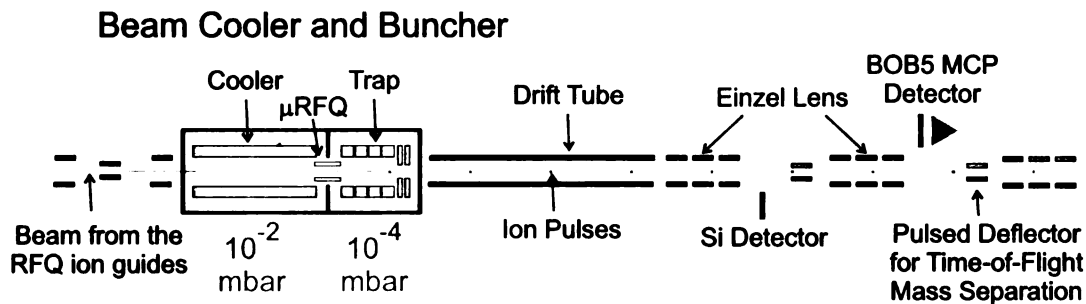
Figure 2.4: Schematic diagram of the LEBIT beam cooler and buncher along with the beam transport system that can be operated as a time-of-flight mass separator.

After leaving the gas cell and ion guides the beam enters a beam cooler and buncher. The purpose of the beam cooler and buncher (Figure 2.4) is to convert the continuous beam leaving the gas stopping station into a low-emittance pulsed beam [45,51,58] for capture in the Penning trap. The beam cooler and buncher is a gas-filled RFQ ion trap operated similarly to the ion guides discussed in the previous section. The 5 keV beam from the gas stopping station is electrostatically decelerated to about 10 eV before entering the beam cooler and buncher. In the cooler section, the ions lose energy through collisions with a buffer gas to prepare them for capture in the subsequent trap section. The gas pressure in the cooler section is regulated using a PID loop and an electromagnetic solenoid valve. The cooler section can be filled with helium or neon gas and is typical operated around 10^{-2} mbar. Using neon as a buffer gas and with a sufficiently high energy of the incoming beam allows collision induced dissociation (CID) of molecular ions, that is, a breaking apart of the contaminant and radioactive molecular ions into their constituents [59]. The ions surviving the cooler section are transported to the buncher section by a small RFQ (μRFQ) that serves to restrict the gas flow between the two sections.
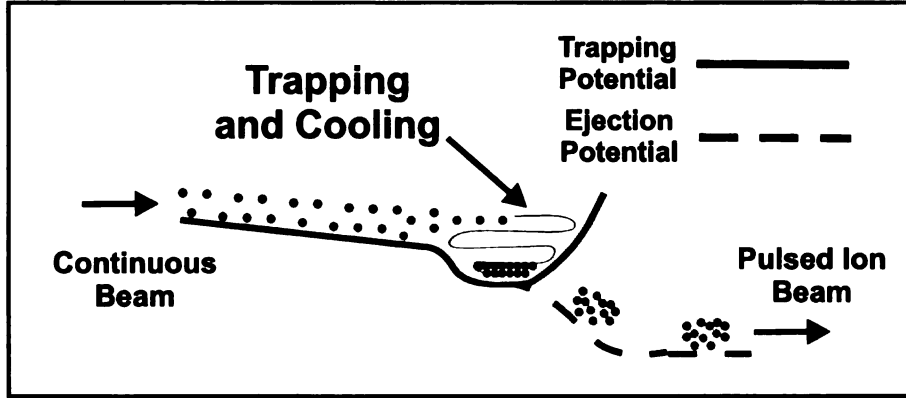
Figure 2.5: Schematic depicting the operation of the LEBIT beam cooler and buncher.

The buncher section contains a linear RFQ ion trap, which again consists of four RF electrodes this time surrounded by a tube segmented into 7 cylindrical electrodes. Ions entering the trap are confined radially by the oscillating voltages applied to the RF electrodes and axially by a DC potential well created by applying the appropriate voltages to the cylindrical trap electrodes. A separate helium gas inlet allows the buffer gas pressure in the buncher section to be adjusted; typically a pressure of 10^{-4} mbar is used. In the trap, ions are stored and cooled to thermal velocities by the buffer gas. To minimize the energy of the stored ions even further the electrodes of the LEBIT beam cooler and buncher can be cooled with LN_2 to attain temperatures between 70 K < T < 300 K depending on the location of the electrode. By switching the last trap electrodes to a lower voltage the ions can be ejected from this linear trap; this process is illustrated in Figure 2.5. After leaving the trap ion pulses are accelerated to a kinetic energy of 2 keV by a set of acceleration electrodes. A detailed study of ion pulses ejected from the LEBIT beam cooler and buncher was been performed as part of this work and will be discussed in Chapter 6.

The beam transport system from the beam cooler and buncher to the Penning trap consists of a pulsed drift tube and deflector along with several focusing and steering elements. The pulsed drift tube is used to fine tune the energy of the ion pulses for optimal capture in the Penning trap. A pulsed deflector, located approximately two
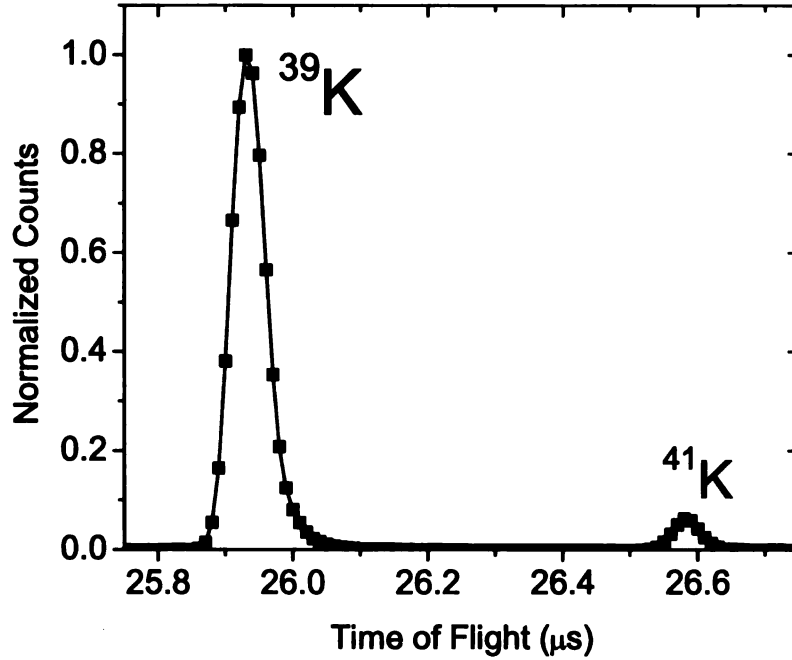
Figure 2.6: Pulses observed on the BOB5 MCP detector for ^{39}K and ^{41}K ions. A mass resolving power of approximately 200 was achieved in this case.

meters after the beam cooler and buncher, is used as a time-of-flight mass filter. Selection is accomplished by applying a deflecting voltage to one of the steering electrodes that is only switched off for a short time when the ion species of interest arrives. The properties and mass distribution of ion pulses entering the pulsed deflector can be measured at BOB5 (see Figure 2.2) by means of a micro-channel plate (MCP) detector. Figure 2.6 shows typical ion pulses observed on this MCP detector containing ^{39}K and ^{41}K ions. Typically, a pulse width of 50 ns can be achieved leading to a mass resolving power of about 200. Ions that are transmitted through the time-of-flight mass filter are focused by a final Einzel lens before entering the Penning-trap mass spectrometer.

2.3 The Penning Trap Mass Spectrometer
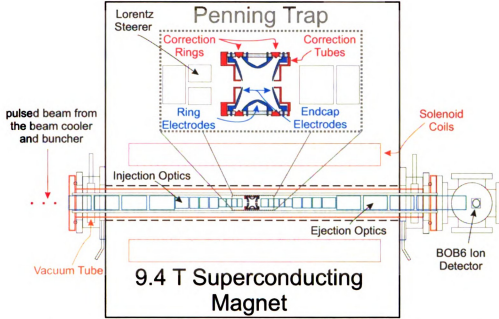
Figure 2.7: Layout of the LEBIT Penning-trap mass spectrometer. The inset shows **an** enlarged view of the trap electrodes.

The LEBIT Penning-trap mass spectrometer [46, 47], shown in Figure 2.7, can be used to determine the mass of a trapped ion to a high precision by measuring its cyclotron frequency, $\omega_c = qB/m$. The trap consists of a small set of electrodes mounted in a vacuum tube located in the room-temperature, horizontal bore of a solenoidal superconducting magnet. To determine an ion's mass accurately from the measured cyclotron frequency a highly homogenous magnetic field with minimal non-linear fluctuations is required. The spectrometer's superconducting magnet was built by Cryomagnetics Inc. and provides a magnet field strength of B = 9.4 T with a homogeneity on the order of 10 ppm over a 210 cm^3 volume with an average field decay of about $9.4 \cdot 10^{-8}$ T/h. The magnet also contains a set of Gabrielse coils [60] to nullify the effects of any external field changes on the central field strength. To improve the stability of the magnetic field further additional measures were taken. The natural decay of the magnetic field is compensated by slowly ramping a current through a pair of copper wires wound around the vacuum tube. Effects of external

pressure changes on the liquid-gas equilibrium of the helium bath and thus on the magnetic field strength are minimized by stabilizing the helium bath's pressure using a precision barometer and an electromagnetic value controlled by a PID loop.

Located at the entrance to the solenoidal magnet are the Penning trap's injection optics. These tube shaped electrodes are used to decelerate incoming ions to the eV level as they move towards the trap electrodes. Directly before the Penning trap the ions pass through a four-fold segmented cylindrical electrode named the "Lorentz" steerer [61]. This steerer is used to quickly prepare ions for measurement in the trap by moving them off axis. The Penning trap consists of two hyperbolic endcap electrodes and a segmented ring electrode as shown in Figure 2.7. In the center of each endcap electrode is a 4 mm hole that allows ions to enter and to exit the trap. As ions enter the central trapping region the voltage on the endcap electrodes is switched to create a DC potential well. Together with the magnetic field this provides ion confinement in the trap. The azimuthal ring electrode is divided into 8 segments, to allow the application of an RF voltage and the excitation of an ion's radial motion. The correction ring and tube electrodes minimize the effects of higher-order field contributions from the endcaps' holes and the finite extent of the electrodes. The voltage on the endcap electrodes can also be switched to create an extracting electric field to eject ions from the trap. The Penning trap's ejection optics transport ions from the Penning trap to BOB6 (see Figure 2.7). In BOB6, the ions' time of flight relative to their ejection from the Penning trap can be determined by detecting these ions on either a micro-channel plate (MCP) detector arranged in a Daly configuration [62] or a channeltron. Ion extraction and time-of-flight measurements are the basis of the time-of-flight ion-cyclotron-resonance (TOF-ICR) detection technique [48, 49] used at LEBIT for the determination of an ion's cyclotron frequency. This technique is particularly well suited for the measurement of short-lived radioactive ions.
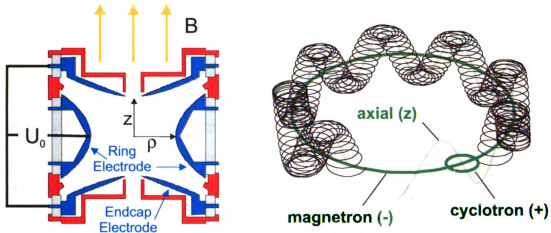
Figure 2.8: Schematic of a Penning trap (left) and illustration of a trapped ion's motion (right).

2.3.1 Mass Determination in a Penning Trap

Penning-trap mass spectrometry has been studied for over thirty years and the physics behind it is well understood [48,49,63,64]. The purpose of this section is to provide a brief introduction to this field and to present the information pertinent to Penning-trap mass measurements performed as part of this work.

Ions confined in a Penning trap move in a superposition of a homogeneous magnetic field and an axial quadrupole potential created by the electrode configuration shown in Figure 2.8. The three dimensional motion of an ion stored in a Penning trap (Figure 2.8) is composed of an axial oscillation ω_z between the endcaps and a revolution perpendicular to the magnetic field consisting of a fast reduced cyclotron motion ω_+ and a slow magnetron motion ω_-. An ion with a mass m and charge q performs a harmonic oscillation in the axial direction with a frequency:

$$\omega_z = \frac{qU_0}{md^2} \tag{2.1}$$

where $d = \sqrt{\rho^2/4 + z^2/2}$ is the characteristic dimension of the trap (Figure 2.8) and U_0 is the potential difference between the endcap and ring electrodes. The frequencies

of the two radial motions are given by the expression:

$$\omega_{\pm} = \frac{\omega_c}{2} \pm \sqrt{\frac{\omega_c}{4} - \frac{\omega_z}{2}} \qquad (2.2)$$

where ω_c is the cyclotron frequency of the ion. At this point, it is important to note that with a measured value for the cyclotron frequency $\omega_c = qB/m$ and precise knowledge of the magnetic field strength B and integer charge of the ion q, the mass of an ion m can be determined. The pure cyclotron frequency of ion can also be obtained by summing its reduced cyclotron and magnetron frequencies:

$$\omega_c = \omega_+ + \omega_- \qquad (2.3)$$

Another useful relationship is that an ion stored in a Penning trap with a strong magnetic field and a low electrostatic trapping potential will have a reduced cyclotron frequency that is much larger than its magnetron frequency, so that

$$\omega_+ \gg \omega_z \gg \omega_- \qquad (2.4)$$

This inequality is important in differentiating between ions leaving the trap with a pure magnetron motion versus a pure reduced cyclotron motion, as used in LEBIT's cyclotron resonance detection scheme discussed later.
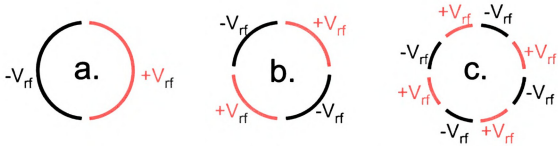
Figure 2.9: Schematic of the Penning trap's segmented ring structure and the application of the RF voltage V_{rf} for a a.) dipole, b.) quadrupole, and c.) octupole excitation.

An ion's motion in the Penning trap can be excited by applying an RF voltage to the trap's ring electrodes. The phases of an RF voltage applied to the segmented ring structure for a dipole, quadrupole, and octupole excitation in the trap are illustrated in Figure 2.9. The amplitude of an ion's motion in the trap can be increased by exposing the ion to a dipole RF electric field at its corresponding eigenfrequency. Driving contaminant ions that happen to be present in the trap at their reduced cyclotron frequency ω_+ their radius can be increased until its larger than that of the hole in the endcap electrode, effectively removing them from the system [65]. A quadrupole RF electric field can be used to couple two separate eigenmotions. Such an excitation is important for mass measurements since it allows the ion's motion to be excited at $\omega_c = \omega_+ + \omega_- (= qB/m)$, thus enabling the cyclotron frequency ω_c to be determined directly. Exposing an ion to a quadrupole RF electric field with a frequency $\omega_{RF} = \omega_c$ will cause its motion to oscillate from a pure magnetron motion to a pure reduced cyclotron motion and vice versa [48,49]. With the correct RF amplitude V_{rf} for a given excitation time T_{rf}, an ion that initially only has magnetron motion can be fully converted into having only reduced cyclotron motion. Since $\omega_+ \gg \omega_-$ this induces a large change in the kinetic energy of the ion which can be detected by a change in the time of flight of ions exiting the trap [49,66]. It should be mentioned that a similar behavior can be obtained with an octupole RF excitation where the ion's motion can be driven at $2\omega_c$. An octupole excitation scheme can achieve an improved mass resolving power but the practicality of this excitation is still under investigation [46,67].

In the TOF-ICR detection technique, ions in the trap are exposed to a quadrupole RF electric field and then ejected from the trap. As an ejected ion traverses through the fringing field of the magnet, its radial energy is converted into axial energy. This conversion is due to the interaction of the ion's orbital magnetic moment $(\mu = \frac{E_r}{B_0})$ with the magnetic field gradient $(\frac{\partial B}{\partial z})$ which exerts an axial force on the ion equal to $F = \frac{E_r}{B_0}\frac{\partial B}{\partial z}$ where E_r is the ion's radial energy and B_0 is the initial magnetic
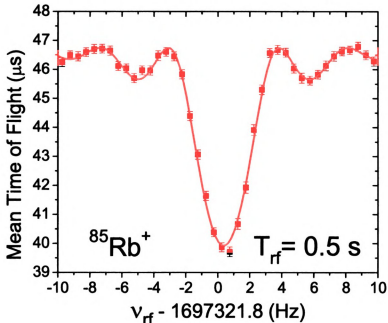
Figure 2.10: Cyclotron resonance curve obtained for ^{85}Rb$^+$. Plotted is the mean time of flight of ions from the Penning trap to the detector as a function of the applied RF frequency (ν_{rf}). The solid curves shows a fit of the theoretical line shape to the data.

field strength. Due to the higher radial velocity associated with the reduced cyclotron motion, the largest axial velocity will be obtained when an ion's initial magnetron motion has been fully converted into cyclotron motion. The relative axial velocity can be easily detected by recording the ion's time of flight from the Penning trap to an ion detector. The cyclotron resonance curve is obtained by applying a quadrupole RF electric field for several frequencies ν_{rf} close to the cyclotron frequency ν_c and plotting the average measured time of flight as a function of applied frequency. The curve will have a minimum at the ion's cyclotron frequency. The cyclotron frequency can then be determined by fitting the theoretical line shape [48] to the data. A typical cyclotron resonance curve obtained for ^{85}Rb$^+$ ions at the LEBIT facility can be seen in Figure 2.10.

The mass resolving power R achieved with TOF-ICR detection technique for an

excitation time T_{rf} is given by the expression:

$$R = \frac{\nu}{\Delta\nu} = \frac{m}{\Delta m} \approx \nu_c \cdot T_{rf}.$$ (2.5)

For a given number N of detected ions, this resolution leads to a statistical precision of

$$\frac{\delta m}{m} = \frac{\delta\nu}{\nu} \approx \frac{1}{R \cdot \sqrt{N}} \approx \frac{\gamma}{\nu_c \cdot T_{rf} \cdot \sqrt{N}}$$ (2.6)

where γ is a factor dependent on the individual experiment. The value of this factor is determined by the achievable change in time of flight of an ion due to the RF excitation applied in the trap along with the width of the ion's time-of-flight distribution at the ion detector. In the case of LEBIT it was determined to be about $\gamma \approx 0.3$ [47]. To determine the magnetic field's strength the cyclotron frequency of a stable isotope with a well-known mass can be measured. By performing such a reference measurement before and after the measurement of an ion with an unknown mass the magnetic field strength during the measurement can be interpolated, and thus the mass of the unknown ion can be extracted.

Chapter 3

Mass Measurement of N $\approx$ Z $\approx$ 34 Nuclides

Mass measurements of nuclei in the N $\approx$ Z $\approx$ 34 region are important for rp process network calculations and investigating the structure of nuclei close to the proton dripline. In this work, high-precision Penning-trap mass measurements of ^{68}Se, ^{70}Se, ^{70m}Br, and ^{71}Br were performed at the LEBIT facility [4]. These measurements complement earlier studies made by LEBIT in this mass region [5].

3.1 Experimental Procedure

For this experiment, a primary beam of ^{78}Kr with an energy of 150 MeV/u was impinged on a beryllium target to create a secondary beam of rare isotopes via projectile fragmentation. The isotopes of interest (^{68}Se, ^{70}Se, ^{70m}Br, and ^{71}Br) were separated out of this secondary beam with the A1900 and delivered to the gas stopping station. For the measurements reported here, the gas cell was operated at a helium gas pressure of 500 torr, and the angle of the glass degrader was optimized for each isotope.

The RFQ mass filter was used in combination with a silicon detector to mea-
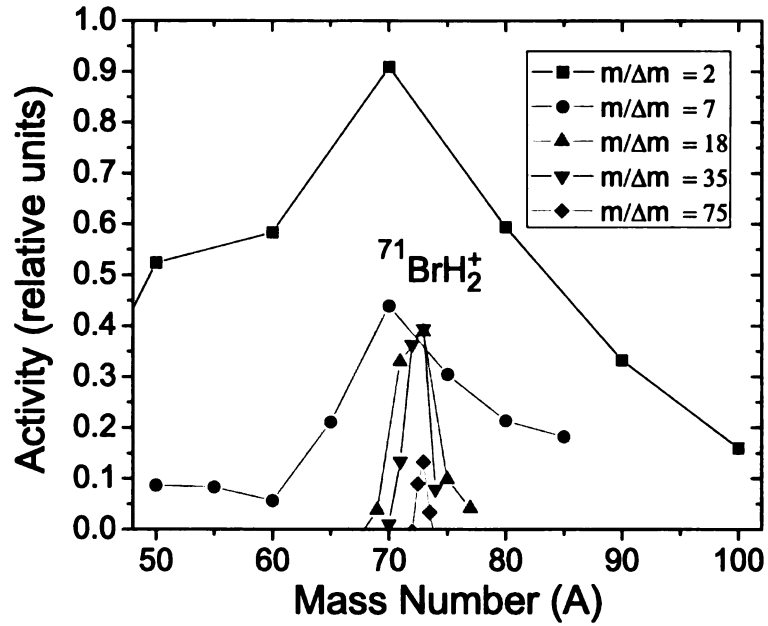
Figure 3.1: The observed activity versus mass number using different mass filter resolving powers (m/Δm), shows that ^{71}BrH$_2^+$ ions were extracted from the gas cell.

sure the mass distribution of activity leaving the gas cell. As in earlier experiments performed with LEBIT [5] ions were extracted in different forms depending on the element. A mass scan with the RFQ mass filter and the activity detected on the silicon detector can be seen in Figure 3.1 for ^{71}Br ions stopped in the gas cell. The figure shows several measurements performed with differing mass resolving powers ($m/\Delta m$) to determine the charge state and chemical form of the ^{71}Br ions leaving the gas cell. The ^{71}Br isotopes were extracted in the form of molecular ^{71}BrH$_2^+$ ions while the ^{70m}Br isotopes were extracted as atomic ^{70m}Br$^+$ ions; a possible explanation for this variation is the different incident beam rates which were 1300 ion/s in the case of ^{71}Br and 140 ion/s in the case of ^{70m}Br. For the selenium ions both isotopes were extracted as singly charged atomic ions, thus confirming the observations in [5].

For the mass measurements, the RFQ mass filter was operated with a resolving power of approximately R = $\frac{m}{\Delta m}$ = 50. This filtering, as previously mentioned,

removed non-isobaric contaminants created during the stopping process by charge exchange reactions between the helium ions and gas impurities in the gas cell. The purified beam from the gas stopping station was then transported to the beam cooler and buncher. The cooler section was operated with a neon gas pressure of 10^{-2} mbar to break up undesired contaminant molecular ions through collision induced dissociation (CID). The ions were then accumulated and cooled in the buncher section for times ranging from 100 ms for ^{70m}Br$^+$ to 500 ms for ^{68}Se$^+$. To maximize our usage of the ion beam exiting the gas cell, ions were simultaneously loaded into the beam cooler and buncher while a measurement was being performed in the Penning trap. After ejection from the beam cooler and buncher, the pulsed beam was further purified using the system's time-of-flight mass filter to remove any remaining non-isobaric contaminant ions. Ion pulses entering the LEBIT Penning trap were prepared with a pure magnetron motion, necessary for the measurement cycle, using the Lorentz steerer [46,61].

Once captured in the Penning trap, the ions were further purified using a reduced cyclotron dipole excitation to drive identified and suspected isobaric contaminant ions from the trap. The ions of interest were then excited using a quadrupolar RF electric field. Excitation times in the trap depended on the half-lives and ranged from $T_{rf} = 100$ ms in the case of ^{70m}Br$^+$ to $T_{rf} = 1.25$ s in the case of ^{68}Se$^+$. After being excited in the trap the ions were ejected, and their time of flight to the BOB6 MCP detector was determined. This procedure was repeated for different excitation frequencies to obtain the cyclotron resonance curves for ^{68}Se$^+$, ^{70}Se$^+$, ^{70m}Br$^+$, and ^{71}BrH$_2^+$; examples are shown in Figure 3.2. The lowest obtained resolving power was $R \approx 3 \cdot 10^5$ for ^{70m}Br$^+$, and the highest was $R \approx 3 \cdot 10^6$ for ^{68}Se$^+$.

During the measurements of ^{68}Se$^+$, ^{70m}Br$^+$, and ^{71}BrH$_2^+$ the average number of ions stored in the trap was kept below one per cycle, assuming a 30% detection efficiency of ejected ions on the BOB6 MCP detector. This minimized systematic effects due to the interaction of simultaneously stored ions with different masses

27

Mean Time of Flight (μs)

Mean Time of Flight (μs)
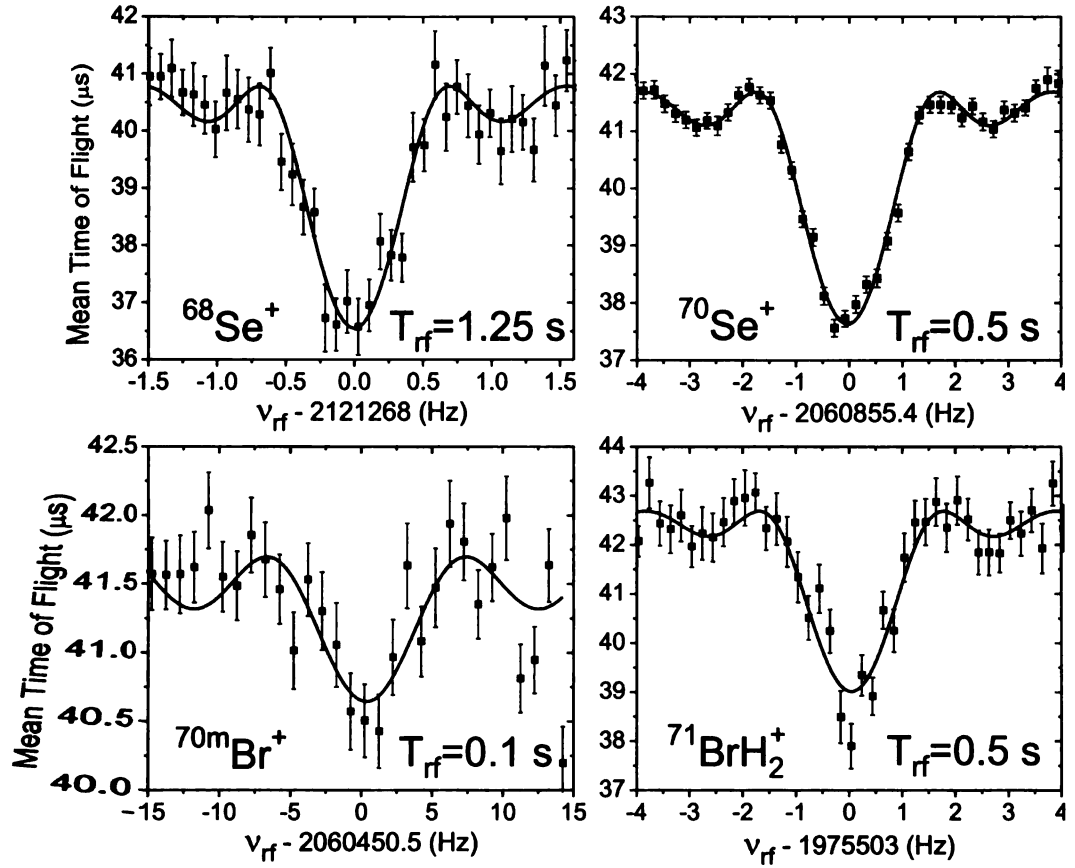
Figure 3.2: Cyclotron resonance curves observed for $^{68}Se^+$, $^{70}Se^+$, $^{70m}Br^+$, and $^{71}BrH_2^+$. Different excitation times (T_{rf}) as indicated in the figures were used.

[65]. Each cyclotron frequency measurement of a rare isotope was bracketed with measurements of a stable reference ion with a well-known mass that was also extracted from the gas cell. In all cases, a reference ion within a ± 1 atomic number of the rare isotope was used to minimize mass-dependent systematic effects due to imperfections in the trapping field [49]. At least four individual measurements were performed per isotope.

3.2 Data Evaluation

For each cyclotron resonance curve, the theoretical line shape [48] was fit to the data to extract the cyclotron frequency and its associated statistical error. In order to determine the magnetic field during the measurement of the rare isotope, a linear interpolation was applied between the cyclotron frequencies obtained from bracketing measurements of the reference ion. From this interpolation the reference ion's cyclotron frequency $(\omega_{c,Ref})$ at the time of the rare isotope's measurement was obtained. A ratio of the rare isotope's and reference ion's cyclotron frequency $(R = \omega_c/\omega_{c,Ref})$ was then calculated for each measurement. From the individual frequency ratios a weighted average ratio $(\bar{R})$ was calculated and used to determine the mass of the ion. The final uncertainty for the average ratio value was calculated from the individual measurement's uncertainties using a standard propagation of error for a weighted average described more thoroughly in [46]. Only in the case of ^{70}Se was an additional systematic shift applied, the calculation of this shift and other systematic errors that were considered will be discussed in the next section. Table 3.1 summarizes the nuclides studied in this work, their reference ions, and the average of the cyclotron frequency ratios.

Plots of the individual frequency ratio obtained for each the measurement of ^{68}Se$^+$, ^{70}Se$^+$, ^{70m}Br$^+$, and ^{71}BrH$_2^+$ are shown in Figure 3.3 along with the uncertainty obtained for the average ratio. In all cases, the individual values obtained

Table 3.1: Ions investigated together with the half-life $(T_{1/2})$, the reference ion used (Ref.), the number of individual cyclotron frequency measurements (N), and the averaged frequency ratio $(\bar{R})$.

	$T_{1/2}$	Ref.	N	$\bar{R}$
^{68}Se$^+$	35.5 s	CF$_3^+$	12	1.015504334(8)
^{68}Se$^+$	35.5 s	C$_6$H$_5^+$	5	1.133899455(9)
^{70}Se$^+$	41.1 m	^{13}CF$_3^+$	4	1.000930159(24)
^{70m}Br$^+$	2.2 s	^{13}CF$_3^+$	7	1.00073357(23)
^{71}BrH$_2^+$	21.4 s	C$_4$H$_9$^{16}O$^+$	4	1.001512556(80)

were in good agreement with the final ratio value expect for the second measurement of $^{70m}Br^+$. No valid reason could be found to exclude this measurement; thus it was used in the final evaluation. Its contribution to the final ratio value was a shift of $\delta R = 1.6(20) \cdot 10^{-7}$ that effectively doubled the uncertainty for the average frequency ratio of $^{70m}Br^+$.
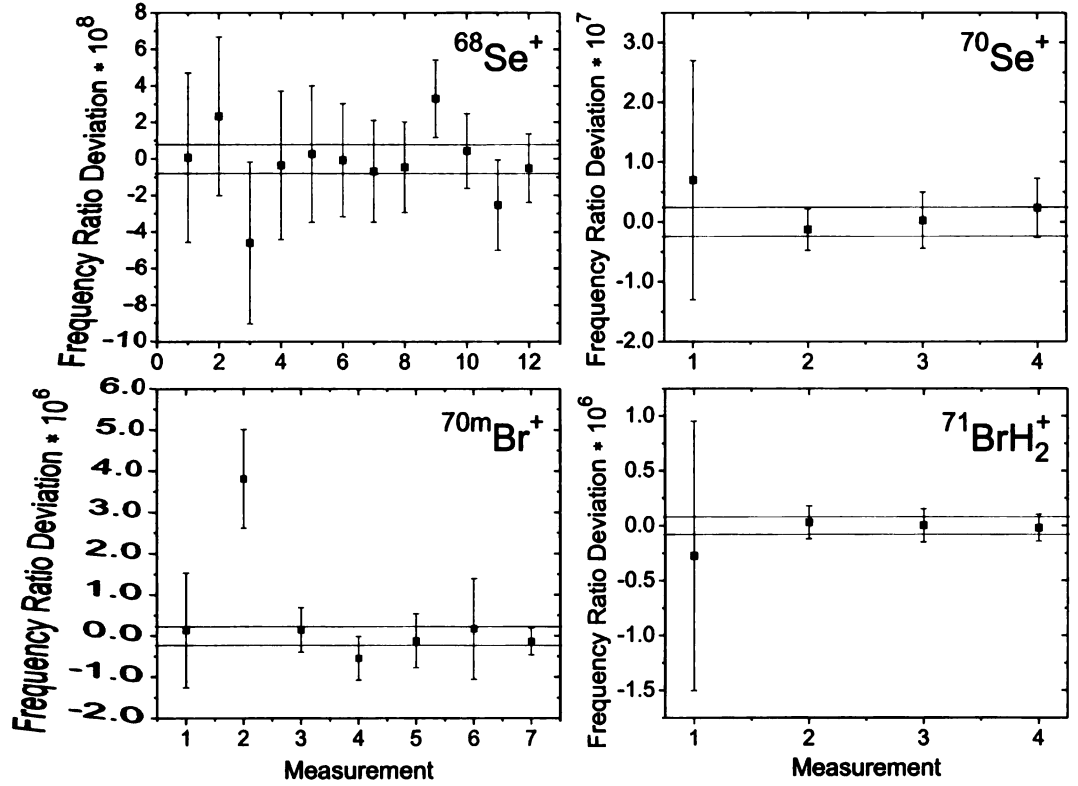
Figure 3.3: Frequency ratio deviation from the mean value $(R - \bar{R})$ given in Table 3.1 obtained for each measurement of $^{68}Se^+$, $^{70}Se^+$, $^{70m}Br^+$, and $^{71}BrH_2^+$. The band indicated by solid lines corresponds to the final uncertainty obtained.

3.2.1 Uncertainty Analysis

The most significant non-statistical source of error was a count rate effect that was only present during the measurement of $^{70}Se^+$. In this case an average of about six ions consisting of $^{70}Se^+$ and contaminant ions were stored in the trap simultaneously.

The possible effects of a frequency shift due to ion-ion interaction of unequal ion species in the trap was evaluated by determining the measured cyclotron frequency as a function of the number of stored ions and extrapolating to the frequency that would have been obtained with one ion. The result of this count rate analysis was a final frequency ratio of $\bar{R} = 1.000930159(24)$. This new value shows a significant shift of $1.6(21) \cdot 10^{-8}$ from the value obtained without this analysis.

Additional systematic effects including relativistic frequency shifts, mass-dependent systematic errors, the effects of a nonlinear change in the magnetic field, and the influence of contaminant ions present in the trap were considered but not taken into account since they were well below the statistical uncertainties. Next each of these systematic errors is discussed. The "relativistic mass" of an ion is $m = \gamma m_0$ where $\gamma = \sqrt{1/(1 - v^2/c^2)}$ was used to normalize the mass of the ion in the rest frame (m_0) to its velocity (v) and the speed of light (c). The measured cyclotron frequency is also affected by this mass shift and can be expressed as $\omega_c = qB/\gamma m$. A relativistic shift in the frequency ratio can be suppressed by using a reference ion and measurement ion with a similar mass. For our measurements, mass doublets were used in all cases except for the measurement of ^{68}Se$^+$. Even though ^{68}Se$^+$ was our highest precision measurement ($\frac{\delta R}{R} = 8 \cdot 10^{-9}$) the calculated relativistic shift in the frequency ratio ($2.9(3) \cdot 10^{-10}$) was found to be insignificant. This shift was calculated using an initial magnetron radius of $\rho_- = 0.75(1)$ mm and $\rho_- = 0.94(1)$ mm for the ^{68}Se$^+$ ions and CF$_3^+$ ions, respectively, that were obtained from fits of the resonance curve.

Residual trapping field imperfections can also cause shifts in the measured cyclotron frequency [68]. The size of these shifts depend on the ion's motion in the trap and its mass. If a mass doublet is used to determine the ratio of the isotope of interest and reference ions' cyclotron frequency, these effects will cancel. In order to determine the contribution of these mass-dependent systematic errors, prior to our experiment mass measurements were performed using several well-known ions with largely different masses. Comparing the mass values from this analysis to known values from
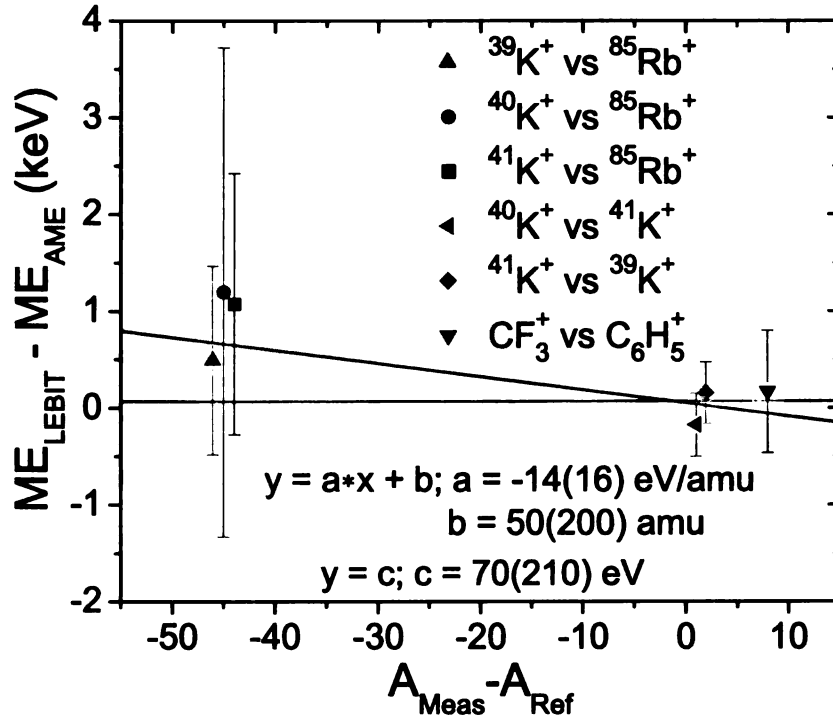
Figure 3.4: The mass difference (in keV) between values from the AME'03 [2] and a **LEBIT** measurement plotted against the difference between the measurement and reference ion's mass number.

the AME'03 [2], as shown in Figure 3.4, no statistically significant mass-dependent error was found. This was determined using an F-test for a 1st order polynomial fit ($y = a \cdot x + b$) with the criterion that the results have less then a 5% chance of being generated by a dataset with no mass dependence. Fitting the data with a constant ($y = c$) revealed an average deviation of 70(210) eV between the two data sets which is well below the uncertainty of any measurement performed in this work and statistically consistent with zero.

Systematic errors in the frequency ratio can also arise due to a non-linear change in the magnetic field since a linear interpolation was used to determine the reference ion's cyclotron frequency during the measurement of a rare isotope. Plots of the magnetic field's change and calibration for the measurements of $^{68}Se^+$, $^{70}Se^+$, $^{70m}Br^+$, and $^{71}BrH_2^+$ can be seen in Figures 3.5. A linear change in magnetic field over time was

observed for the measurement $^{70}\text{Se}^+$, $^{70m}\text{Br}^+$, and $^{71}\text{BrH}_2^+$ depending on the rate of the compensation current applied to counter the natural decay of the magnetic field. In the case of $^{68}\text{Se}^+$, approximately 5 hours into the measurement, the magnetic field's decay constant can be seen to change from $1.7 \cdot 10^{-7}$ T/h to $-3.1 \cdot 10^{-8}$ T/h (Figure 3.5). This change in the decay constant could be due to an unknown external perturbation. To determined the effects of this change the first 8 measurements and last 6 measurements were evaluated separately. The ratios obtained from this analysis were $\bar{R} = 1.0155043301(140)$ and $\bar{R} = 1.0155043361(97)$ respectively. Since these ratios are in good agreement no data were excluded in the final analysis.

The effects of a non-linear change in the magnetic field of LEBIT was studied in
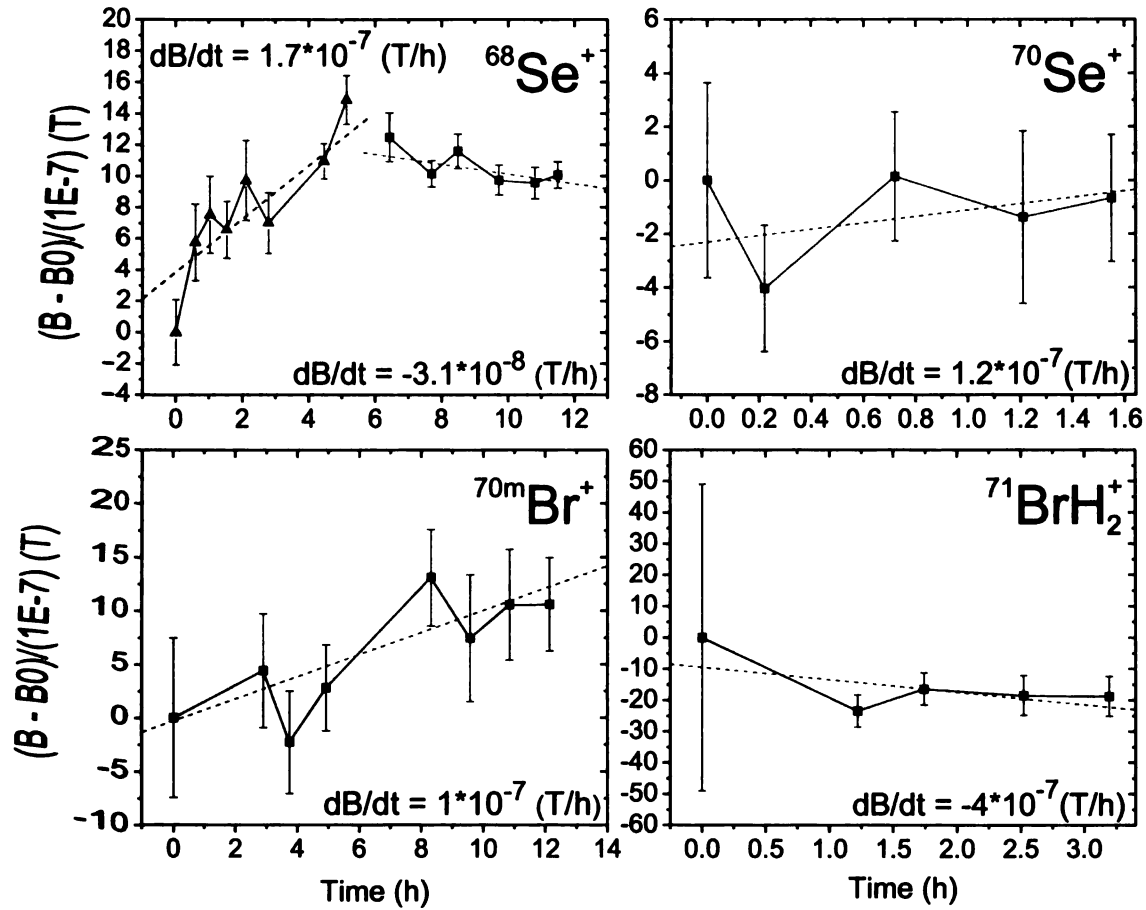
Figure 3.5: Observed change (dashed line) and calibration (solid line) of the magnetic field strength for the measurement of $^{68}\text{Se}^+$, $^{70}\text{Se}^+$, $^{70m}\text{Br}^+$, and $^{71}\text{BrH}_2^+$.

more detail in [46] and it was found that for times between reference measurements less then 1.5 hours the uncertainty in the measured frequency introduced by changes in the magnetic field was on the order of $\delta v/v = 2(1) \cdot 10^{-10}$. As this value is much less then the statistical uncertainty obtained for any individual measurement performed during the present experiment, it was not included in the final uncertainty analysis. Only in the case of $^{70m}\text{Br}^+$ and $^{71}\text{BrH}_2^+$ (Figure 3.5) were the measurement times larger then 1.5 hours. During these measurements, the statistical uncertainties ($\delta v/v > 5 \cdot 10^{-7}$) were an order of magnitude larger than effects due to non-consideration of any non-linear magnetic field change.

3.2.2   Evaluation of ^{70m}Br

The evaluation of the ^{70}Br mass was complicated by the existence of two states with comparable masses. ^{70}Br has a $J^\pi = 0^+$ ground state with a half-life of $T_{1/2} = 79.1(8)$ ms and a longer-lived, $T_{1/2} = 2.2(2)$ s, $J^\pi = 9^+$ β decaying isomeric state [69, 70] with an excitation energy of 2292.2(8) keV [3]. The measurement of ^{70}Br (Figure 3.2) contained only one resonance. Therefore, further evaluation was required to determine whether this resonance corresponded to that of the ground or β decaying isomeric state. The fact that the half-lives of the two states differ by over an order of magnitude was used to support an assignment.

To determine the measured state of ^{70}Br the number of ions per trapping cycle measured after Penning trap was compared to the number of ions expected based on the number of ions leaving the gas cell. The measurements necessary for this comparison were performed on the BOB6 MCP detector (see Figure 2.2) and the silicon detector located after the mass filter in BOB1. The theoretically expected number of ions (N_{exp}) was calculated using the expression:

$$(N_{exp}/\varepsilon) \cdot \ln(2)/T_{1/2} = R_{gs} \cdot (1 - e^{-t_1 \cdot \ln(2)/T_{1/2}})(e^{-t_2 \cdot \ln(2)/T_{1/2}}) \qquad (3.1)$$

which is a growth and decay curve based on the ions accumulation and decay in the beam cooler and buncher and subsequent decay in Penning trap. From the rate leaving the gas cell (R_{gs}), Equation 3.1 gives the number of ions that should be detected per trapping cycle based on the relative efficiency ε of the two detectors, a time t_1 during which the ions were allowed to accumulate and cool in the beam cooler and buncher, a time t_2 required for contaminant ion removal and excitation in the Penning trap, and the half-life $T_{1/2}$ of the ion.

To determine the relative efficiency of the 2 detectors this rate analysis was first performed for the case of ^{71}Br where the half-life of the measured state ($T_{1/2}$ = 21.4 s) was known and long enough to avoid decay losses. For ^{71}Br, a decay rate of 1.4(5) ions/s was measured with the silicon detector and on average 0.21(6) ions/cycle were observed on the BOB6 MCP detector for an accumulation time t_1 = 250 ms. From this comparison the relative efficiency of the 2 detectors was determined to be approximately ε = 0.6. Using this value to evaluate the case of ^{70}Br, the number of ions expected at BOB6 were 0.019(3) ions/cycle and 0.0015(2) ions/cycle for ^{70m}Br ($T_{1/2}$ = 2.2 s) and ^{70}Br ($T_{1/2}$ = 79.1 ms), respectively. These calculations were performed using the beam rate of 0.07(1) ions/s measured on the silicon detector, an accumulation time t_1 = 500 ms, and a decay time in the trap t_2 = 135 ms. Based on the 0.03(1) ions/cycle we actually observed on the BOB6 MCP detector it was concluded that the measured resonance for ^{70}Br corresponded to that of the isomeric state.

3.3 Results

3.3.1 Atomic Masses Values

As was indicated above, the frequency ratios $R = \omega_c/\omega_{c,Ref}$ measured in this work (Table 3.1) were used to determine the mass values of the rare isotopes being inves-

tigated. The mass values (m) were obtained via the relation:

$$m = \frac{1}{R} \cdot (m_{ref} - m_e) + m_e \qquad (3.2)$$

where m_e is the mass of the electron, and m_{ref} is the mass of the reference isotope calculated from the 2003 Atomic Mass Evaluation (AME'03) [2]. The binding energy of the missing electrons were neglected from Equation 3.2 as they are much smaller then the frequency ratios' uncertainties.

Table 3.2: Mass excess values ME in keV obtained with LEBIT, from AME03 [2] and the difference $\Delta ME = ME_{AME'03} - ME_{LEBIT}$. Also given is the ground state mass of ^{70}Br obtained from the LEBIT mass for ^{70m}Br and the excitation energy from [3].

Species	ME_{LEBIT} (keV)	$ME_{AME'03}$ (keV)	ΔME (keV)
^{68}Se	-54189.3(5)	-54210(30)	-21(30)
^{70}Se	-61929.7(1.6)	-62050(60)	-120(60)
^{70m}Br	-49133(15)	-49138(310)	-5(310)
^{71}Br	-56502.4(5.4)	-57060(570)	-558(570)
^{70}Br	-51425(15)	-51430(310)	-5(310)

Table 3.2 contains the final mass values obtained in this work along with the mass values from the AME'03 [2] and their differences to LEBIT's measurements. The presented mass uncertainties range from $\frac{\delta m}{m} = 8 \cdot 10^{-9}$ for ^{68}Se to about $\frac{\delta m}{m} = 2.5 \cdot 10^{-7}$ for ^{70m}Br. The ground state mass value given in Table 3.2 for ^{70}Br was calculated using the measured mass value for the isomeric state ^{70m}Br and the known excitation energy of 2292.2(8) keV [3].

A visual comparison of the new mass values to values from previous measurements and the AME'03 [2] can be seen in Figure 3.6. In all cases, the values obtained in this work show an increased precision by a factor of 40 or more over values from the AME'03 [2]. The new mass values also are in good agreement with those listed in AME'03 [2] except for the case of ^{70}Se. Results from time-of-flight measurements of ^{70}Se preformed with a mass spectrometer [8, 12] agree with the more precise LEBIT
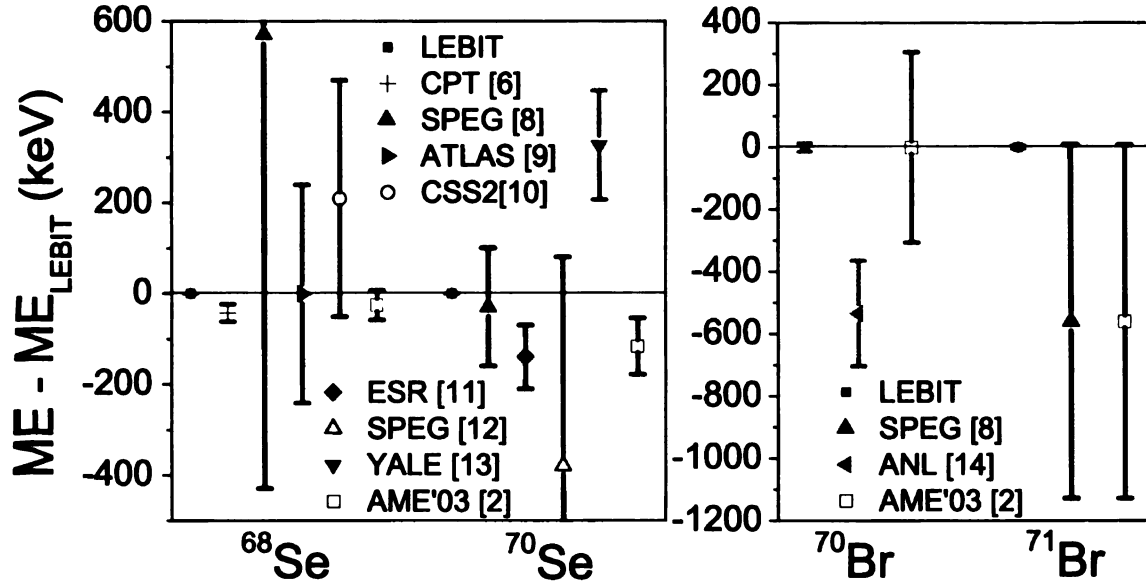
Figure 3.6: A comparison between the LEBIT mass values and from previous experiments [6,8–14] and AME'03 [2].

value. Deviations of more than 2σ are observed for results from a β^+ decay [13] and a storage ring time-of-flight measurement [11]. Among the isotopes studied only ^{68}Se was measured previously in a Penning trap. The Canadian Penning trap (CPT) mass value [6] disagrees by approximately 2σ with the more precise LEBIT result. Mass values of ^{68}Se have also been obtained via β^+ decay Q value measurements [9], and time–of–flight measurements using a mass spectrometer [8] and a cyclotron [10,31]. While data from [8], [9], and [10] agree with our value, the value from [31] shows a 23σ deviation and thus was not included in Figure 3.6. The mass of ^{71}Br was measured earlier by its time of flight through a mass spectrometer [8], and this values agrees with our result. For ^{70}Br, a preliminary mass value was given in [14] but excluded since 1993 from the AME [71] due to a conflict with the mass systematic trends in this region. Our measurement agrees with the extrapolation from the AME'03 [2] and disagrees with [14] by 0.5 MeV and thus supports this rejection.

37

3.3.2 Mass Predictions from Coulomb Displacement Energies

Nuclei in the N $\approx$ Z $\approx$ 34 region are difficult to obtain in laboratory nuclear reactions due to their proximity to the proton dripline and thus low production rates. However, the masses of these nuclei are vital to our understanding of the rp process and the structure of nuclei far from stability. In the absence of experimental data, the masses of nuclei on the proton-rich side of the N = Z line have been obtained from Coulomb displacement energies (CDE) calculated with the Skyrme Hartree-Fock model [1] and the known mass of the neutron-rich mirror nuclei. The Coulomb displacement energy is the binding energy difference between mirror nuclei and is thought to be calculated more accurately than the total binding energy as it is mostly dependent on the Coulomb interaction. In light nuclei where precise experimental mass data is available on both sides of the N = Z line these calculations have been shown to be accurate within 100 keV [1].

In the N $\approx$ Z $\approx$ 34 region few masses beyond the N = Z line have been measured. However, with our mass measurements of ^{70}Se and ^{71}Br and using the CDE values from [1], 22190(100) keV and 11260(100) keV respectively, higher accuracy mass predictions were made for the proton-rich nuclei ^{70}Kr and ^{71}Kr. Table 3.3 gives the new predictions together with the values from the AME'03 [2]. As shown in Table 3.3, the values obtained in this work are in reasonable agreement with those from the AME'03 but are a factor of 4 more precise.

Table 3.3: A comparison of predicted mass excesses in keV using Coulomb displacement energies [1] and data from this work to values from the AME'03 [2].

Species	$ME_{LEBIT+CDE}$	$ME_{AME'03}$	ΔME
^{70}Kr	-41304(100)	-41680(390)	-376(403)
^{71}Kr	-46025(100)	-46920(650)	-895(658)

3.3.3

3.3.3 Neutron-Proton Pairing Energies

The pairing energy V_{np} of the last valence neutron and proton is thought to play a pivotal role in the structure of nuclei. V_{np} is defined as the average interaction energy of the last neutron and proton in a nucleus and is given by the expression:

$$V_{np} = [B_{N,Z} - B_{N-1,Z}] - [B_{N,Z-1} - B_{N-1,Z-1}] \qquad (3.3)$$

where B is the nuclear binding energy. The pairing energy of N = Z nuclei are especially interesting, due to an observed enhancement called the Wigner energy [72]. In [73], the enhanced pairing energy of N = Z nuclei was explained by the supermultiplet model of nuclei [74] which assumes a spin-isospin symmetry. Figure 3.7 shows the neutron-proton pairing energy for odd-odd N = Z nuclei that were calculated with mass values from the AME'03 [2]. This figure shows that going from very light to heav-
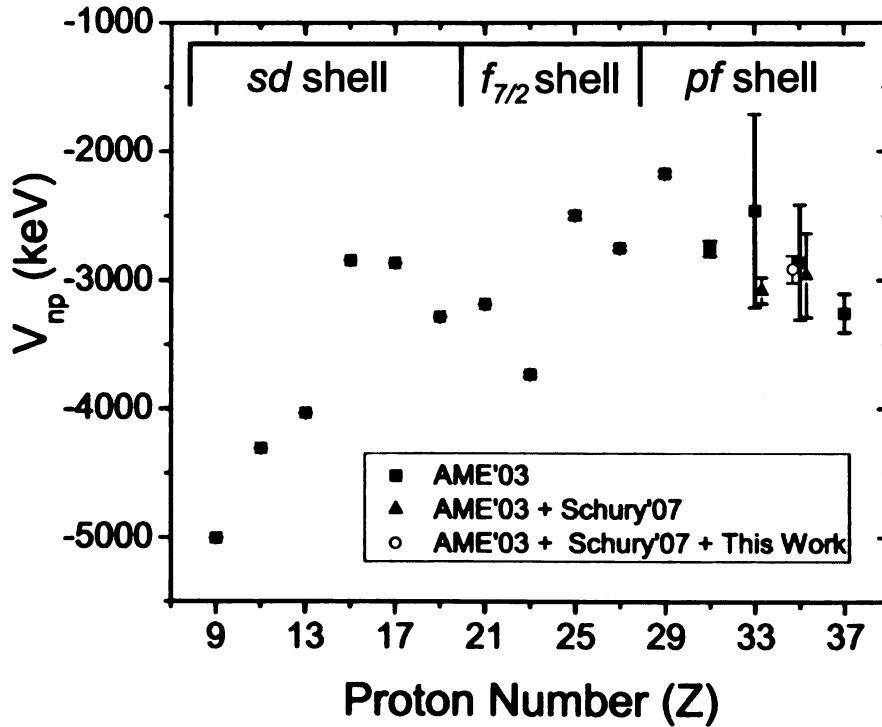
Figure 3.7: The neutron-proton pairing energies are shown for odd-odd N = Z nuclei up to ^{74}Rb as function of the proton number Z.

ier nuclei in the *sd* shell, the pairing energy of N = Z nuclei decreases in magnitude (i.e. becomes less negative). This decrease is due to the effects of spin-orbit coupling and the Coulomb interaction on spin-isospin symmetry. For nuclei heavier then ^{56}Ni an increase in the neutron-proton pairing energy and a restoration of the spin-isospin symmetry was predicted due to a reduced spin-orbit splitting in the *pf* shell [73]. A possible increase in strength of the neutron-proton pairing energy for heavier nuclei (Z > 28) is therefore of great interest and will require more mass measurements along the N = Z line for heavier isotopes.

Taking the improved mass values from this experiment, a previous LEBIT measurement [5], and Equation 3.3 the neutron-proton pairing energy for ^{70}Br was calculated to be $V_{np} = -2920(110)$ keV. Our value is in good agreement with the pairing energy calculated using masses and extrapolated masses from the AME'03 [2] ($V_{np} = -2860(330)$ keV) but has a factor of 3 smaller uncertainty. A comparison of the neutron-proton pairing energy calculated in this work and from the AME'03 can be seen in Figure 3.7. While there is an indication that neutron-proton pairing energy increases (i.e. becomes more negative) with mass for the heavier N = Z nuclei in the *pf* shell more data are required to validate this trend.

Chapter 4

rp Process Network Calculations and Results

The current understanding of type I x-ray bursts and the properties of the involved neutron stars can be improved through comparisons of calculated x-ray burst light curves with observations. The usefulness of these comparisons depends heavily on the quality of the burst model's input data. The required data ranges from proton capture reaction rates to β decay half-lives. The rp process is the driving capture process for nuclei heavier ^{56}Ni in these burst models. To model accurately the delay in the rp process caused by the waiting point nuclei ^{64}Ge, ^{68}Se, and ^{72}Kr, the nuclear masses of these and the surrounding nuclei are required. We report here an examination of the sensitivity of an rp process network calculation [1, 30] to the mass uncertainty of nuclei in the $N \approx Z \approx 34$ region.

4.1   Introduction

The dependence of rp process network calculations on nuclear masses can be made apparent by considering the time dependence of an isotope's abundance Y_A during a burst. For each isotope, there are a series of decays and nuclear reactions which will

either increase or decrease its abundance. For example, the time derivative of this isotope's abundance due to a proton capture reaction $(A + p \rightarrow B + \gamma)$ from nucleus A to nucleus B and the complementary photodisintegration reaction $(B + \gamma \rightarrow A + p)$ is given by

$$\frac{dY_A}{dt} = -Y_A Y_p \rho N_A \langle \sigma \nu \rangle_{A(p,\gamma)B} + Y_B Y_\gamma \rho N_A \langle \sigma \nu \rangle_{B(\gamma,p)A} \qquad (4.1)$$

where ρ is the mass density, Y is the given particle's abundance, and $N_A \langle \sigma \nu \rangle$ is the stellar reaction rate. Whereas, the change in the isotope's abundance due to a β^+ decay from $(A \rightarrow B + e^+ + \nu_e)$ or to this nucleus $(C \rightarrow A + e^+ + \nu_e)$ is given by

$$\frac{dY_A}{dt} = -Y_A \frac{ln(2)}{T_{1/2_A}} + Y_C \frac{ln(2)}{T_{1/2_C}} \qquad (4.2)$$

where $T_{1/2}$ is the given isotope's half-life. In an rp process network calculation the time evolution of the isotopes is described by a large network of such differential equations. The necessary reaction rates are provided by a combination of measurements and, where experimental data are unavailable, statistical model calculations based on the Hauser-Feshbach formalism [75].

Nuclear mass values are required for the calculation of forward and reverse reaction rates. The forward rates such as proton capture (p,γ) reaction rates are mostly obtained through Hauser-Feshbach calculations, and the reverse reaction rates for photodisintegration (γ,p) are calculated from the forward rates through the principle of detailed balance. In this work, we approximated the effects of the mass uncertainties of nuclei in the $N \approx Z \approx 34$ region on a type I x-ray burst network calculations through their impact on the reverse reaction rates. The reason for this choice was that the rp process is to a large extent governed by the flow through a waiting point nuclei, where an equilibrium has developed between the forward proton capture channel and the reverse photodisintegration channel. In such a situation the important parameter is the ratio of the forward and reverse rate, not the direct value of either [1]. The ratio

of the forward and reverse reaction rate is determined by the calculation of the reserve rate from the forward rate. For example, from a proton capture rate $(\langle \sigma \nu \rangle_{A(p,\gamma)B})$ the calculated inverse photodisintegration rate $(\lambda_{B(\gamma,p)A})$ is

$$\lambda_{B(\gamma,p)A} = \frac{(2J_p + 1)G_A}{G_B} \left(\frac{\mu k_b T}{2\pi \hbar^2} \right)^{3/2} exp \left(-\frac{Q_{A(p,\gamma)B}}{k_b T} \right) \langle \sigma \nu \rangle_{A(p,\gamma)B} \qquad (4.3)$$

where J is the spin, μ is the reduced mass, k_b is the Boltzmann constant, T is the temperature, $Q_{A(p,\gamma)B}$ is the Q value of the proton capture, and G is the partition function defined in [24]. The ratio's exponential dependence on the reaction's Q value is why nuclear masses are such a critical parameter in rp process network calculations.

4.2   rp Process Network Calculations

The uncertainties of various Q values for nuclei near ^{64}Ge and ^{68}Se have been significantly improved or corrected, with the high-precision mass data obtained in this work (described in Chapter 3), earlier LEBIT work [5], and predictions made using Coulomb displacement energies (CDE) [1]. A comparison of Q values from this data set (supplemented by mass values from the AME'03 [2] where required) to Q values calculated purely from the AME'03 [2] mass values and to Q values calculated from the AME'03 [2] mass values with the value for ^{68}Se from the Canadian Penning Trap [6] and mass predictions performed using CDE [1] is shown in Table 4.1. The LEBIT data set provides Q values with an improved precision as high as a factor of a 100 over the previous data sets.

Table 4.1: Proton capture reactions for nuclei with $63 \leq A \leq 72$ along with Q values obtained with mass values from the LEBIT data set [1,2,4,5], the AME'03 [2], and the AME'03 [2] including a measurement of ^{68}Se from [6] and CDE from [1].

Reaction	LEBIT (keV)	AME'03 (keV)	AME'03 + CPT + CDE (keV)
^{63}Ga(p,γ)^{64}Ge	5058(4)	5090(30)	5090(30)
^{64}Ge(p,γ)^{65}As	-260(100)	-80(300)	-360(150)
^{65}As(p,γ)^{66}Se	2350(140)	2030(420)	2430(180)
^{64}Ga(p,γ)^{65}Ge	4935(2)	4870(100)	4870(100)
^{65}Ge(p,γ)^{66}As	2830(30)	2380(690)	2377(690)
^{66}As(p,γ)^{67}Se	1820(100)	2280(710)	2400(700)
^{66}Ge(p,γ)^{67}As	2268(3)	2310(100)	2310(100)
^{67}As(p,γ)^{68}Se	4892(1)	4856(110)	4870(100)
^{68}Se(p,γ)^{69}Br	-640(100)	-450(100)	-810(110)
^{69}Br(p,γ)^{70}Kr	2330(140)	2490(400)	2580(160)
^{68}As(p,γ)^{69}Se	4827(6)	4690(50)	4691(55)
^{69}Se(p,γ)^{70}Br	2280(15)	2410(310)	2410(310)
^{70}Br(p,γ)^{71}Kr	1890(100)	2790(720)	2450(660)
^{70}Se(p,γ)^{71}Br	1861(6)	2310(570)	2306(570)
^{71}Br(p,γ)^{72}Kr	4730(10)	4170(570)	4170(570)

4.2.1 Local Network Calculations to Determine the Effective Lifetime of the ^{68}Se Waiting Point
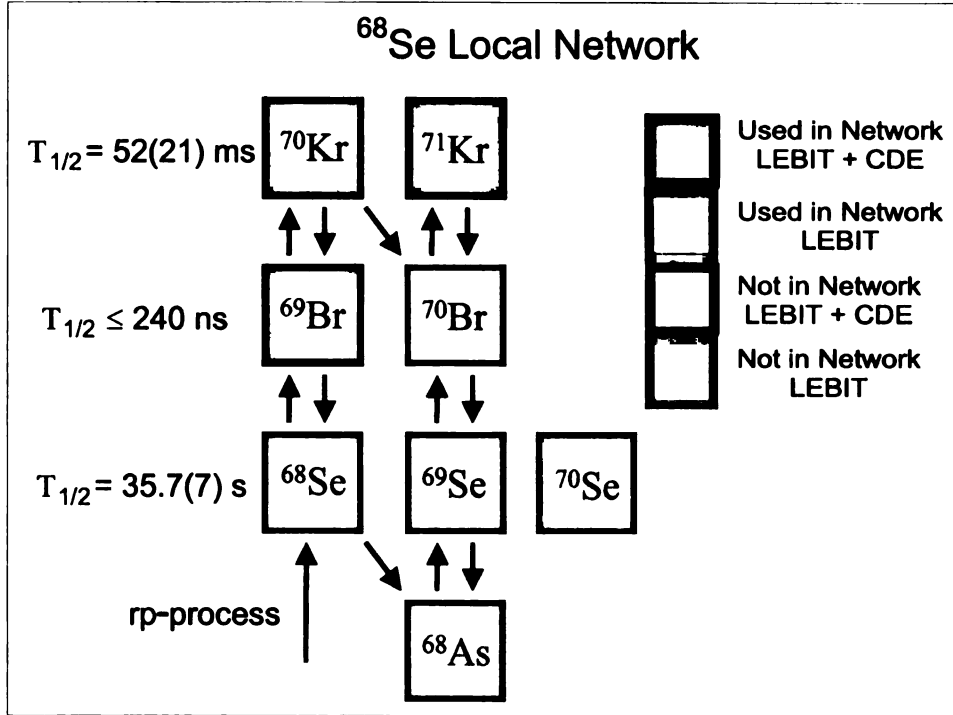
Figure 4.1: The local network used to calculated the effective lifetime of the ^{68}Se waiting point.

The waiting point nuclei ^{68}Se has a β decay half-life of 31.4 s which is relatively long compared to a typical burst duration of 10-100 s. A local network calculation was performed to determine the extent to which the reaction flow through the double proton capture channel could effectively decrease the total lifetime of this waiting point. As illustrated in Figure 4.1, this local network consisted of the nuclei ^{68}As, ^{68,69}Se, ^{69,70}Br, and ^{70}Kr and the reactions relevant to the rp process in this region. The effective lifetime of the waiting point was calculated from the time required to convert 50% of the initial ^{68}Se abundance to a nuclei beyond a single proton capture. For this calculation, a solar abundance of hydrogen was assumed, and the density was held constant at 10^6 g/cm^3 for all simulations. The initial temperature, on the other hand, was varied between 0.5-2.0 GK to cover the range where the double proton
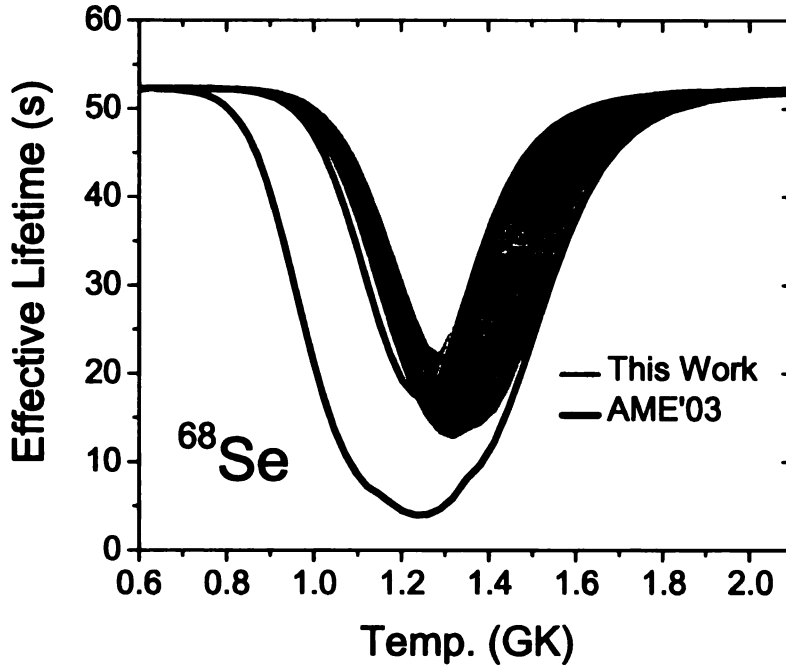
Figure 4.2: The variation of the effective lifetime of the ^{68}Se waiting point versus temperature obtained from a local rp process network calculation using mass values from the data set presented in this work [4] and from a calculation performed using mass values from AME'03 [2] and CPT [6] data set.

capture channel would be significant. The necessary forward (p, γ) reaction rates were taken from [75] and the reverse (γ, p) reaction rates were calculated as discussed in Section 4.1. These reverse reaction rates were recalculated for all variations of the ^{68}Se, ^{69}Br, and ^{70}Kr mass values within their uncertainties. Then a local network calculation was performed for each variation of these new reverse reaction rates to determine the effect of the mass values' uncertainties on the effective lifetime of the ^{68}Se waiting point.

The variation of the effective lifetime of the ^{68}Se waiting point as a function of temperature obtained from this local network calculation can be seen in Figure 4.2. The envelopes shown in this figure represent the range of effective lifetimes obtained for the ^{68}Se waiting point through variations of the AME'03 + CPT data set's and LEBIT data set's mass values. In both cases, for temperatures less then 0.8 GK and

greater then 1.8 GK the effective lifetime of the waiting point was set by the β decay lifetime of the ^{68}Se nucleus. The reason for this is that below 0.8 GK the energy of incoming protons is not large enough to penetrate the Coulomb barrier of the ^{68}Se nucleus and for temperatures greater then 1.8 GK the photodisintegration rates are large enough to significantly reduce the flow through the double proton capture channel. In the intermediate temperature range, a reduction in the ^{68}Se effective lifetime was observed. For the older data set, a minimum effective lifetime of 10.7(68) s was obtained and, within its uncertainty, still allows for the possibility of a lifetime on the order of a few seconds. For such lifetimes, much shorter than typical burst time scales of 10-100 s, ^{68}Se would not be an important waiting point anymore. The new LEBIT data results in a minimum lifetime of 17.4(45) s, and it is now clear that ^{68}Se is a strong waiting point for all prevalent conditions. This change in the calculated lifetime is due to the improved mass predictions obtained for ^{70}Kr and ^{69}Br using our new results for the ^{70}Se mass and the ^{69}Se LEBIT mass measurement [5] together with their CDE [1].

4.2.2 Full Network Calculations

In order to determine the effects of the improved Q values on the light curve, temperature, nuclear energy generation rate, and final elemental abundances of a type I x-ray burst, a full network calculation was performed using a single-zone burst model [1,7]. A realistic burst scenario was created using the parameters given in Table 4.2 from [7] to perform the network calculations. These simulations were performed and compared

Table 4.2: Initial parameter values used for a type I ray burst simulation [7].

Parameter	Value
Accretion Rate	0.1 $\dot{m}_{Edd}$
Energy Emitted Per Accreted Nucleon	0.15 MeV
Hydrogen Mass Faction	0.66
Metallicity (Z)	0.001
Surface Gravity	$1.9 \cdot 10^{14}$ cm/s^2

47
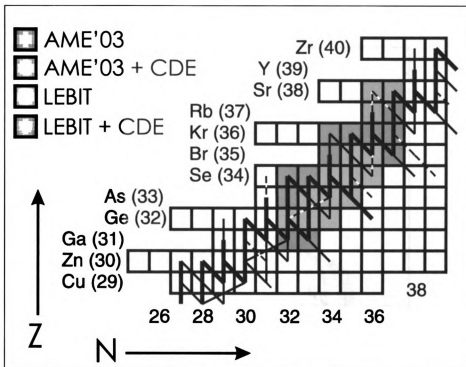
Figure 4.3: *rp* process path in the $N \approx Z \approx 34$ region. The nuclei are colored to indicated how their mass values were determined for the LEBIT data set.

using Q values and uncertainties from each data set presented in Table 4.1 to calculate the reverse reaction rates as described for the local network calculation in the previous section. A simulated *rp* process path, in the $N \approx Z \approx 34$ region, obtained using mass values from the LEBIT data set is shown in Figure 4.3.

The masses of $^{64-66}$Ge, $^{68-70}$Se, and $^{72-74}$Kr were varied within their uncertainty to determine the effects of their mass uncertainties on the simulations results for each data set. This process is illustrated in Figure 4.4 which shows the different temperature curves for the neutron star's crust as a function of time obtained with permutations of the mass values for the LEBIT data set. The same analysis was also performed for the other data sets and x-ray burst output parameters. The results from these analyses for the luminosity, temperature, nuclear energy generation rate and final abundance for the simulated burst are shown in Figures 4.5-4.8, respectively. For simplicity, only an error band that encompasses the results obtained for all permutations is shown in these figures.
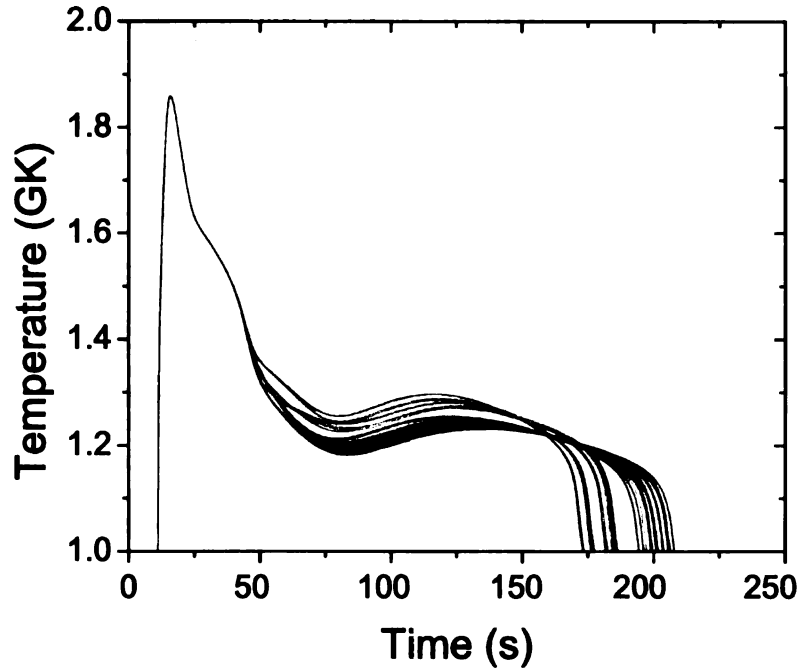
Figure 4.4: Temperature curves of a type I x-ray burst obtained by permutations of the mass values from the LEBIT data set.

For all of these burst output parameters a decrease in the simulated error band's width due to the reduced uncertainties of the mass values provided by the LEBIT data set, compared to the older data sets, was observed. The most significant being the reduced width obtained for the burst's x-ray luminosity as a function of time (Figure 4.5) as it is a direct experimental observable of a type I x-ray burst. The light curves obtained with the LEBIT data shift towards a shorter burst time scale compared to other calculations. This shift can also be seen in the crust's temperature (Figure 4.6) and burst's energy generation rate (Figure 4.7) as a function of time. The reduced uncertainty in the burst's light curve demonstrates that more useful comparisons to observation can now be performed. Such a quantitative comparisons of the simulated and observed bursts would require a more robust stellar burst model (i.e multi-zoned) [76]. Also, to extract the initial system parameters of an observed burst would require comparisons to a range of simulations with differing stellar parameters such as accretion rates, accreted compositions, and neutron star properties. The com-

plexity and time required for this analysis put it beyond the scope of the present work but should be possible. The simulated light curve's accuracy and uncertainty could still be improved through mass measurements of nuclei beyond the $N = Z$ line, e.g. ^{65}As, ^{69}Br and ^{73}Rb, which are especially difficult to measure as they are thought to be proton unbound in some cases (^{69}Br, ^{73}Rb).

Improved abundance data are also important for reliable modeling of neutron star crust processes [29] and to predict possible contributors to galactic nucleosynthesis [22]. The final burst abundances provided by the present model are shown in Figure 4.8, which shows that the uncertainty in the production of heavier nuclei in the rp process has been considerably reduced. The production of these nuclei is strongly dependent on the overall impedance of the rp process reaction flow created by the waiting points in the $A = 64 - 72$ mass region for which improved data are now available. An increase in the amount of $A = 68$ nuclei present after the burst is also observed. This is most likely due to the longer lifetime of the ^{68}Se waiting point found in this work.
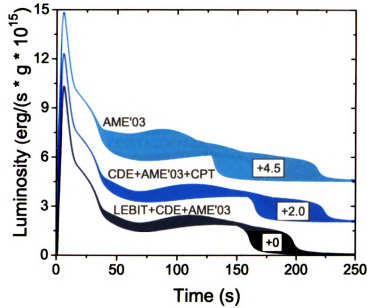
Figure 4.5: Luminosity as a function of time (light curve) of a type I x-ray burst obtained for the Q value data sets presented in Table 4.1. The different curves were offset by the indicated luminosity for clarity.
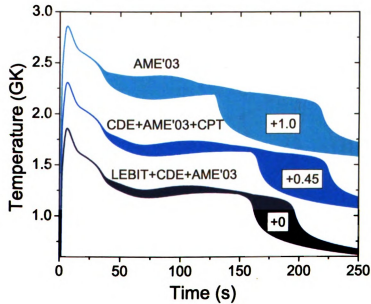
Figure 4.6: Temperature as a function of time of a type I x-ray burst obtained for the Q value data sets presented in Table 4.1. The different curves were offset by the indicated temperature for clarity.
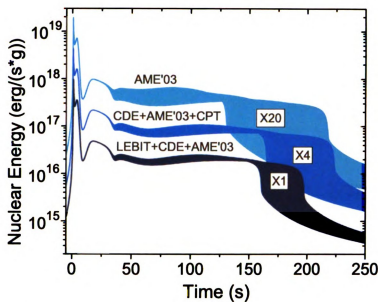
Figure 4.7: The nuclear energy generation rate as a function of time of a type I x-ray burst obtained for the Q value data sets presented in Table 4.1. The different curves were scaled by the given factor for clarity.
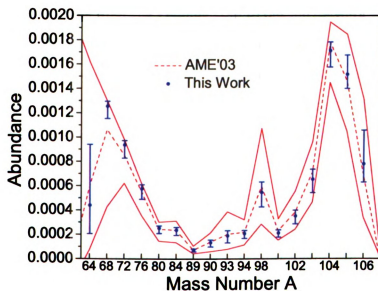
Figure 4.8: Final elemental abundance from a type I x-ray burst obtained using the Q value data set sets presented Table 4.1. The data points correspond to abundances obtained with the LEBIT data set, and the error band to those obtained with the AME'03 [2] + CPT [6] data set.

Chapter 5

A Daly Detector System for Ion Detection

The time-of-flight ion-cyclotron-resonance (TOF-ICR) detection technique employed at the LEBIT facility requires a detection system with the ability to determine the time of flight of individual ions from the Penning trap to an ion detector. The optics used to transport ions from the Penning trap to our ion detector system are detailed in Figure 5.1. Also presented are two different configurations in which a micro-channel plate (MCP) detector can be implemented to detect these ions. In the first detector system employed at LEBIT, ions were directly impinged on an MCP detector. In this type of system, a single ion detection efficiency of about 45% with a time resolution better than 1 ns can be achieved [77]. However, higher detection efficiencies (> 80%) can be obtained by using an MCP detector to detect the secondary electrons generated by impinging the ions onto a cathode. An MCP detector implemented in this configuration is commonly referred to as a Daly detector [62]. Since a high detection efficiency is crucial when working with rare isotopes that have a low production rate, a Daly detector was designed and implemented for the LEBIT facility. Before discussing the new Daly detector, the MCP detectors used at LEBIT will be briefly described.
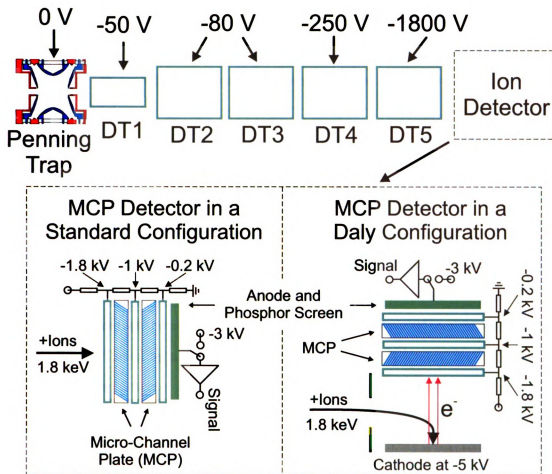
Figure 5.1: Top: Schematic of the Penning trap ejection optics and typical voltages applied to these drift tubes (DT1-6) for ion transport from the trap to the detector. Bottom: Schematic of a MCP detector implemented in a standard configuration for direct ion detection (left) and in a Daly configuration for indirect ion detection via secondary-electron emission (right).

5.1 Ion Detection with an MCP Detector

Single ion detection with an MCP detector is based on the conversion of an ion incident on the detector into a cascade of electrons (about 10^5 electrons per incoming ion) that can be measured using conventional electronics. The MCP detectors used at LEBIT consist of two MCPs in a chevron configuration followed by an anode which is an aluminized phosphor screen. A schematic of one such detector along with the resistor chain used to supply the voltages necessary for operation of the detector is shown in Figure 5.1. An MCP is composed of a material with a high secondary-electron emis-

sion coefficient that is perforated with a 2-D array of small holes (micro-channels) running at slight angle to the plate's normal. Electrons produced by the collision of an incoming ion with the plate's surface are accelerated through these channels and repeatedly collide with the channel's surface. These collisions result in the emission of more electrons and an effective multiplication of the signal's strength. At LEBIT, a potential difference of about -800 V is applied across each plate to ensure the production of a space-charge-limited cascade of electrons from each incident ion. This pulse of electrons is collected at the back of the last plate on the anode. Depending on how the anode is connected the electrons can be observed as an electronic signal or as visible light. The two different connection schemes for the anode are illustrated in Figure 5.1. To detect the electronic signal, the anode is connected to a charge-sensitive preamplifier followed by a digital oscilloscope. In this configuration the ion's time of incidence on the detector relative to their ejection from the Penning trap can be determined. To produce a visible signal, the anode is floated on a high negative voltage ($\approx$ -3 kV) to enable the incoming electrons to penetrate the aluminum layer covering the phosphor screen. The florescence of the phosphor can be used to determine the position of ions incident on the MCP detector.

The detection efficiency of a single charged particle on an MCP detector depends on the configuration of the detector along with properties of the charged particle such as its mass, kinetic energy, and angle of incidence. In the case of LEBIT, the ions to be detected after the Penning trap have masses that range from A=20-100, an incident kinetic energy of 1.8 keV, and an angle of incidence perpendicular to the detector's surface. The detection efficiency of MCP detectors at LEBIT is difficult to determine as the absolute number of ions incident on a detector for any given measurement is unknown. However, an estimate for their detection efficiency can be made using the results from previously published studies [15, 16]. In Figure 5.2, the detection efficiency curves are given for ions [15] and electrons [16] incident on a chevron and single-plate MCP detector, respectively. The dashed line, in this figure, represents the
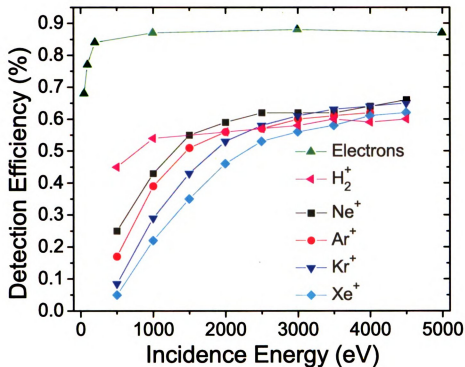
Figure 5.2: Detection efficiency versus impact energy for ions [15] and electrons [16] incident on a chevron and single-plate MCP detector, respectively. The dashed line marks the incident energy of ions at LEBIT.

incident energy of ions at LEBIT and shows that an ion detection efficiency ranging from 40-60% should be obtained. This figure also shows that if electrons were being detected instead of ions the MCP detector's efficiency could increase to about 85%.

5.2 The LEBIT Daly Detector System

In 1960, N. R. Daly implemented an MCP detector in a configuration shown in Figure 5.1 to take advantage of the detector's higher electron detection efficiency [62]. In this configuration ions are directed onto the surface of a cathode made of a material with a high secondary-electron emission coefficient. When an ion collides with the cathode's surface, multiple electrons are freed from the material which are then guided to an

MCP detector by a strong electric field. Due to the increased particle number and the intrinsically higher detection efficiency of electrons on an MCP detector, Daly detectors can achieve detection efficiencies greater than 80% for ions. In order for LEBIT to benefit from such an efficiency increase a Daly detector was designed for the facility. One of the main design criterion was that all ions leaving the Penning trap would impact the cathode such that the resulting electron beam that would be accelerated onto the MCP detector. This is a non-trivial task as the excitation applied to the ions in the trap gives them a range of radial energies resulting in differing trajectories upon ejection. Another important criterion was to maximize the secondary-electron emission by choosing an appropriate material for the cathode.

5.2.1   Design

The LEBIT Daly detector setup was designed and tested through simulations in SIMION [78]. The first step in designing the setup was ensuring that for a given electrode and voltage configuration the emitted secondary electrons would be directed onto the MCP detector. In an iterative process of simulation and modification of the simulated electrode configuration the system was optimized. The finalized electrode geometry, from SIMON, is shown in Figure 5.3 (top view) and Figure 5.4 (front view). An optimal distance between the cathode and the MCP detector of 20 mm was found for the standard operational voltages shown in Figures 5.3 and 5.4. To minimize the electric field penetration of the cathode into the last drift tube (DT6) a 12 mm diaphragm was placed on the end of the tube. To prevent the detector's mount and the surrounding beam tube's electric field from disturbing the ions' trajectories in the Daly detector an overhang was added to the top and bottom of the cathode. The trajectories, in the Daly detector, of $^{84}\text{Kr}^+$ ions ejected from the trap with and without an initial radial energy are shown in Figure 5.3. This figure indicates that in both cases the $^{84}\text{Kr}^+$ ions create an electron beam that would be transported onto the detector.
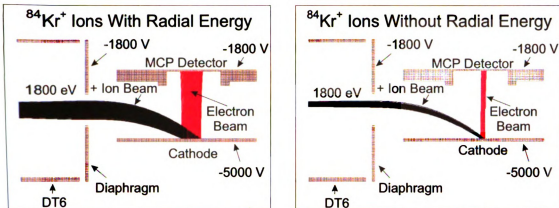
Figure 5.3: Electrode geometry (top view) of the LEBIT Daly detector setup showing trajectories for ions ejected from the trap (black) with and without radial energy. The resultant electron beam is shown in red.

The effect of a fringe magnetic field from the 9.4 Tesla superconducting magnet on the operation of the LEBIT Daly detector was also investigated. Based on a map of the magnetic field provided by the manufacture a fringe field with a strength of 80 Gauss was added in the simulations. A comparison of ion trajectories through the
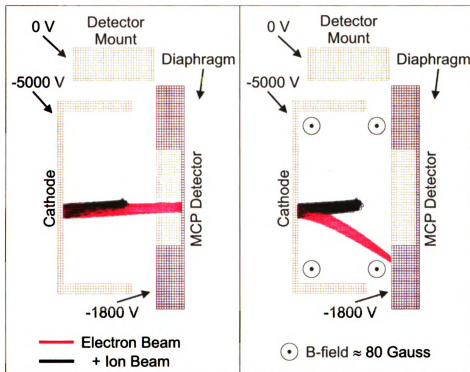
Figure 5.4: Front view of the Daly detector electrode geometry and a comparison of ion trajectories without (left) and with (right) a fringe magnetic field.

Daly detector with and without this fringe field is shown in Figure 5.4. The fringe magnetic field has a large effect on the secondary electrons due to their low mass. Depending on the strength of this field it may prevent the electrons from reaching the MCP detector, and a fringe field compensation could be required.
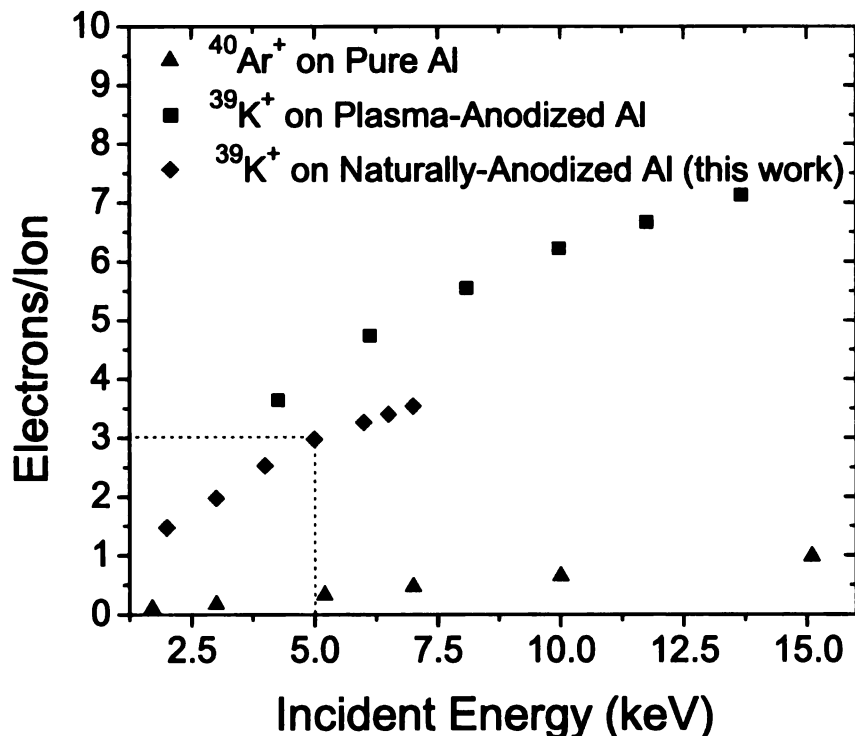
Figure 5.5: Experimental secondary-electron yields from pure [17] and plasma-anodized aluminum [18] as a function of the incident ion beam's energy. Also shown are the results of an electron yield measurement performed with the realized LEBIT Daly detector (see Section 5.2.2 for more details).

To achieve a high detection efficiency the Daly detector's cathode should be made of a material with a high secondary-electron emission coefficient. Figure 5.5 shows the experimental secondary-electron yields for $^{39}K^+$ ions normally incident on a plasma-anodized aluminum target with a 1000 $\mathring{A}$ thick layer of Al_2O_3 [18] and $^{40}Ar^+$ ions normally incident on a pure aluminum target without a layer of Al_2O_3 [17]. These two studies show that in the pertinent energy range the plasma-anodized aluminum has a much higher secondary-electron emission coefficient. At a typical collector voltage

of -5 kV almost 4 electrons would be emitted per incident ion. However, plasma-anodized aluminum is difficult to obtain. An alternative is to use naturally-anodized aluminum which has a Al_2O_3 layer about 10 $\overset{\circ}{A}$ thick and to effectively increase the thickness of this layer by impinging the ion beam at a high angle of incidence with respect to the surface's normal. In [79], it was shown that comparable secondary-electron emission coefficients were obtained for a 30 keV ^{85}Rb$^+$ ion beam normally incident on a plasma-anodized aluminum target and for the same beam incident on a naturally-anodized aluminum target at an angle of 50° from the surface's normal.

For our Daly detector design at typical voltages, ions are impinged on the cathode at an angle of 60° away from normal incidence. Thus if the Daly detector's cathode is made of naturally-anodized aluminum a secondary-electron emission coefficient comparable to the plasma-anodized aluminum data presented in Figure 5.5 should be obtained. Based on this premise an estimate for the probability of detecting at least one electron (P_E) for a single ^{39}K$^+$ ion incident on a Daly detector with our design specifications and a naturally-anodized aluminum cathode can be made. Assuming that the number of electrons emitted per ion incident on the cathode will form a Poisson distribution about the mean value, the probability of detecting at least one electron is described by

$$P_E = 1 - e^{-\gamma_e \varepsilon_t} \tag{5.1}$$

where γ_e is the secondary-electron emission coefficient and ε_t is the MCP detector's efficiency for electrons. With $\gamma_e \approx 4$ [18, 79] and $\varepsilon_t \approx 85\%$ [16] a detection efficiency of about 97% should be obtained. Based on this high detection efficiency and the difficulty of obtaining plasma-anodized aluminum, the cathode was constructed from naturally-anodized aluminium.

5.2.2 Realization and Performance

Based on the specifications for the LEBIT Daly detector obtained through the ion optical design and considerations described in the previous section the mechanical design drawing shown in Figure 5.6 was created. From this drawing the realized Daly detector setup shown in Figure 5.7 was machined and assembled. The Daly detector is mounted on an electro-pneumatically controlled actuator which can be used to move the Daly detector in and out of the beam axis. To allow for this movement, and prevent any electrical short circuits, the voltages necessary to operate the detector are supplied by a flexible Kapton coated printed circuit board.

After first operation of the Daly detector it became clear that a fringe field compensation was required. To null the fringe magnetic field an opposing field was created by running a current through two coils of wire place on either side of the Daly detec-
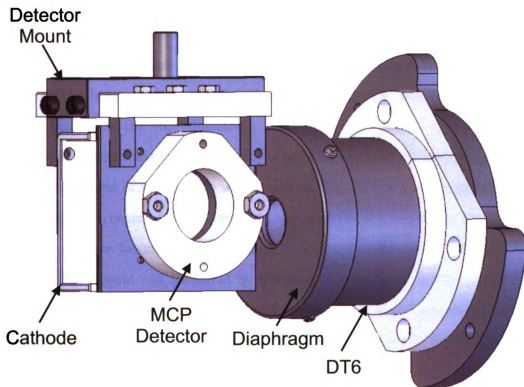
Figure 5.6: Mechanical drawing of the LEBIT Daly detector.
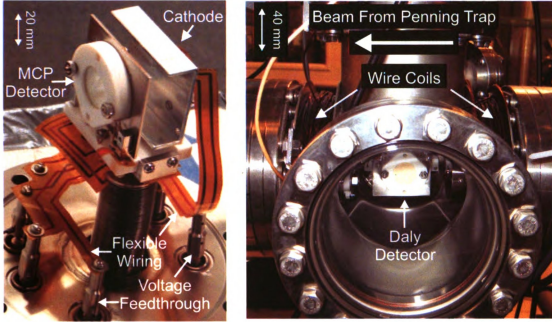
Figure 5.7: Left: Picture of the LEBIT Daly detector setup. Right: Picture of the vacuum chamber housing the Daly detector along with the fringe field compensation coils.

tor. These wire coils, similar to a Helmholtz coil, are shown in Figure 5.7. Using the calculated optimal voltages and adjusting the current through the wire coils while observing the beam spot on the phosphor screen, it is now possible to center the electron beam onto the MCP detector.

To obtain an estimate for the efficiency of our Daly detector the secondary-electron emission coefficient of the cathode was measured. The data was obtained by imping-ing a continuous beam of $^{39}K^+$ ions onto the cathode and measuring the resulting secondary electron beam current off the MCP detector's front plate. The rate of the incoming $^{39}K^+$ beam was measured by placing a high positive voltage on the front plate of the MCP detector to steer the incoming ions onto the cathode operated with a low voltage to prevent the emission of any secondary electrons. The ratio of these two measurements, the secondary-electron emission coefficient, as a function of the cathode voltage was already shown in Figure 5.5. The dashed line shows that for a cathode voltage of -5 kV a secondary-electron emission coefficient of $\gamma_e \approx 3$ is ob-

tained. Thus according to Equation 5.1 with a $\varepsilon_t \approx 85\%$ [16] the detection efficiency of the Daly detector is about 92%. This is comparable to the value predicted using the data from [18,79]. However, the detection efficiency of the Daly detector could be further improved by using an aluminium cathode with an oxidized layer enhanced by a plasma-anodization process.

Chapter 6

Time-of-Flight Mass Spectroscopy and Separation at LEBIT

Contaminant ion detection and removal are an important part of the LEBIT facility as the interaction of simultaneously stored ions with different masses in the Penning trap can cause systematic frequency shifts [65]. At the LEBIT facility, beam purification is accomplished in several ways as already discussed in Chapter 2. The first stage of beam purification is performed in the mass filtering section of the RFQ ion guides. The RFQ mass filter provides for a moderate suppression of neighboring mass (A±1) and an almost complete suppression of all other non-isobaric contaminants. In the beam cooler and buncher, weakly bound contaminant molecular ions can be broken into their constituents through collision induced dissociation (CID) with a buffer gas. Despite these mass filtering efforts, the CID products and highly abundant non-isobaric contaminant ions may still be present in the ion pulse ejected from the beam cooler and buncher. To limit the contaminants entering the Penning trap to isobars, these ion pulses are further purified using time-of-flight mass separation. Directly related to this is the ability to detect contaminant ions and determine their relative abundance by measuring their time of flight to the BOB5 MCP detector (see Figure 2.2). Based on these capabilities the LEBIT beam cooler and buncher along with the

following beam transportation, detection, and filtration system can be classified as a time-of-flight mass spectrometer and separator. The investigation and optimization of this system is the basis of this chapter.

The operation of the LEBIT beam cooler and buncher was briefly described in Section 2.2 of this thesis and more thoroughly explained in [45,51,58,80]. Originally, the beam cooler and buncher was not designed to be operated as a part of a time-of-flight mass spectrometer. It assumed this role only after the need for further beam purification and contaminant identification was discovered. Initial measurements performed with this system demonstrated that a single mass resolving power could not be attained. A time-of-flight distribution measured on the BOB5 MCP detector for the naturally abundant isotopes of krypton after ejection from the beam cooler and buncher before further improvements is shown in Figure 6.1. A mean time of $\bar{t} =$
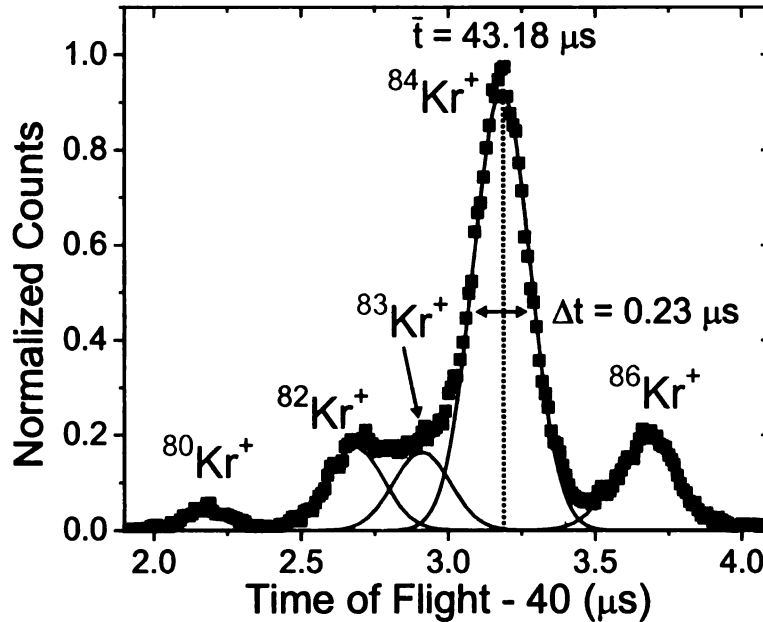
Figure 6.1: A time-of-flight distribution measured with the BOB5 MCP detector for the naturally abundant krypton isotopes performed during the initial investigation of the beam cooler and buncher's use as a time-of-flight mass spectrometer and separator.

43.18 μs and a pulse width (FWHM) of $\Delta t = 0.23$ μs was measured for the $^{84}Kr^+$ ions. This gives a mass resolving power of $R = m/\Delta m = \bar{t}/(2 \cdot \Delta t) \approx 90$ with which is insufficient to separate neighboring masses (e.g $^{82}Kr^+$, $^{83}Kr^+$, and $^{84}Kr^+$) of comparable intensities. In order to study the possibility of achieving a single mass resolving power, the ion pulse width's dependency on the ejection parameters of the beam cooler and buncher was investigated.

6.1 Basics of Time-of-Flight Mass Spectrometry and Separation

An idealized time-of-flight mass spectrometer [81] is shown in Figure 6.2. In this simplified system, ions are accelerated by an electric field created through the application of voltages $V0 > V1 > V2$ on the electrodes shown in the figure. This acceleration region, of length $2L$, is followed by a field-free region where ions are allowed to drift for a distance of length D. At the end of the drift region, ions are either impinged on an ion detector where their time of flight is recorded or sent into a mass filter where contaminant ions are removed based on their time of flight. Consider the case
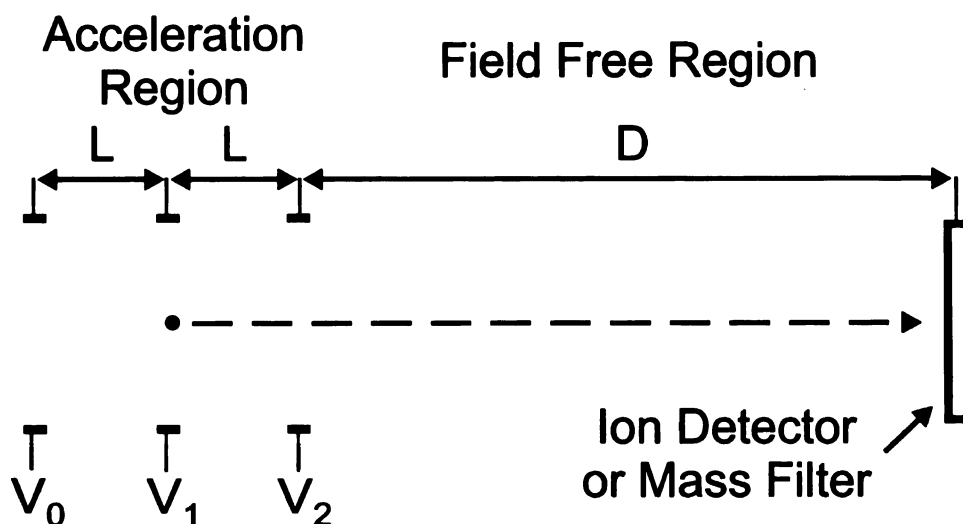
Figure 6.2: Schematic illustrating an idealized time-of-flight mass spectrometer.

where the voltages V0-V2 are chosen such that a constant accelerating electric field of strength E is created. An ion with mass m and charge q starting at rest in the center of the acceleration region reaches the end of the drift region in a time

$$t = \sqrt{\frac{2Lm}{qE}} + D\sqrt{\frac{m}{2qEL}} \propto \sqrt{m} \qquad (6.1)$$

that is proportionate to the square root of its mass. This dependency forms the basis of time-of-flight mass spectrometry and separation.

The time of flight given in Equation 6.1 is what would be obtained for all ions of the same mass in an ideal scenario. In reality, ions will have a range of initial velocities and positions that will lead to deviations from this ideal time of flight. For instance, ions stored in the trap section of the beam cooler and buncher are cooled to a thermal velocity through collisions with a buffer gas [80]. As these ions are confined in an approximately harmonic trapping potential they will have an axial velocity distribution with a standard deviation $\sigma_{\dot{z}}$ of

$$\sigma_{\dot{z}} = \sqrt{\frac{k_B T}{m}} \qquad (6.2)$$

where k_B is the Boltzmann constant and T is the temperature of the buffer gas. The thermal energy of the stored ions leads to an axial spatial distribution with a standard deviation σ_z of

$$\sigma_z = \sqrt{\frac{k_B T}{qk}} \qquad (6.3)$$

where k (approximately 0.02 V/mm^2 for the beam cooler and buncher) is a parameter describing the shape and depth of the trapping potential.

The effects of an initial spatial and velocity distribution on the measured time-of-flight spread of an ion pulse can be quantified. An ion at rest displaced axially by z_0

from the assumed center of the acceleration region has a time of flight of

$$t = \sqrt{\frac{2m(L \pm z_0)}{qE}} + D\sqrt{\frac{m}{2qE(L \pm z_0)}}. \qquad (6.4)$$

An ion starting from the center of the acceleration region with an initial axial velocity v_0 will arrive at the detector's position with a time of flight of

$$t = \sqrt{\frac{2Lm}{qE}}\sqrt{1 + \frac{v_0^2 m}{2qEL}} + D\sqrt{\frac{m}{2qEL}}\left(1 + \frac{v_0^2 m}{2qEL}\right)^{-1/2} \pm \frac{v_0 m}{qE}. \qquad (6.5)$$

Thus the time of flight obtained for a pulse of isobaric ions with a spread of initial velocities and positions will be distributed about the mean value given by Equation 6.1.

6.1.1 Time Focusing

To remove variations in the time of flight measured for a group of ions due to an initial spacial distribution time focusing techniques can be used. The term "time focus" is used to describe the position where the measured time-of-flight distribution for a group of ions is independent of their individual axial starting positions. Such a focus is created by the extracting electric field which imparts a higher kinetic energy on ions starting further away from the measurement point. The time of flight for two ions, with starting positions displaced from the central position of the acceleration region by $+z_0$ and $-z_0$ respectively, can be determined using Equation 6.4. The condition to obtain a time focus after a drift distance D with a single constant acceleration electric field of length L is

$$D = 2\sqrt{L^2 - z_0^2}. \qquad (6.6)$$

Since, the length of the acceleration region and the drift region are fixed, the time focus obtained in Equation 6.6 is of limited applicability.

In 1955, W. C. Wiley and I. H. McLaren created a time-of-flight system with

an increased time focusing capability [82]. They accomplished this by splitting the initial acceleration region into two consecutive constant electric fields with different strengths. The condition for time focusing with this system is

$$D = 2A_1 C \left(1 - \frac{1}{C + \sqrt{C}} \frac{A_2}{A_1} \right) \quad \text{where} \quad C = \frac{A_1 E_1 + A_2 E_2}{A_1 E1} \quad (6.7)$$

where A_1 and E_1 are the length and strength of the first electric field and A_2 and E_2 are the length and strength of the second electric field. As shown in Equation 6.7, the position of the time focus obtained for this system is independent of the ions' initial axial position z_0 and can be adjusted by changing the magnitude of the consecutive electric fields. The flexility of this system allows a time focus to be obtained at almost any distance from the starting point.

6.1.2   Energy Focusing

In the mass spectrometer shown in Figure 6.2, the effects of the ions' initial energy spread on the final time-of-flight distribution cannot be removed but can be significantly suppressed. This can be illustrated by considering the time of flight obtained for two ions starting from the same position with opposite initial axial velocities (v_0 and $-v_0$). Due to the direction-dependent term in Equation 6.5 the ions' time of flight will differ by

$$t_{tat} = \frac{2v_0 m}{qE}. \quad (6.8)$$

This value is also known as the turn-around-time (t_{tat}) of an ion and is defined as the time it takes an ion with an initial velocity ($-v_0$) opposite to the direction of its acceleration to return to its original position. The average turn-around-time for a distribution of ions determines the minimum obtainable pulse width (Δt_{min}) for the resulting time-of-flight distribution. Equation 6.8 shows that for a large initial electric field strength E the ions' average turn-around-time can be made relatively small. In a realistic setting the situation is more complicated as the voltages necessary

to create the initial electric field can not be generated instantaneously. The device used to supply the required voltages along with the capacitance of the electrode system dictates how fast these voltages can change. Assuming a linear change in voltage the electric field experienced by the ions as a function of time is

$$E(t) = \begin{cases} \frac{S_r}{L}t & \text{if } t \leq \frac{V}{S_r} \\ \frac{V}{L} & \text{if } t > \frac{V}{S_r} \end{cases}$$ (6.9)

where L is the length of the acceleration region, S_r is the device's slew rate, and V is the maximum voltage output of the device. Based on this electric field the minimum obtainable pulse width for an ion distribution can be approximated as

$$\Delta t_{min} \approx \begin{cases} \frac{2v_0 mL}{qV} & \text{if } S_r \gg \frac{qV^2}{2v_0 mL} \\ \frac{5}{2}\sqrt{\frac{v_0 mL}{qS_r}} & \text{if } S_r < \frac{4}{25}\frac{qV^2}{v_0 mL} \end{cases}$$ (6.10)

These equations show that for high slew rates the minimum obtainable pulse width is determined by the device's maximum output voltage and that for low slew rates it is determined by the magnitude of the slew rate itself.

For the beam cooler and buncher's time-of-flight system, assuming the use of power supplies with a relatively high slew rate, a minimum pulse width can be calculated explicitly from the standard deviation of the initial velocity distribution given in Equation 6.5. With this minimum pulse width of

$$\Delta t_{min} = \sqrt{\frac{4mk_B T}{q^2 E^2}}$$ (6.11)

and the mean time of flight ($\bar{t}$) from Equation 6.1 a maximum resolving power of

$$R = \frac{m}{\Delta m} = \frac{\bar{t}}{2\Delta t_{min}} = \frac{2L + D}{\sqrt{16L}}\sqrt{\frac{qE}{k_B T}}$$ (6.12)

70

can be formulated. This equation shows that the maximum obtainable resolving power of the beam cooler and buncher's time-of-flight system is determined not only by the strength of the initial electric field but also by the drift region's length and the temperature of the buffer gas. It should be noted that the resolving power given in Equation 6.12 is an approximation as the beam cooler and buncher's extracting electric field is more complicated than the one presented in Figure 6.2.

6.1.3 Beam Emittance

Beam emittance is a value that quantifies the "ease" with which beams can be manipulated and transferred between different devices [83]. In the field of Penning-trap mass spectrometry, the quality of the obtained cyclotron frequency resonance depends on the emittance of the ion pulse captured in the Penning trap. The emittance of an ion pulse and its relevance can be understood through the use of phase space diagrams. For the transverse phase space diagram, the magnitude of each ion's momentum and position along an axis perpendicular to the beam's direction of propagation are plotted at a given time. In a longitudinal phase space diagram, the energy in the direction of beam's propagation and time of flight of each ion are plotted at a given position. The area occupied by the ions in these diagrams is referred to as the transverse and longitudinal emittance, respectively. Assuming the ion pulse's position and momentum distributions can be described by a Gaussian function the shape of the ions' area in phase space will be elliptical.

Figure 6.3 shows the evolution of a transverse phase space ellipse through time and a longitudinal phase space ellipse through space. These ellipses can change in shape but their area or emittance will stay constant, provided that all applied forces are conservative and uniformly applied to all ions. In such a system, the spread in energy and momentum of an ion pulse will stay constant whereas its width in space and time can increase and decrease, as illustrated in Figure 6.3. The smallest obtainable value for an ion pulse's spatial or temporal width is determined by the pulse's emittance.

71
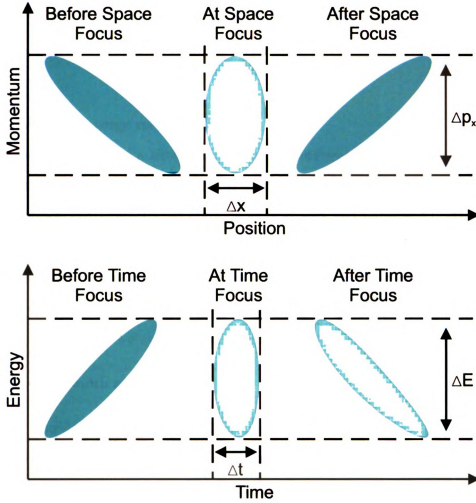
Figure 6.3: Phase space action diagrams showing the evolution of an ion pulse's transverse momentum versus position through time (top) and longitudinal energy versus time of flight through space (bottom).

When the traverse phase space ellipse achieves its minimum spatial spread Δx, the space focus, the ion distribution's transverse emittance can be expressed as

$$\xi_{trans} = \pi \Delta p_x \Delta x \tag{6.13}$$

where Δp_x is the ion pulse's spread in momentum. At the position where the longitudinal phase ellipse achieves its minimum width in time Δt, the time focus, the

longitudinal emittance of an ion pulse can be expressed as

$$\xi_{long} = \pi \Delta E_0 \Delta t \tag{6.14}$$

where ΔE_0 is the energy spread of the pulse.

For the evaluation of a time-of-flight mass spectrometer, the longitudinal emittance is the most relevant. The strength of the initial electric field (E) used to accelerate an ion pulse directly affects its energy spread and pulse width. The initial longitudinal spatial distribution (Δz) and momentum spread (Δp_z) for a group of ions accelerated by the electrode configuration shown in Figure 6.2 relates to the resulting energy spread as

$$\Delta E_0 = qE\Delta z \tag{6.15}$$

and the pulse's width as

$$\Delta t = \Delta p_z/(qE). \tag{6.16}$$

The product of these two equation shows that in an ideal scenario, the longitudinal emittance should be independent of the accelerating electric field. Thus for the beam cooler and buncher's time-of-flight system, the longitudinal emittance of an extracted ion pulse should be expressed as

$$\xi_{long} = \pi \Delta z \Delta p_z = \pi k_B T \sqrt{\frac{m}{k}} \tag{6.17}$$

in terms of initial trapping parameters given in Equations 6.2 and 6.3. However perturbations such as time dependent electric fields, non-harmonic trapping potentials, and collision with a buffer gas can result in distortions of an ion distribution's phase space ellipse and deviations from this ideal relationship.

6.2 Simulation of Ion Pulse Ejection from the Beam Cooler and Buncher

6.2.1 Setup

To investigate the time-of-flight spread of ion pulses ejected from the beam cooler and buncher, this system was simulated in SIMION [78]. The electrode geometry used for these simulations is shown in Figure 6.4. An initial distribution of 990 $^{39}K^+$ ions was generated in the beam cooler and buncher using a hard-sphere, elastic, ion-neutral collision model made for SIMION. Ions were cooled in the beam cooler and buncher with a helium gas at a temperature of 296 K and pressure of $0.5 \cdot 10^{-3}$ mbar for a time of 3 ms. The voltages applied to the trap electrodes for the duration of this cooling process are shown in Table 6.1. To eject ions from the beam cooler and buncher and to account for the slew rate, the voltages applied to the trap electrodes were linearly increased from the values given in Table 6.1 until the desired extraction voltage was reached. During the ejection process the pressure in the beam cooler and buncher was held at $0.05 \cdot 10^{-3}$ mbar using the above collision model.

The optimization process performed in these simulations was based on the time and velocity focusing techniques discussed in Sections 6.1.1 and 6.1.2. To achieve the maximum mass resolving power the ion pulses ejected from the beam cooler and buncher should obtain a time focus at BOB5. This requires that at least a dual acceleration scheme is used to extract these ions. To create two independent consecutive electric fields and to reduce the number of optimization parameters the trap electrodes were conceptually divided into two groups: the first acceleration region composed of Trap4, Trap5, and Trap6 and the second acceleration region composed of Trap7, BunEX1, and BunEX2. This division was made based on the fact that the potential well used to confine ions in the trap is centered about the Trap5 electrode. The electric field strength in the first E_1 and second E_2 acceleration regions were

74
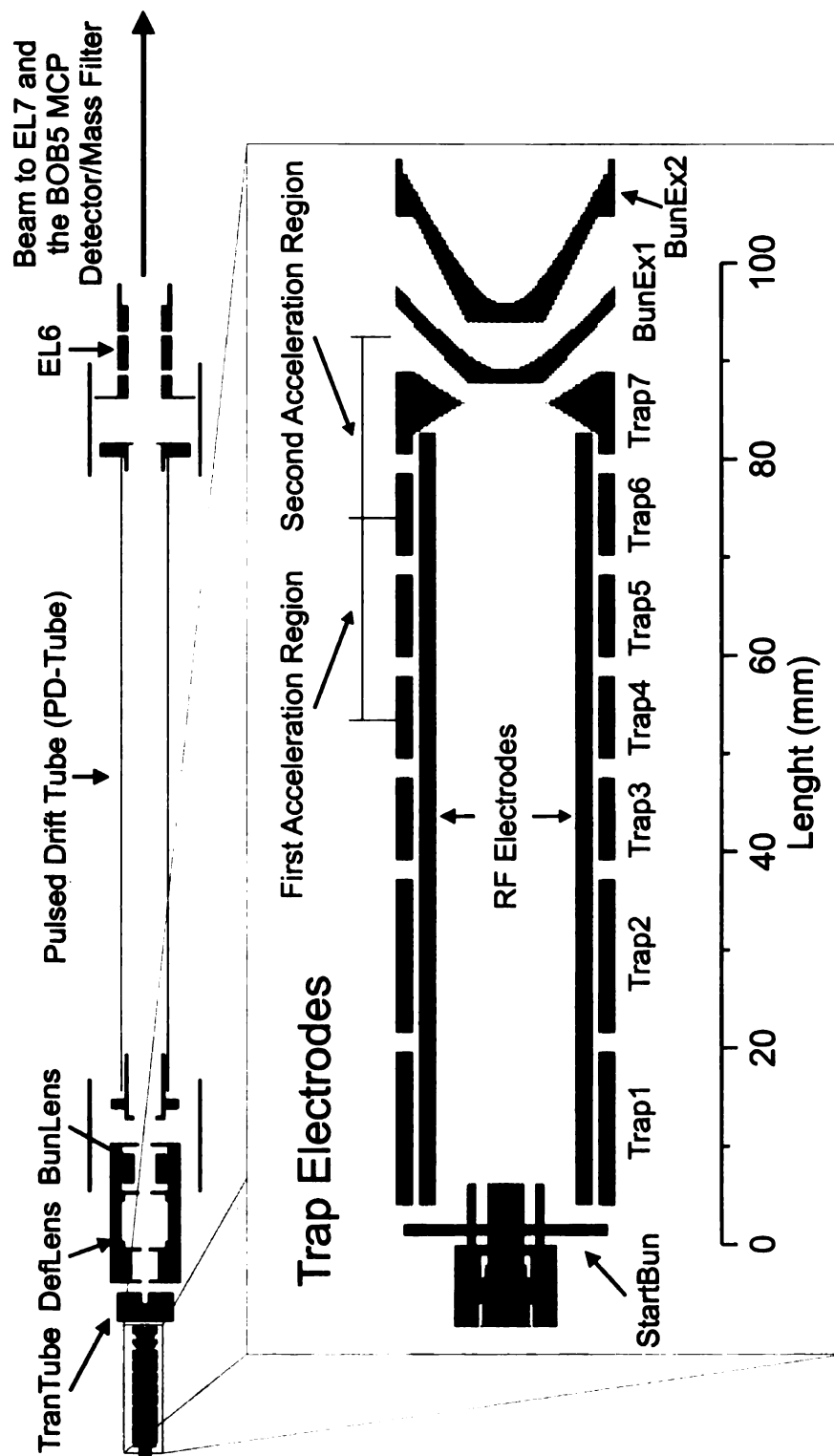
Figure 6.4: Electrode geometry of the beam cooler and buncher and the following transportation optics. An enlarged view of the beam cooler and buncher's trap section is also shown.

75

Table 6.1: The voltages applied to the beam cooler and buncher's trap electrodes during the cooling process. Also shown are two settings used for the ejection of ions from the trap that were optimized for a time focus at BOB5 with an initial electric field strength $E_1 \approx 1.9$ V/mm and $E_1 \approx 6.8$ V/mm.

Electrode	Trapping	Ejection	
		$E_1 \approx 1.9$ V/mm	$E_1 \approx 6.8$ V/mm
RF Amplitude	95 V	95 V	95 V
DC Offset	-30.9 V	-30.9 V	-30.9 V
Pressure	$0.5 \cdot 10^{-3}$ mbar	$0.05 \cdot 10^{-3}$ mbar	$0.05 \cdot 10^{-3}$ mbar
StartBun	-27.5 V	-27.5 V	-27.5 V
Trap1	-27 V	30 V	30 V
Trap2	-28 V	110 V	110 V
Trap3	-30 V	110 V	110 V
Trap4	-35 V	100 V	400 V
Trap5	-40 V	-50 V	-50 V
Trap6	-35 V	-120 V	-400 V
Trap7	-10 V	-120 V	-400 V
BunEx1	-8 V	-115 V	-400 V
BunEx2	N/A	-300 V	-600 V
TranTube	N/A	-740 V	-800 V
DefLens	N/A	-2040 V	-2040 V
BunLens	N/A	-3080 V	-3080 V
PD-Tube	N/A	-2040 V	-2040 V
EL6	N/A	-3240 V	-3240 V
EL7	N/A	-5970 V	-5970 V

determined from the average change in potential along the trap's axis between the first and last electrode of each region.

6.2.2 Results

The electric field strength E_1 was optimized to reduce the effects of the trapped ions' initial energy spread on their width in time after being extracted from the beam cooler and buncher. Extraction from the trap was simulated using two ions starting from the center of the Trap5 electrode both with an initial thermal velocity (T = 296 K) oriented along the trap's axis but in opposite directions. The time of flight difference between these two ions was determined as a function of the voltage difference applied
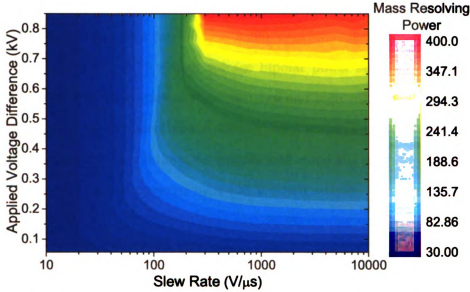
Figure 6.5: The maximum obtainable mass resolving power (color scale) for $^{39}\text{K}^+$ ions ejected from the beam cooler and buncher as a function of the voltage difference applied between the Trap4 and Trap6 electrodes along with the slew rate with which this voltage was generated.

(ΔV) between the Trap4 and Trap6 electrodes as well as the slew rate used to generate this voltage. For these simulations the Trap5 electrode was set to ground, and the Trap4 and Trap6 electrodes were set to $+\Delta V/2$ and $-\Delta V/2$, respectively. From the difference and the average of the two ions' time of flights a maximum obtainable resolving power was calculated. The results of this simulation are shown as a color contour plot in Figure 6.5. The values obtained in this simulation are for an idealized scenario but still provide valuable information about the extraction of thermalized ion distributions from the beam cooler and buncher.

In the original experimental setup for the beam cooler and buncher, the voltages applied to the trap electrode were supplied by a series of bipolar switchable power supply that could output up to ± 120 V and had a slew rate of $S_r \approx 45$ V/μs. The switching curve, for this type of power supply, as measured on a digital scope is shown in Figure 6.6. With a slew rate of $S_r \approx 45$ V/μs, Figure 6.5 shows that the mass resolving power obtained is almost independent of the applied voltage and limited mainly by the slew rate of the power supply itself. Fortunately, a higher voltage

bipolar power supply that could generate up to ±400 V and a high voltage fast MOSFET switch with a slew rate of $S_r \approx 8{,}000$ V/μs were also available. The output of such a switch powered by a high voltage bipolar power supply is also shown in Figure 6.6. With the integration of these switches and high voltage power supply into the LEBIT system an increased mass resolving power could be achieved. Based on this information all further simulations were performed using the operational parameters of a fast MOSFET switch powered by a 400 V power supply.
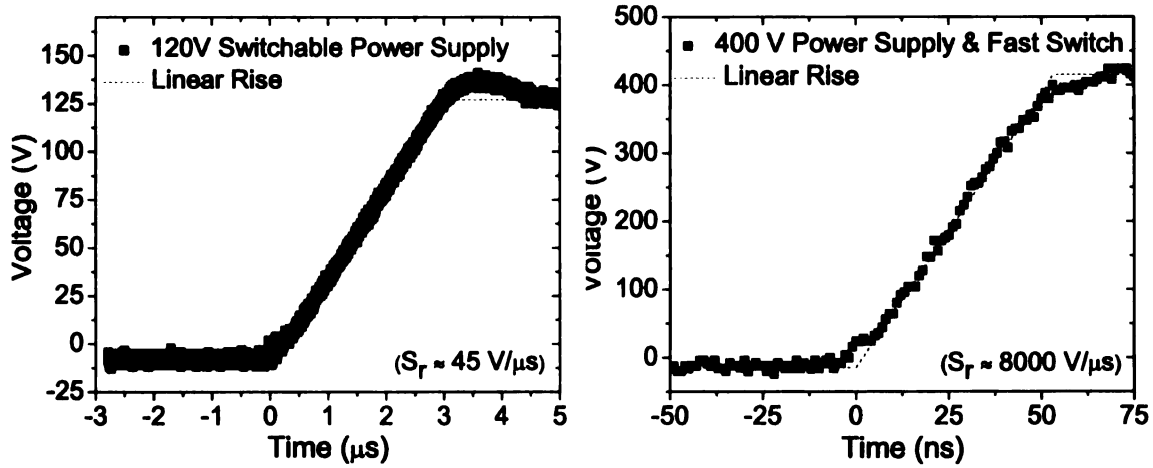
Figure 6.6: Left: Output of the 120 V bipolar switchable power supply while switching from 0 V to 120 V, and linear approximation of this data. Right: Output of a high voltage fast MOSFET switch powered by a 400 V bipolar power supply while switching from 0 V to 400 V, and a linear approximation of this data. Both curves were measured using a digital oscilloscope.

The electric field strength E_2 was optimized to obtain a time focus at BOB5. The optimal voltages for Trap7, BunEX1, and BunEX2 were determined using the complete ion distribution presented in Section 6.2.1. For these simulations the electric field strength E_1 was set to 6.8 V/mm, the field strength obtained with the 400 V power supplies at their maximum voltage (±400 V). Figure 6.7 shows the individual calculated time of flights for the ejected ions to BOB5 as a function of their initial positions in the trap and for electric field strengths of $E_2 = 1$ V/mm, 20 V/mm, and 50 V/mm. From these results it can be seen that a time focus is obtained at BOB5
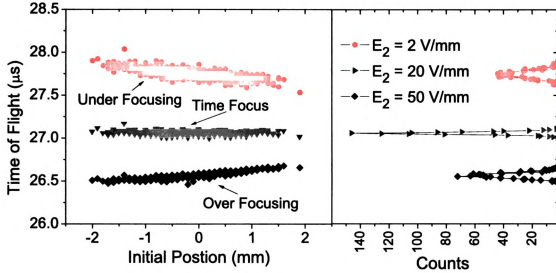
Figure 6.7: Left: Calculated ion time of flight to BOB5 obtained depending on the ions' initial position in the trap and the electric field strength E_2. Right: A histogram of the ions' time of flight to BOB5.

with $E_2 = 20$ V/mm. A similar procedure was performed with $E_1 = 1.9$ V/mm, for which a time focus at BOB5 was obtained with $E_2 = 15$ V/mm. The voltages applied to the trap electrodes and the potential created along the axis of the trap for both settings are shown in Table 6.1 and Figure 6.8, respectively. In simulation, a resolving power of $R \approx 280$ and $R \approx 110$ were obtained with the settings optimized for $E_1 = 6.8$ V/mm and $E_1 = 1.9$ V/mm respectively.
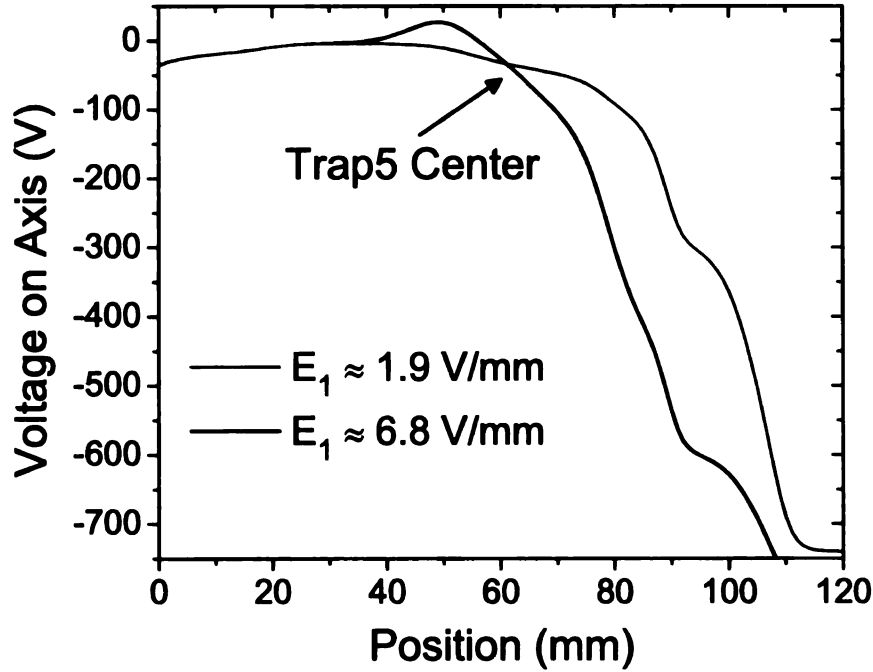
Figure 6.8: Comparison of the potentials created along the axis of the trap for the two optimized voltage configurations.

6.3 Experimental Study of Ion Pulse Ejection from the Beam Cooler and Buncher

Based on the results of the simulations presented in the previous section the power supplies for the Trap4, Trap6, Trap7, and BunEx1 electrodes were upgraded to a set of high voltage switches, each powered by two channels of a 400 V bipolar power supply. Experimental studies were then performed to determine the mass resolving power and longitudinal emittance of ion pulses produced by this system.

The simulated ion pulses were able to very well reproduce properties of experimental data obtained with this upgraded system. Figure 6.9 shows the measured and simulated mean time of flight and width in time (FWHM) of $^{39}K^+$ ion pulses measured on the BOB5 MCP detector as a function of the voltage difference between Trap4 and Trap6 electrodes. For these measurements the electric field strength E_2 was held constant at 20 V/mm, and a helium buffer gas at T = 296 K was used in the
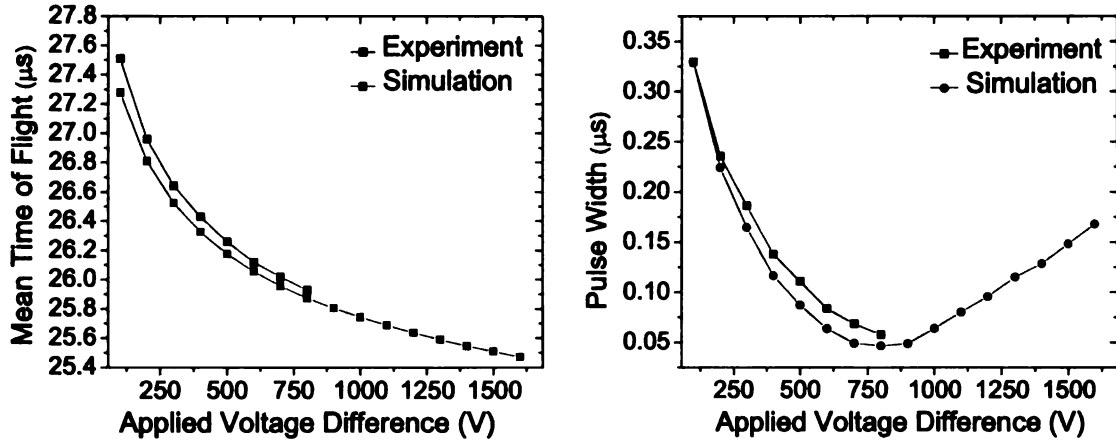
Figure 6.9: Comparison of simulated and experimental values obtained for the mean time of flight (left) and pulse width (right) observed at BOB5 for $^{39}K^{+}$ ion pulses ejected from the beam cooler and buncher as a function of the applied voltage difference between the Trap4 and Trap6 electrodes.

beam cooler and buncher. The largest source of error in the experimental measurements was the width of the single ion pulses measured on the BOB5 MCP detector (FWHM $\approx$ 10 ns). As the full analog signals were recorded for these measurements the finite width of the single ion pulse resulted in an increase of about 10 ns in the measured pulse width of the full ion distribution. Another possible source of error is that in simulation ions were ejected at same RF phase whereas in experiment ions were ejected at multiple phases of the RF. Simulation results for an electric field strength E_1 beyond those presently achievable with the 400 V power supplies are also shown in Figure 6.9; they indicate that going to an electric field strength $E_1 >$ 6.8 V/mm alone would not increase the mass resolving power at BOB5. A further improvement of the mass resolution would probably require the use of faster switches and higher voltages for all trap electrodes or a lower temperature buffer gas in the beam cooler and buncher.

6.3.1 Ion Detection and Removal

Time-of-flight distributions measured on the BOB5 MCP detector for krypton and potassium isotopes, are shown in Figure 6.10. These distributions were measured using the ejection settings optimized for an electric field strength $E_1 = 6.8$ V/mm, given in Table 6.1. For $^{39}\text{K}^+$ and $^{85}\text{Rb}^+$ ions resolving powers of R $\approx$ 220 and 200 were obtained. The agreement of these values confirms that the resolving power is to the first order mass independent. Both values are approximately a factor of 2.5 times higher than the resolving power obtained during the initial investigation of the system (see Figure 6.1) and are now sufficient to resolve the isotopes of krypton (i.e. $^{82}\text{Kr}^+$ and $^{83}\text{Kr}^+$). The disagreement of the measured resolving powers with the simulated one (R = 280) is most likely due to the error associated with measurements performed on the BOB5 MCP detector and the single-phased ejection used in the simulations.
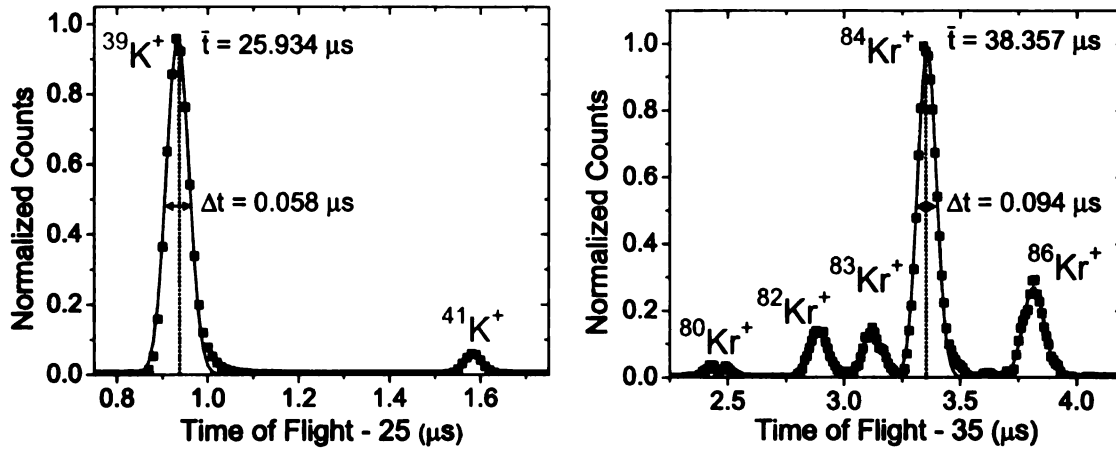
Figure 6.10: Ion pulses detected on the BOB5 MCP detector for potassium (left) and krypton (right) isotopes using the ejection voltages optimized for an electric field strength $E_1 = 6.8$ V/mm.

With the $E_1 = 6.8$ V/mm ejection settings the performance of the time-of-flight mass filter was investigated using krypton isotopes. The filtering mechanism of our time-of-flight mass filter is a pulsed deflector, the operation of which is depicted in Figure 6.11. To perform a mass scan with this deflector it was set to a high deflection voltage $V_{deflection}$ to eject ions from the system except for a time of 300 ns during

Io

Io

Ion

Deflector

Fig
abu
the

wh

en

an

of

tra

A

mo
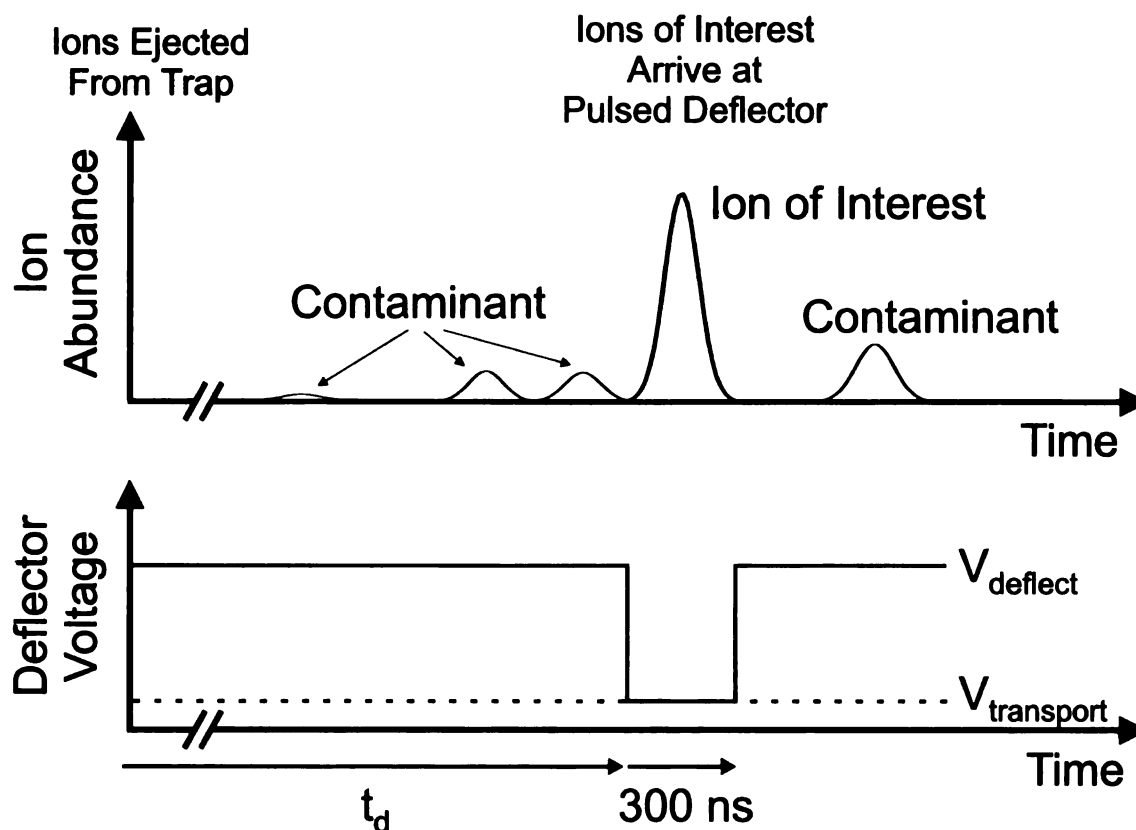
Figure 6.11: Two time lines, one for the deflector's voltage and the other for the ion abundance at deflector's location, illustrating the operation of a pulsed deflector as the filtering mechanism in a time-of-flight mass filter.

which the voltage was switched to a low transport voltage $V_{transport}$ to allow ions to enter the Penning trap. The time between ejection from the beam cooler and buncher and switching to $V_{transport}$, which we call t_d, can be adjusted depending on the mass of desired isotope. By changing the deflector's start time t_d and counting the ions transported to the BOB6 MCP detector the plot shown in Figure 6.12 was obtained. A gate start time t_d properly calibrated for $^{83}Kr^+$ suppressed $^{82}Kr^+$ and $^{84}Kr^+$ by more then a factor of a 100.
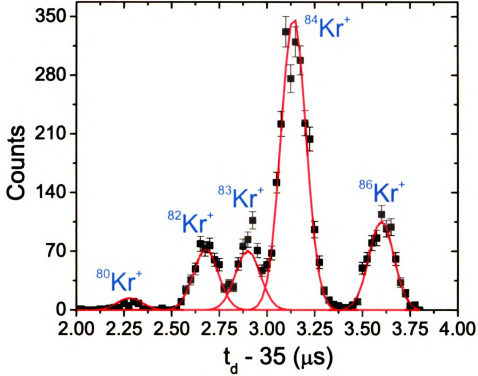
Figure 6.12: Mass scan of krypton isotopes performed by changing the time-of-flight mass filter's start time t_d and detecting the transported ions on the BOB6 MCP detector.

6.3.2 Longitudinal Emittance

To experimentally determine the longitudinal emittance of ion pulses ejected from the beam cooler and buncher their energy spread and pulse width were measured. These measurements were performed with a ^{39}K ion beam and for a helium buffer gas at temperature of $T \approx 130$ K and 250 K in the trap section of the beam cooler and buncher. This temperature was determined using a thermocouple located near the center of the trap. The widths of the ^{39}K ion pulses were measured on the BOB5 MCP detector and the results are shown in Figure 6.13. To determine the pulse's energy spread a retardation technique was used. Instead of detecting ions at BOB5 they were allowed to pass through the Penning trap and were detected with the MCP detector in BOB6. For these measurements, all electrodes of the Penning trap were put on a potential V_p which was ramped. The number of ions transmitted through the

Penning trap was then measured as a function of V_p. In order to extra the ions' energy spread these transmission curves were fitted with an integrated Gaussian function. The data obtained as a result of this process are shown in Figure 6.14.
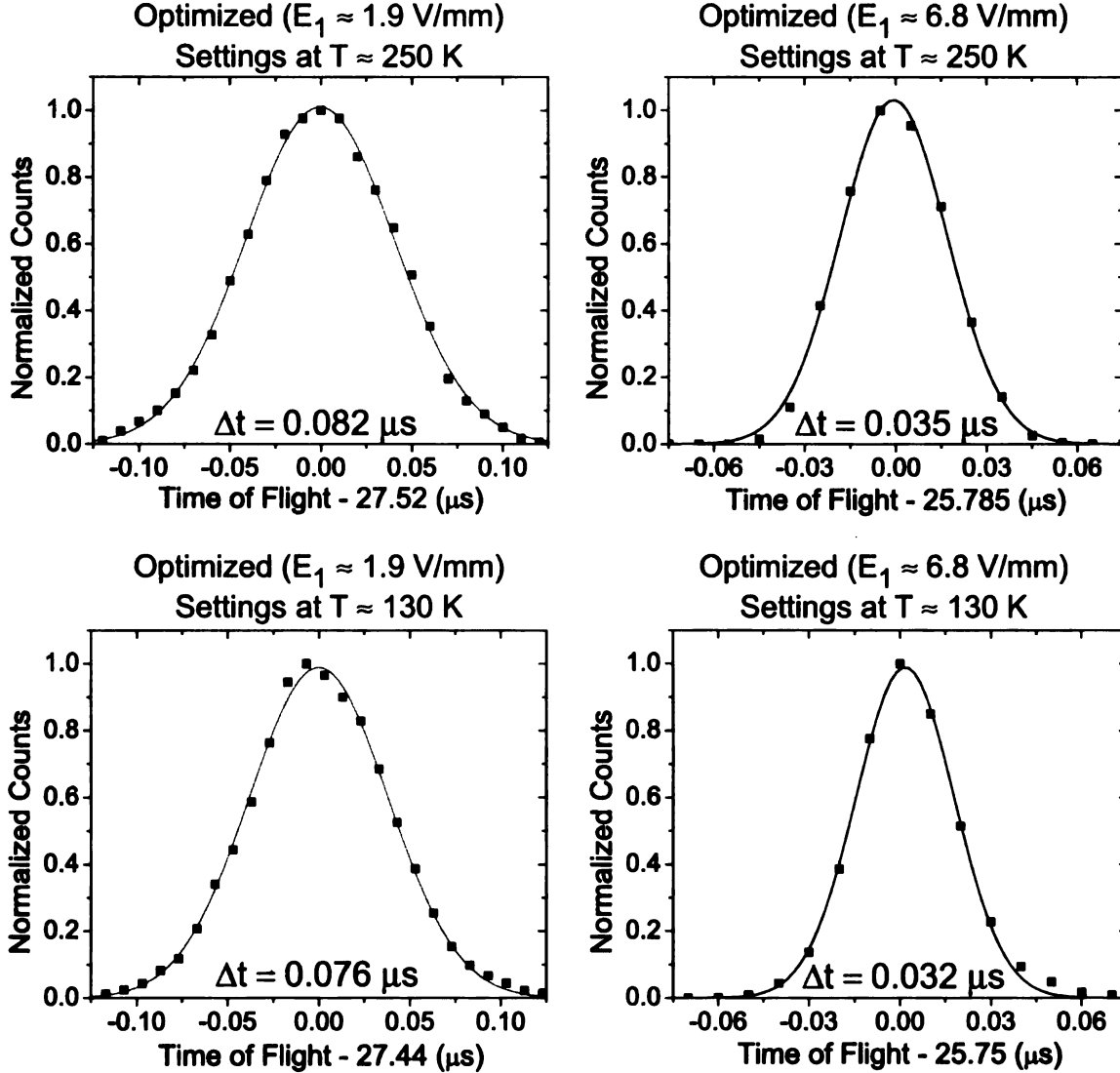
Figure 6.13: Time-of-flight distributions and pulse widths measured on the BOB5 MCP detector for ^{39}K$^+$ ion pulses ejected from the beam cooler and buncher for different ejection settings and buffer gas temperatures.

Assuming a time focus is achieved at BOB5, one can determine the longitudinal emittance from the pulse width and energy spread values presented in Table 6.2. The emittances listed in the table are an upper bound on the longitudinal emittance although the agreement of the experimental and simulated pulse widths shown in Figure 6.9 supports this method of determining the longitudinal emittance. As predicted
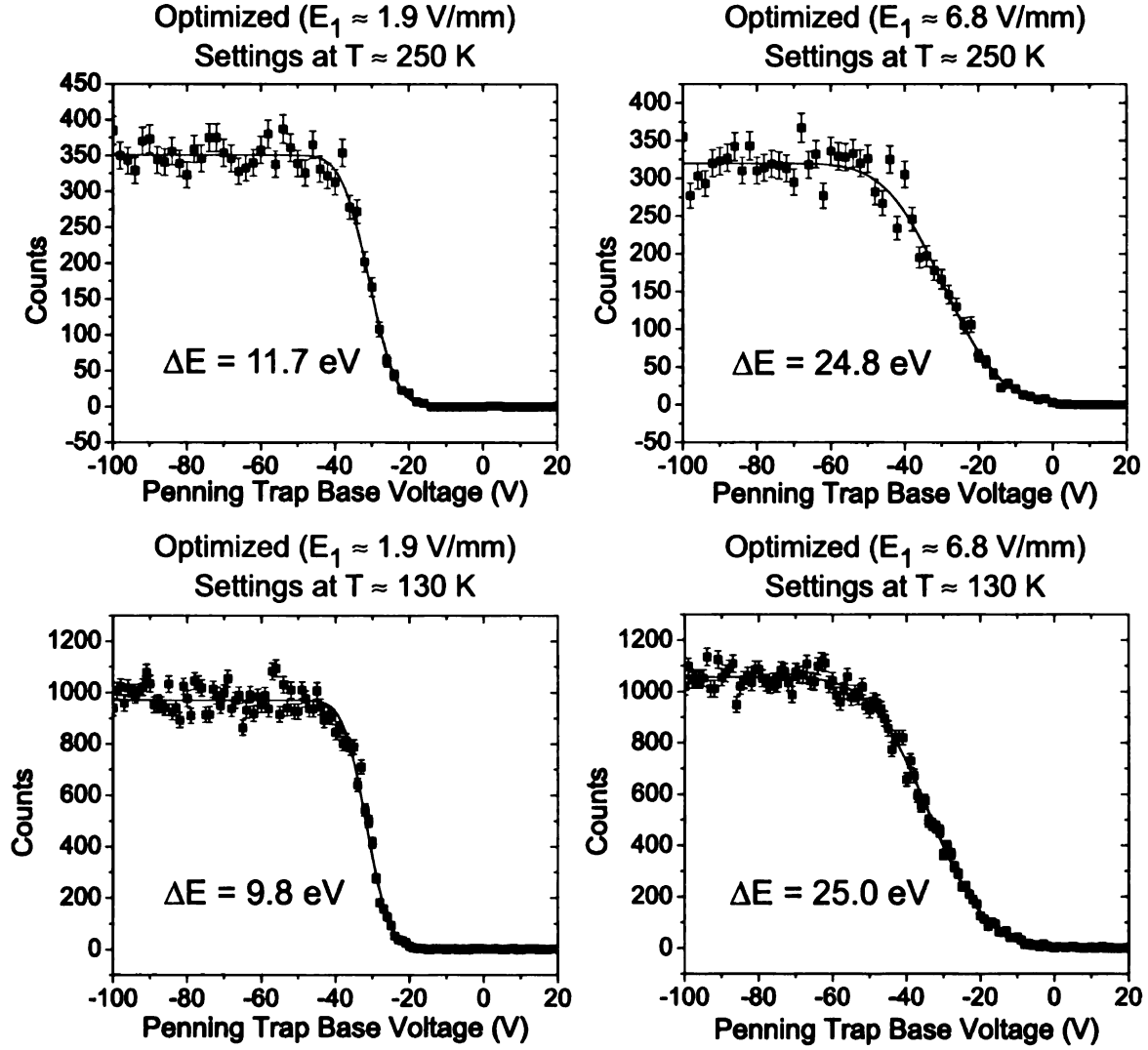
Figure 6.14: Integrated beam energy profile observed on the BOB6 MCP detector for ^{39}K $^+$ ion pulses ejected from the beam cooler and buncher for different ejection settings and buffer gas temperatures.

by Equation 6.17 the values shown in Table 6.2 for the two different ejection electric fields are in good agreement. However, the average longitudinal emittance does not decrease as expected with the temperature. We would expect a decrease in the longitudinal emittance by a factor of 1.9 when reducing the temperature from $T = 250$ to $T = 130$ K; instead we only observed a change of 1.18. This could be explained by the errors mentioned previously in the Section 6.3 or an error in the temperature reading. Another possible explanation is poor injection into the Penning trap which could cause an increase in the measured energy spread.

Table 6.2: Pulse width Δt, energy spread ΔE, and longitudinal emittance ξ_{long} obtained for the different beam cooler and buncher ejection settings given in Table 6.1 and buffer gas temperature T. The pulse width Δt and energy spread ΔE are quoted as a 2σ width whereas the longitudinal emittance is given as the area of the 2σ confidence ellipse.

Setting	T	Δt	ΔE	ξ_{long}
$E_1 \approx 1.9$ V/mm	130 K	0.076 μs	9.8 eV	0.75 π eV·μs
$E_1 \approx 6.8$ V/mm	130 K	0.032 μs	25.0 eV	0.80 π eV·μs
$E_1 \approx 1.9$ V/mm	250 K	0.082 μs	11.7 eV	0.96 π eV·μs
$E_1 \approx 6.8$ V/mm	250 K	0.035 μs	24.8 eV	0.87 π eV·μs

Chapter 7

Simulations of a Multipass Time-of-Flight Mass Spectrometer

The current mass filtering techniques applied to the beam entering the Penning trap are inadequate to suppress isobaric molecular contaminants. To separate a molecular contaminant ion of the same mass number as a stable or unstable isotope typically requires a mass resolving power of R (FWHM) $= m/\Delta m > 1{,}000$. This fact can be seen in Figure 7.1 which shows the mass difference between possible isobaric molecular contaminants and isotopes of interest along the N = Z line. In the Penning trap, isobaric contaminant ions can be removed, but only after being identified. Unfortunately, this process can be time consuming. One solution is the installation of a multipass time-of-flight (MTOF) mass filter [84]. In such a device ions are isochronously reflected between two electrostatic mirrors to achieve an increased flight path and a mass resolving power of $R > 10{,}000$ [85–87]. In this chapter, simulations for the addition of such a device to the LEBIT facility are discussed.
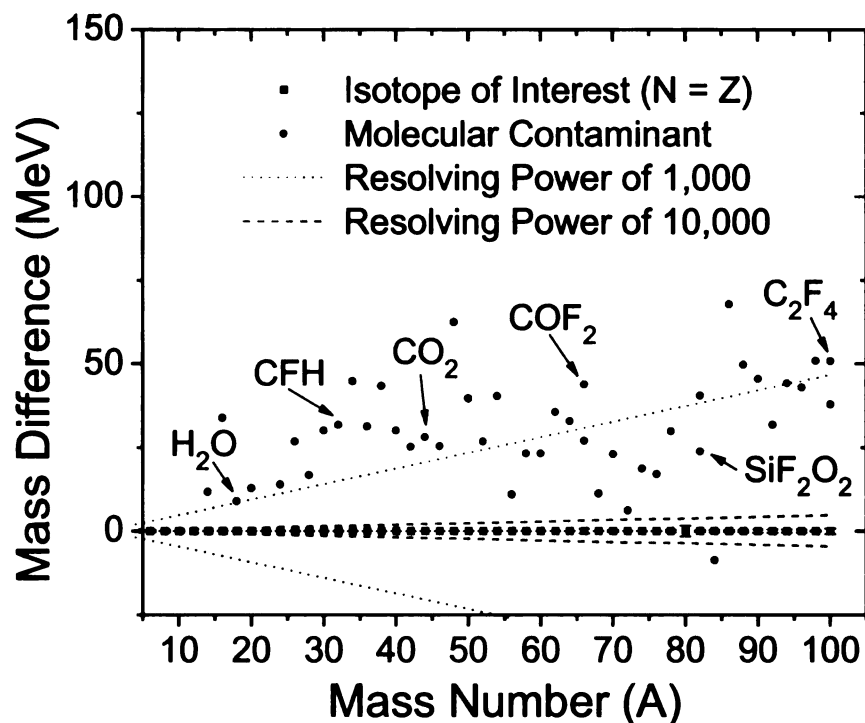
Figure 7.1: Plot showing the mass difference between stable isobaric molecular contaminant ions and rare isotopes along the N = Z line. The presented contaminants are a combination of observed (labeled) and possible candidates. The dotted and dashed lines demarcate the mass resolving powers provided by R = 1,000 and 10,000.

7.1 MTOF Basics

In the field of time-of-flight mass spectrometry, a device known as a "reflectron" or single-pass time-of-flight mass spectrometer has long been in use to reduce the effects of an ion packet's energy distribution on its time of flight post-acceleration [88]. A reflectron is an electrostatic mirror composed of a series of ring-shaped electrodes. A schematic of a reflectron and its basic operation is depicted in Figure 7.2. On the individual ring electrodes voltages (V1-V8) are placed to create a decelerating electric field which reverses the velocity of an incoming group of ions. In the top figure, ions leaving the pulsed source enter the reflectron and then are reflected back onto an ion detector or a mass filter. The distance d the ions penetrate into the mirror operated
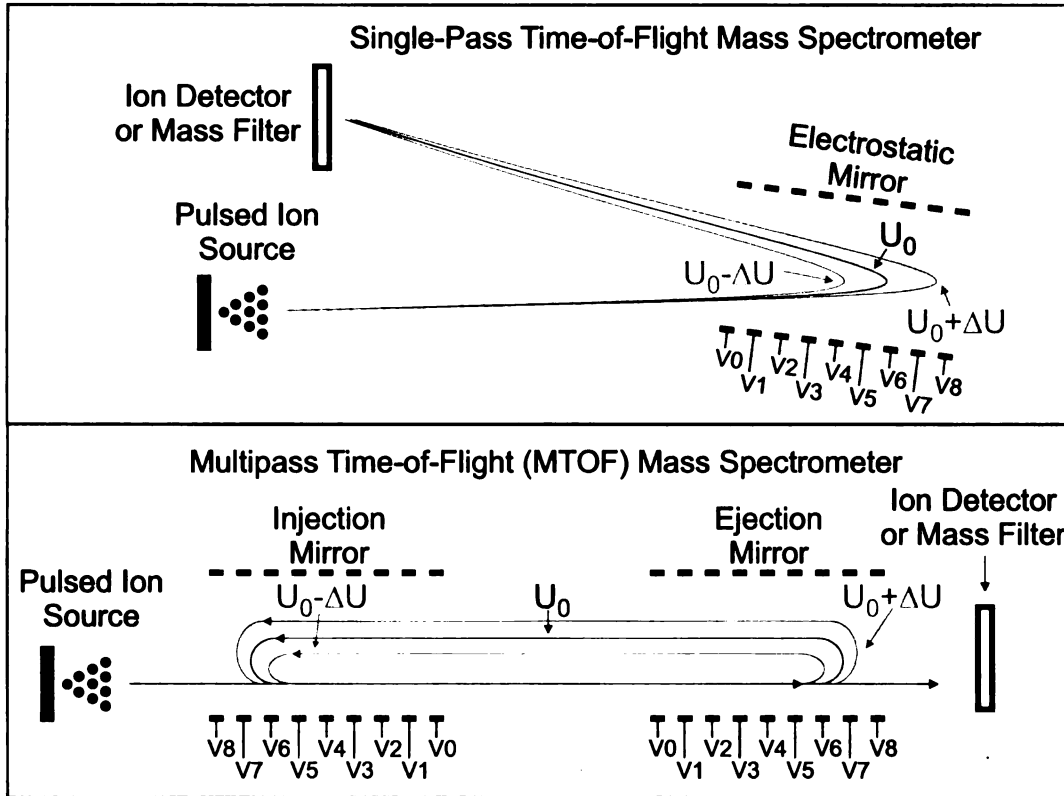
Figure 7.2: Schematic showing a single-pass (top) and multipass (bottom) time-of-flight mass spectrometer. Also shown are the trajectories of ions with kinetic energies of $U_0 - \Delta U$, U_0, and $U_0 + \Delta U$.

with a constant decelerating electric field of magnitude E depends on their kinetic energy U_0:

$$d = \frac{U_0}{qE} \tag{7.1}$$

The turn-around-time t_{tat} for the same ion is given by

$$t_{tat} = \frac{\sqrt{2mU_0}}{qE}. \tag{7.2}$$

Equation 7.2 relates the time it takes an ion to pass through the mirror to its incoming energy. Thus the reflectron's electric field can be adjusted to achieve an isochronous, or energy independent, mode of operation [81,88]. To obtain a higher degree of control over the mirror's electric field some designs incorporate grids which slightly reduces

the

era

Sec

on

sio

bet

set

tio

the

Th

fro

ally

flig

ma

ele

pro

opt

has

the

7.

7.2

The

This

of t

reso

the device's transmission efficiency. Most reflectrons are operated with a dual decel-eration region with properties similar to the dual acceleration region described in Section 6.1. In this configuration, a 2nd order energy focusing with a mass resolution on order of R = 5,000 has been achieved [81,88].

The multipass time-of-flight (MTOF) mass spectrometer [84] is a natural exten-sion of the reflectron. In an MTOF (depicted in Figure 7.2), a group of ions is reflected between two electrostatic mirrors. Initially, the injection mirror's ring electrodes are set to a transport voltage to allow ions from the source to enter the system. The ejec-tion mirror's ring electrodes, on the other hand, are held at a reflection voltage. Once the ions are at the mid-point of the MTOF the injection mirror's voltages are raised. The ions are then allowed to reflect between the two mirrors for N laps and ejected from the system by lowering the voltages on the ejection mirror's ring electrodes. Ide-ally, the ion pulse's width in time should stay constant while the pulse's mean time of flight increases linearly with the number of laps. This gives the MTOF an enhanced mass resolving capability over a linear mass spectrometer or a reflectron. The optimal electrode and voltage configuration of an MTOF are determined through a dynamic process of adjustment accompanied by an evaluation of the system's time-of-flight optical aberrations [84,89]. A group at the Oak Ridge National Laboratory (ORNL) has developed an optimization program to achieve to a 5th order minimization of their MTOF's time-of-flight abberations and a mass resolution of R = 110,000 [85].

7.2 The LEBIT MTOF Mass Filter

7.2.1 Design

The MTOF design for use at LEBIT was based on a design from ORNL [85,89,90]. This design was modified to met the performance requirements and spacial constraints of the LEBIT facility. First to suppress isobaric contamination, we require a mass resolving R > 10,000; clearly the ORNL design is more than sufficient. Second, the
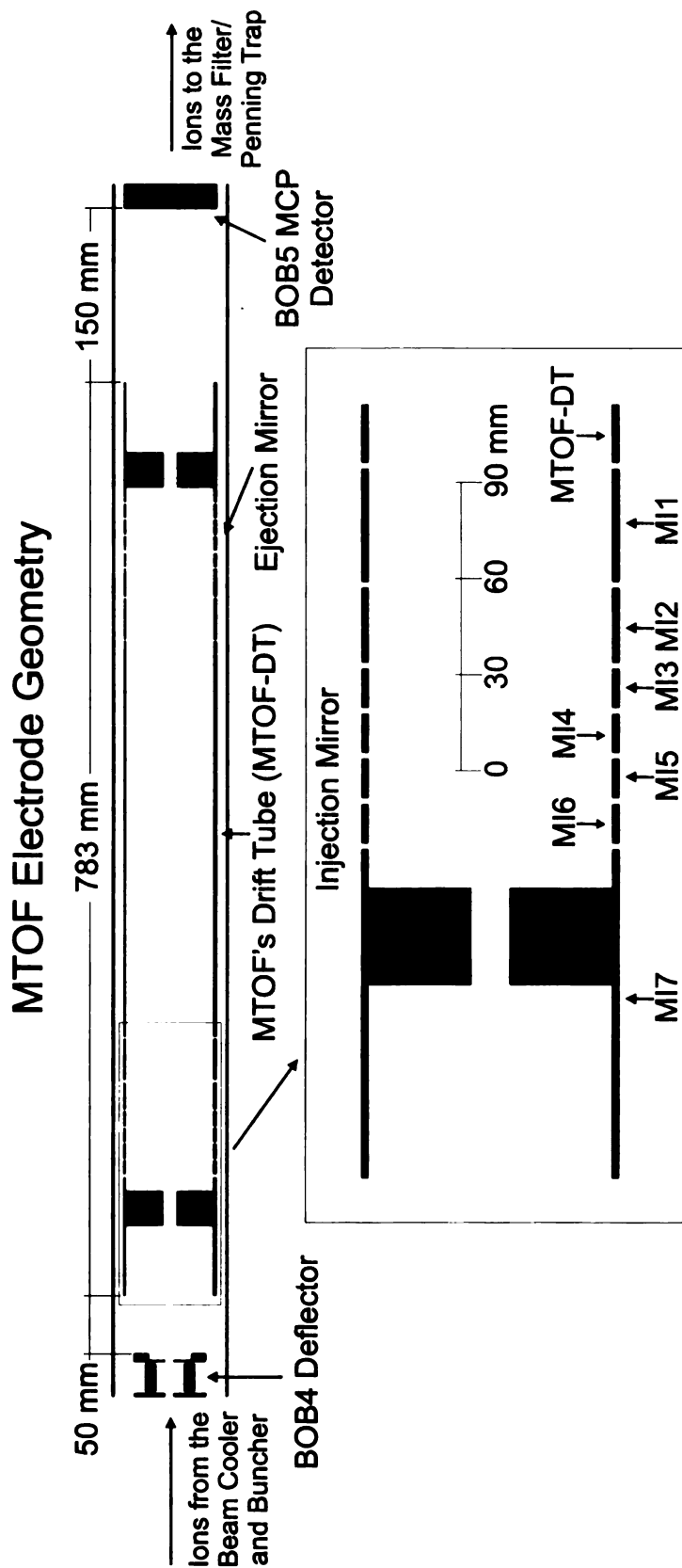
Figure 7.3: Electrode geometry and dimensions of the LEBIT MTOF design including an enlarged view of the injection mirror.

transmission must be as high as possible; therefore, the two grids present in the ORNL design at the end of each mirror were removed. Also, to avoid reconstruction of the beam line, the LEBIT MTOF must fit between BOB4 and BOB5 (see Figure 2.2). Last, any increase in the longitudinal emittance must be minimized.

The modified ORNL MTOF design is shown in Figure 7.3. In this figure, the injection mirror is composed of the electrodes labeled as MI1-MI7. Due to space constraints the ejection mirror's electrodes are not labeled but as it's a replica of the entrance mirror its electrode will be refered to as ME1-ME7 with the same relative assignments. In this design, the Einzel lens located between BOB4 and BOB5 (EL7) was replaced with two separate lens (MI1 and ME1). These electrodes were used to focus the beam as it enters and exits each respective mirror and to provide the tighter beam focusing required to achieve stable ion trajectories in the MTOF. However, if found necessary EL7 may be retained. At the end of each mirror, the ions obtain their lowest overall energy and thus are the most sensitive to optical abberation. To remove the need for a gridded electrode in this region a 12 by 30 mm cylindrical diaphragm along with a 60 mm overhang was added to the end electrode of each mirror.

7.2.2   Simulations

Simulations of the LEBIT MTOF design were performed at MSU using SIMION [78] and at ORNL using their ray tracing and optimization program (see Appendix C). For the simulations performed using SIMION the electrode geometry for the beam cooler and buncher shown in Figure 6.4 and the MTOF electrode geometry shown in Figure 7.3 were used. A thermalized distribution of $^{39}K^+$ ions was generated in the trap section of the beam cooler and buncher using the method described in Section 6.2. Cooling was performed in two different trapping potentials created by the trap electrode voltages given in Tables 7.1 and 7.2 to cover a range of initial longitudinal and transverse emittances. The voltages given in Table 7.1 were used to produce a "low" emittance ion pulse with a longitudinal emittance of 0.45 π eV·μs, and a

transverse emittance of 3.6 π mm·mrad. A "high" emittance pulse with a longitudinal emittance of 0.8 π eV·μs, and a transverse emittance of 5.8 π mm·mrad was produced with the trapping voltages given in Table 7.2.

Table 7.1: Left: Voltages applied to the beam cooler and buncher, transportation lenses, and MTOF for cooling and ejection of an ion distribution with a longitudinal emittance of 0.45 π eV·μs, and a transverse emittance of 3.6 π mm·mrad. Right: Voltages applied to the MTOF's electrode depending on the number of laps N_{laps}.

Electrode	Trapping	Ejection
RF Amp.	95 V	95 V
StartBun	-27.5 V	-27.5 V
Trap1	-27 V	30 V
Trap2	-28 V	110 V
Trap3	-30 V	110 V
Trap4	-35 V	400 V
Trap5	-40 V	-50 V
Trap6	-35 V	-400 V
Trap7	-10 V	-400 V
BunEx1	-8 V	-400 V
BunEx2	N/A	-600 V
TranTube	N/A	-800 V
DCBun	-30.9 V	-30.9 V
DefLens	N/A	-2040 V
BunLens	N/A	-3500 V
PD-Tube	N/A	-2040 V
EL6	N/A	-3500 V
MTOF-DT	N/A	-2040 V
MI2&M2	N/A	-2040 V

N_{laps}	MI1&ME1	MI3&ME3	MI7&ME7
0	-5000 V	N/A	N/A
1	-4000 V	-1000 V	600 V
2	-4000 V	-1150 V	600 V
4	-5000 V	-1300 V	600 V
6	-5000 V	-1305 V	600 V
8	-5000 V	-1320 V	600 V
10	-5000 V	-1325 V	600 V
15	-5000 V	-1350 V	600 V
20	-5000 V	-1370 V	600 V
30	-5000 V	-1370 V	600 V
40	-5000 V	-1380 V	600 V
50	-5000 V	-1380 V	600 V
60	-5000 V	-1380 V	600 V
80	-5000 V	-1380 V	600 V
100	-5000 V	-1380 V	600 V
120	-5000 V	-1380 V	600 V
140	-5000 V	-1380 V	600 V
180	-5000 V	-1380 V	600 V

The beam cooler and buncher's ejection voltages for both the low and high emittance scenarios are also shown in Tables 7.1 and 7.2. These voltages were determined based on simulations described in Chapter 6. The transportation lenses' voltages for each scenario were adjusted to achieve a transmission efficiency to the MTOF as close to 100% as possible. In the high emittance case, 2 of 990 ions hit an electrode directly before the MTOF; in the low emittance case no ions were lost. During the ejection process the effects of a residual gas pressure in the transport region following the beam cooler and buncher were ignored. This gas pressure would slightly reduce the

Table 7.2: Left: Voltages applied to the beam cooler and buncher, transportation lenses, and MTOF for cooling and ejection of an ion distribution with a a longitudinal emittance of 0.8 π eV·μs, and a transverse emittance of 5.8 π mm·mrad. Right: Voltages applied to the MTOF's electrode depending on the number of laps N_{laps}.

Electrode	Trapping	Ejection
RF Amp.	55 V	55 V
StartBun	-22.5 V	-27.5 V
Trap1	-23 V	30 V
Trap2	-24 V	110 V
Trap3	-25 V	110 V
Trap4	-38.5 V	400 V
Trap5	-39 V	-50 V
Trap6	-38.5 V	-400 V
Trap7	-25 V	-400 V
BunEx1	-8 V	-400 V
BunEx2	N/A	-600 V
TranTube	N/A	-1200 V
DCBun	-30.9 V	-30.9 V
DefLens	N/A	-2040 V
BunLens	N/A	-3100 V
EL6	N/A	-3300 V
MTOF-DT	N/A	-2040 V
MI2&M2	N/A	-2040 V

N_{laps}	MI1&M1	MI3&M3	MI7&ME7
0	-6000 V	N/A	N/A
1	-5000 V	-1200 V	600 V
2	-5000 V	-1300 V	600 V
4	-5000 V	-1350 V	600 V
6	-5250 V	-1400 V	600 V
8	-6150 V	-1475 V	600 V
10	-6150 V	-1475 V	600 V
15	-6150 V	-1475 V	600 V
20	-6150 V	-1475 V	600 V
30	-6150 V	-1475 V	600 V
40	-6150 V	-1475 V	600 V
50	-6150 V	-1475 V	600 V
60	-6150 V	-1475 V	600 V
80	-6150 V	-1475 V	600 V
100	-6150 V	-1475 V	600 V
120	-6150 V	-1475 V	600 V
140	-6150 V	-1475 V	600 V
180	-6150 V	-1475 V	600 V

transmission efficiency of ions through this region and result in a time and energy straggling. However, the higher emittance case should account for this simplification.

Ions were injected into the MTOF by setting the injection mirror's voltages MI2-MI7 at a transport potential (-2040 V) while the injection mirror's lens MI1 and all the ejection mirror's electrodes ME1-ME7 were at their operational voltages. Once the ions reached the mid-point of the MTOF on their 1st lap the voltages on the MI2-MI7 ring electrodes were raised to their operational voltages. When the ion packet reached MTOF's mid-point on its Nth lap it was released from the MTOF by lowering the ejection mirror's voltages ME2-ME7 to a transportation potential (-2040 V). Otherwise, for the duration of the ion packets confinement in the MTOF, the mirrors were operated symmetrically with a dual deceleration electric field. The voltages of the MI4-MI6/ME4-ME6 ring electrodes were chosen to achieve a linear increase in

potential between the MI3/ME3 and MI7/ME7 ring electrodes, respectively. The voltages on MI3/ME3 and MI7/ME7 ring electrodes were then adjusted to achieve a minimum pulse width at BOB5 (see Figure 2.2) for a given number of laps (N_{laps}). Due to the length of time (several hours to days) required to perform a single SIMION simulation for $N_{laps} > 40$ the MTOF's operational parameters were investigated but not optimized beyond this point. Asymmetric and non-linear solutions were not considered to limit the initial parameter space. However, such solutions are possible and one is used ORNL; their MTOF is operated in an asymmetric configuration containing a "short" mirror and "long" mirror.

For the simulations performed at ORNL a detailed explanation is provided in Appendix C. The MTOF geometry shown in Figure 7.3 was used but a simplified version of the LEBIT beam cooler and buncher was required as their simulations couldn't accommodate an RF electric field or non-cylindrical electrodes. In these simulations, the MTOF was placed directly after the EL6 lens shown in Figure 6.4 as they were not concerned about spatial constraints. Despite these deviations, valuable information can be gained from the ORNL simulations. Their ray tracing and optimization programs are much faster than the SIMION calculations performed in this work, and a much larger number of laps ($N_{laps} \approx 1000$) and parameter space could be investigated.

Results

The SIMION MTOF simulations were run for a range of laps $0 \leq N_{laps} \leq 180$ for both the low and high emittance scenarios. In all cases, ions were transmitted through the MTOF with a 100% efficiency. The MTOF electrode voltages used for a given number of laps (N_{laps}) are presented in Tables 7.1 and 7.2 for the low and high emittance ion distributions respectively. The mass resolution obtained at BOB5 as a function of the number of laps is shown in Figure 7.4. In both cases, a mass resolution of R $\approx$ 10,000 is achieved after 60 laps and a transportation time of about 800 μs.
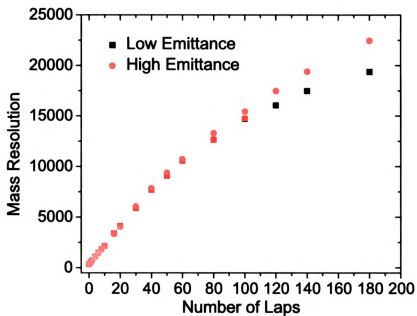
Figure 7.4: Mass resolution obtained for an ion pulse transmitted through the MTOF for a given number of laps.
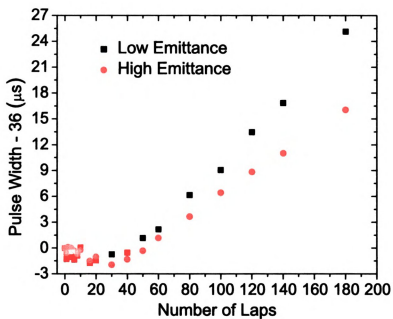
Figure 7.5: The change in an ion pulse's width from its original value after performing a given number of laps in the MTOF.

Surprisingly, a higher mass resolution was obtained for the high emittance case, as compared to the low emittance one, at $N_{laps} > 60$. This is most likely an artifact due the lack of optimization performed for $N_{laps} > 40$. The change in the pulse width from its original width as a function of the number of laps is shown in Figure 7.5. For $N_{laps} < 40$ the change is kept below zero, but it rise quickly afterwards, again due to a lack of optimization. The ORNL MTOF simulations which were performed and optimized for a much larger number of laps $(0 < N_{laps} < 960)$ show that a mass resolution of R > 50,000 is possible with this MTOF design (see Figures C.1 and C.2).

Two other output parameters of the SIMION simulations to consider are the final longitudinal and transverse emittance. The results are shown in Figures 7.6 and 7.7 respectively. The longitudinal emittance increases by less than 20%, for both the low and high emittance cases, after 60 laps in the MTOF. This is expected as the ions pulse's width and longitudinal emittance are directly related. However, the transverse
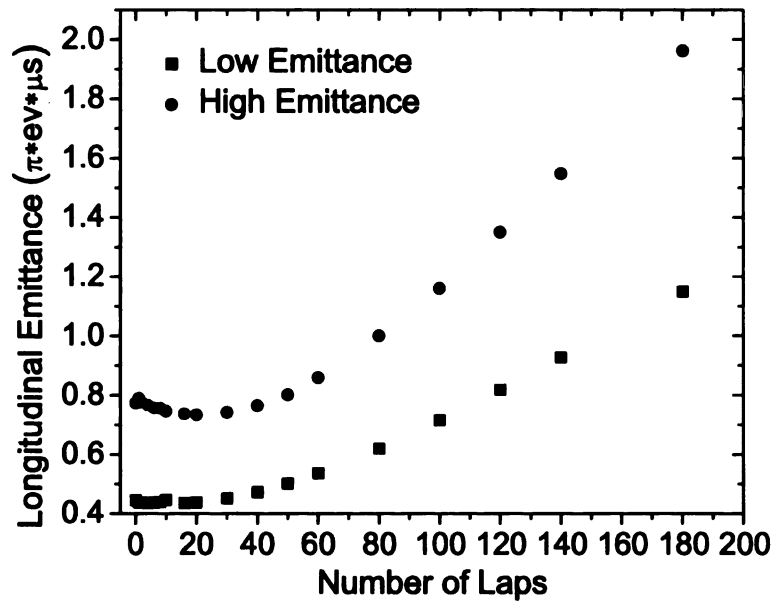
Figure 7.6: Longitudinal emittance obtained for an ion pulse transmitted through the MTOF for a given number of laps.
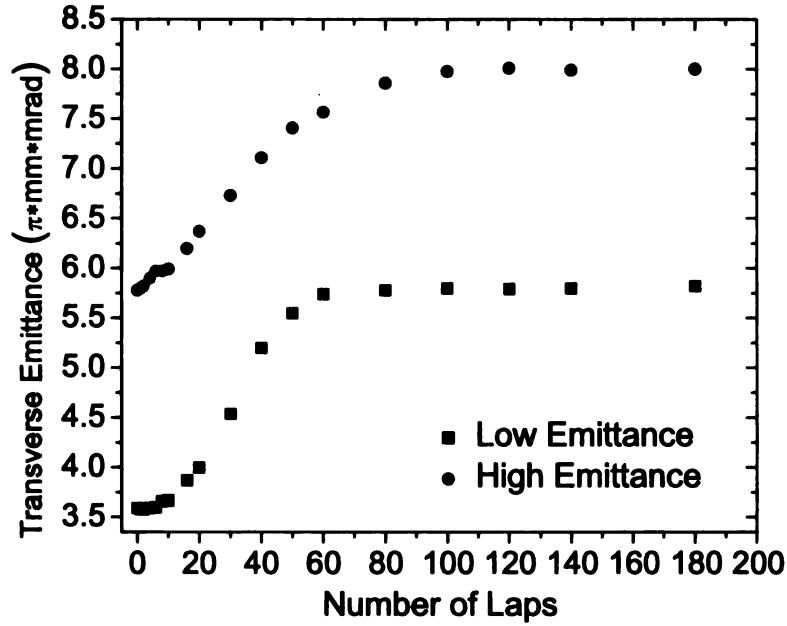
Figure 7.7: Transverse emittance obtained for an ion pulse transmitted through the MTOF for a given number of laps.

emittance, which wasn't an optimization parameter, after 60 laps was increased by 60% and 25% for the low and high emittance cases respectively. This was due to an effective growth of the phase space ellipse in which it became slightly triangular in shape.

To achieve a minimal longitudinal and transverse emittance increase, the MTOF's transportation optics were further investigated. The most effective method found to accomplish this goal was to raise the MTOF's transportation voltage. This both creates a stronger spatial focus for ions entering the MTOF and reduces the voltage difference on the MTOF's electrodes that must be switched. The transverse emittance as a function of the transportation voltage for the low emittance ions distribution and $N_{laps} = 60$ is shown in Figure 7.8. At a transportation voltage of -1200 V, the transverse emittance is reduced from 5.8 π mm·mrad to 4.2 π mm·mrad. With this setting the same mass resolution and longitudinal emittance shown in Figures 7.4 and 7.6 were achieved, but with a gain in the transverse emittance of less then 20% from

the originally stated value (3.6 π mm·mrad). These settings also reduce the maximum voltage difference to be switched from 2600 V to 1800 V which is technically easier to accomplish. Another way to counter the gain in longitudinal and transverse emittance is sending ions back into the beam cooler and buncher for further cooling. Preliminary simulations show that after 60 laps in the MTOF, ions can be transported back to beam cooler and buncher and recaptured with an efficiency greater then 90% using the same transportation lenses voltages listed in Table 7.1.
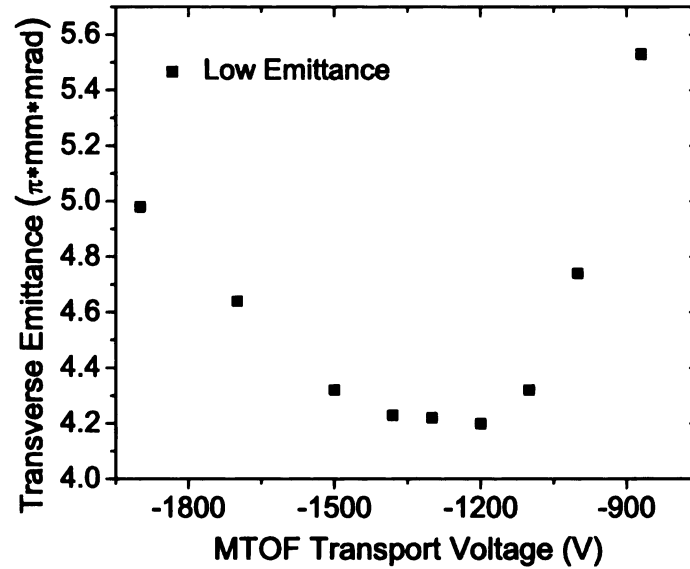
Figure 7.8: Transverse emittance obtained for an ion pulse transmitted through the MTOF ($N_{laps} = 60$) for a given transportation or base MTOF voltage.

Limitations

External factors can limit the achievable transmission efficiency and mass resolving power of the MTOF. These factors can include mechanical deviation from design specifications, ion/neutral-atom collisions in the MTOF, thermal expansion of the electrodes, instability or drift of a power supply's voltage, and mechanical misalignment of the MTOF's electrodes. To determine an acceptable parameter range for these

iacto

macl

in Ta

I

the

<

and

wei

SIN

6.

eff

a

m

Fi
th
w

factors, simulations were performed for a variety of different scenarios. For these simulations the low emittance ion distribution with $N_{laps} = 60$ and the voltages given in Table 7.1 were used.

The first limiting factor explored was the effects of neutral gas atoms present in the MTOF. In the beamline between BOB4 and BOB5 a small residual gas pressure ($< 10^{-6}$ mbar) is present due the buffer gas used to cool ions in the beam cooler and buncher. To determine an acceptable range for this pressure, MTOF simulations were run for an increasingly higher helium gas pressures in the MTOF with the same SIMION model used to cool the ions in the beam cooler and buncher (see Section 6.2.1). From these simulations it was determined that the residual gas pressure's main effect would be on the MTOF's transmission efficiency. Most ions that collide with a neutral atom in the MTOF are lost after several laps; thus, they cannot affect the mass resolution or emittance of the final transmitted ion pulse. The result of these
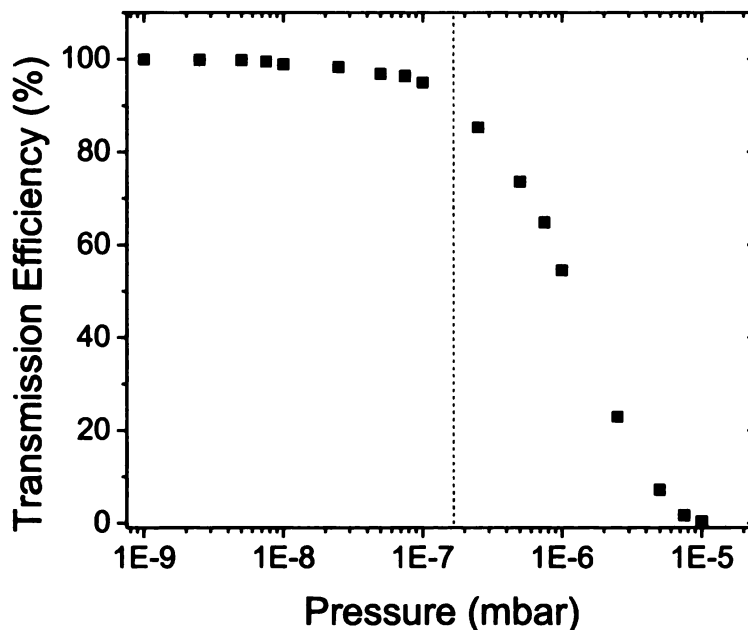
Figure 7.9: Transmission efficiency through the MTOF ($N_{laps} = 60$) as a function of the helium gas pressure in the MTOF. The dashed line represents the pressure below which a transmission efficiency greater 90% is obtained.

simulations are shown in Figure 7.9. In order to achieve a transmission efficiency greater than 90% the residual gas pressure in beamline between BOB4 and BOB5 must be kept below $2 \cdot 10^{-7}$ mbar.

The next group of limiting factors explored were the effects of a voltage instability and temperature change on the MTOF's operation. If the MTOF's mass filter mechanism, such a pulsed deflector, is set to transport an ion pulse with a given mean time of flight, this value must stay constant in time, or else after several hours the ions of interest may no longer be transported. Two factors which can have a large impact on an ion pulse's mean time of flight through the MTOF are the distance between the two mirrors, and the voltage on the last electrode of each mirror. The distance between the two mirrors could change due to a thermal expansion or contraction of the MTOF. Figure 7.10 shows the mean time of flight of ion pulse transmitted through the MTOF for a given deviation in the MTOF length's from its original value (783 mm). To keep the change in the ion pulse's mean time of flight below 25% of its FWHM (38 μs) the deviation in the MTOF's length must be less then $\Delta L = \pm 7.5$
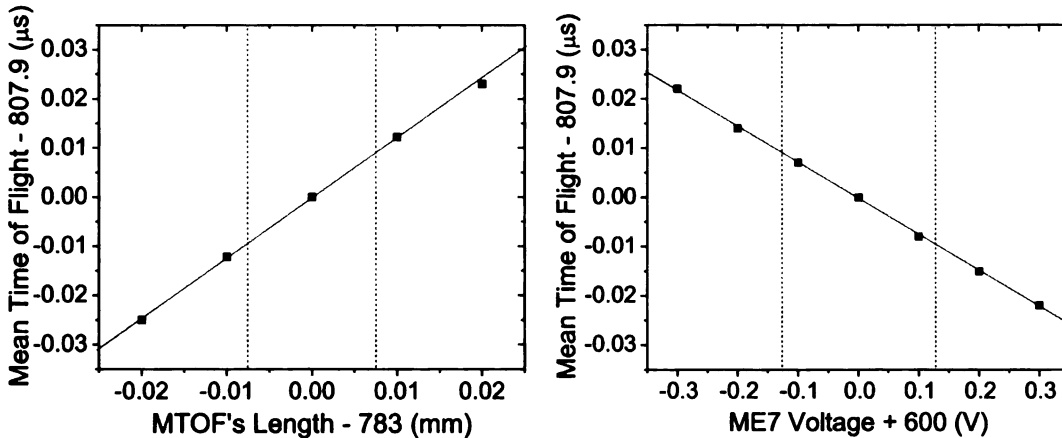
Figure 7.10: Mean time of flight of an ion pulse transmitted through the MTOF ($N_{laps} = 60$) as a function of the MTOF's length (left) and of the voltage of the ejection mirror's last electrode ME7 (right). The band given by the dashed lines represents a change in the mean time of flight less then 25% of the ion pulse's width (FWHM).

μm. A

15 · 1

MTO

order

mirro

7.10

S67

the

in 2

130

th.

cir

th

ro

th

d.

an

T

se

wi

di

th

un

wi

pr

μm. A typical coefficient of linear thermal expansion for a metal at 296° K is around $15 \cdot 10^{-6}$/K and the distance between the two mirror is 783 mm, thus to keep the MTOF's length within the desired range a temperature stabilization of MTOF on the order of $\Delta T = \pm 0.6°$ K would be required. The voltage on the last electrode of each mirror could change due to a "noisy" or temperature-dependent power supply. Figure 7.10 shows the change in an ion pulse's mean time of flight from its original value (807.9 μs) obtained as a function of a deviation in the ME7 electrode's voltage from the value given in Table 7.1 (600 V). To keep the ion pulse's mean time of flight with in 25% its FWHM (38 μs) would require a power supply with a voltage drift less than 130 mV for a reasonable length of time and range of temperatures. It should be noted that these voltage and temperature stabilization requirements could be extended or circumvented with a carefully calibrated PID loop.

The last limiting factor explored was the effect of a mechanical misalignment on the MTOF's operation. It was assumed that the misalignment of the individual mirror's electrode could be avoided and that the largest issue would be the alignment of the two mirrors with respect to each other. The two misalignments considered were a displacement of the ejection mirror perpendicular to the beamline's axis (Transverse) and a non-zero angle between the ejection mirror and the beamline's axis (Angular). The effects of these perturbations on an ion pulse's transverse emittance, the most sensitive parameter, are shown in Figure 7.11. To maintain a transverse emittance within 25% of the previously quoted value (5.8 π mm·mrad) a transverse and angular displacement of less then 1.2 mm and 1.3 mrad respectively would be required. For the most part, these problems could be avoided by constructing the MTOF as one full unit as opposed to two separate mirrors. The alignment of the MTOF's optical axis with the rest of the beamline could be corrected using the deflector system already present in the LEBIT beamline.

Fig
(N
rig
tra
bea

7.

W

re

fo

tra

co

tu

the

of

sol

sin
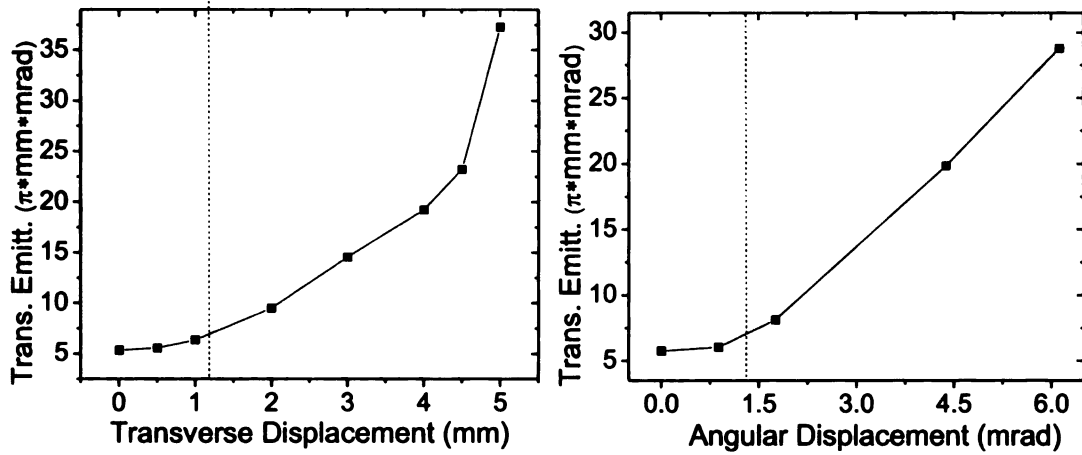
Figure 7.11: Transverse emittance of an ion pulse transmitted through the MTOF (N_{laps} = 60) as a function of the ejection mirror's transverse (left) and angular (right) displacement from the beamline's optical axis. The dashed lines represents a transverse emittance 25% greater then value obtained with the ejection mirror's and beamline's optical axis aligned.

7.3   Conclusion

With the SIMION simulations, of the MTOF design presented in this work, a mass resolution of R > 10,000 with a transmission efficiency of 100% was demonstrated for N_{laps} = 60. It was also shown, for the same settings, that an ion pulse's gain in transverse and longitudinal emittance could be kept below 20%. In preparation for the construction of such a device, performance reducing factor such as temperature fluctuations and residual gas from the cooler and buncher were considered. Fortunately, the tolerance determined pose no technical challenge to the successfully realization of the MTOF. Moreover, the ORNL simulations indicate that higher high mass resolving powers (R > 50,000) are possible with this design. Nonetheless, the SIMION simulations demonstrates the advantage of using an MTOF at the LEBIT facility.

Ch

Su

In
pr
al
p
n
al
w

fr
T
pr
of
of

as
gr
lat
wi

Chapter 8

Summary and Outlook

In this thesis, the first high precision mass measurement of ^{70m}Br was successfully performed in the LEBIT Penning trap. The masses of ^{68}Se, ^{70}Se, and ^{71}Br were also measured and their precisions were increased by factors of 40 and more over the previous literature values [2]. The highest precision achieved was for the waiting point nucleus ^{68}Se, with a $\frac{\delta m}{m} = 8 \cdot 10^{-9}$. With the improved mass values for ^{70}Se and ^{71}Br along with Coulomb displacement energies from [1] higher accuracy mass prediction were made for the proton-rich mirror nuclei ^{70}Kr and ^{71}Kr.

The improved mass values obtained in this work have far reaching implications from stellar evolution to our understanding of nuclear structure far from stability. Through our measurements we were able to more accurately calculate the neutron-proton pairing energy for ^{70}Br. This value in combination with mass measurements of heavier N $\approx$ Z nuclei will help to prove or disprove the claim for a re-strengthening of this pairing energy [73].

These measurements also further solidified the importance of ^{68}Se in the rp-process as a waiting point. Through a local network calculation, we found ^{68}Se to have a greater effective lifetime then previously thought. In a more extensive network calculation we demonstrated that our measurements have greatly reduced the uncertainty with which the light curve of a type I x ray burst can be simulated; thus allowing a

M

ret t

Br

impr

I

impl

cycl

hea

ele

the

an

ti

T

fi

is

te

o

more accurate comparison to observed type I x ray bursts.

Most recently we have remeasured the mass of ^{66}As to the precision required to test the Conserved Vector Current hypothesis [91]. In the future, we hope to remeasure ^{70}Br for the same reason and to measure the mass of ^{65}As for the first time to further improve the accuracy of simulated type I x ray bursts.

In addition to this part of the work several upgrades to the LEBIT facility were implemented. To improve the ion detection efficiency for the measurement of an ion's cyclotron frequency, a Daly detector was simulated and then installed in the LEBIT beamline. This realized system has been in use for over two years and secondary-electron yield measurements suggest that it provides a detection efficiency greater then 90%. To enhance the LEBIT facility's non-isobaric contaminant ion suppression and detection capabilities the beam cooler and buncher's time of flight system was optimized using standard techniques from the field of time-of-flight mass spectrometry. Through this process the resolving power of the beam cooler and buncher's time-of-flight system was increased by a factor of 2.5. Furthermore, to suppress molecular isobaric contaminant ions the addition of a multipass time-of-flight mass spectrometer to the LEBIT beamline was simulated. Through these simulations the feasibility of obtaining a resolving power of R > 10,000 with such a system was demonstrated.

Ap

In

C

T
io
o
b
ti
c
b
b
p
c
re
ej
ju
of
an
A

Appendix A

Improvements to the LEBIT

Control System

The LEBIT control system allows users to remotely control parameters necessary for ion manipulation and data collection at the LEBIT facility. In order to provide and optimize the voltages necessary for the operation of the gas cell, beam cooler and buncher, Penning trap, and electrostatic beam transport system connecting them, the ability to control and monitor approximately 400 power supplies is required. To confine ions in the beam cooler and buncher and in the ion guides, RF voltages must be generated, stabilized, and monitored. The high vacuum obtained in the LEBIT beamline requires the control and monitoring of 12 turbo pumps and 20 electro-pneumatic values. The ability to perform a successful experiment requires a precise control of the ejection, capture, and excitation timings through the system. In the resonance detection technique used at the LEBIT facility, the time-of-flight of ions ejected from the Penning trap must be measured, processed, and recorded. These are just a few of the vital task that must be fulfilled by the LEBIT control system. As part of this work the LEBIT control system was upgraded to provide an improved stability and supportability. This chapter will provide a basic overview of these changes and Appendix B explains the operation of this upgraded system.

A.1 Basics
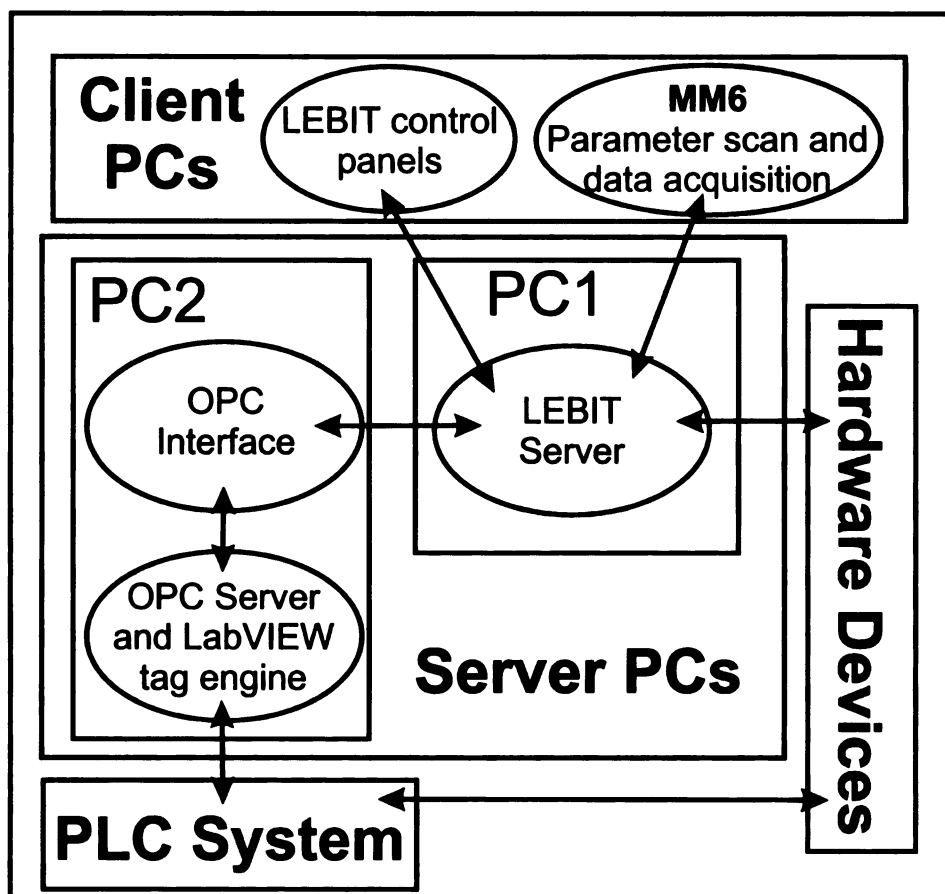
Figure A.1: A flowchart outlining the basics of the updated LEBIT control system.

A schematic view of the upgrade LEBIT control system can be seen in Figure A.1. The LEBIT control system implements two different types of user interfaces for data acquisition and parameter control, respectively. The LEBIT control panels are used to monitor and update parameters in the LEBIT beamline and a program called Mass Measure 6.0 (MM6) is used for data acquisition and parameter scans. The LEBIT control panels and MM6 communicate with the necessary hardware through a LabVIEW based server. The hardware used at LEBIT can be divided into two basic categories, devices controlled directly by the LEBIT server and those controlled by the LEBIT server through the Programable Logic Controller (PLC) system. The PLC

system provides the digital-to-analog and analog-to-digital conversions necessary for control and monitoring of the power supplies, turbo pumps and gate valves that make up the LEBIT beamline. As seen in Figure A.1, the LEBIT server accesses the PLC system through the Object Linking and Embedding for Process Control (OPC) server and the LabVIEW tag engine. A more detailed description of the LEBIT control system can be found in [51] and in the control system's user manual (Appendix B).

A.2 Improvements

For the LEBIT control system to be maintainable it must use supported software. To achieve this an upgrade to the system underlying framework was required. The LEBIT control system is based on a framework designed and supported by the Experiment Control System group at GSI, this framework will be refereed to as the GSI CS. The GSI CS was designed to work in a LabVIEW environment on a Windows or Linux operating system. To prepare for the decommissioning of LabVIEW 6.0 by National Instruments and to incorporate an improved communication layer the GSI framework was recently upgrade from CS2.0 to CS3.1. This upgraded framework and new communication layer were implemented into the LEBIT control system along with several design changes for an improved performance and stability.

A.2.1 DIM Communication

In the previous version of the LEBIT control system all communication was done directly through LabVIEW. In the new version of the control system communication goes through a Distributed Information Management (DIM) server. The DIM system provides a transparent communication layer for distributed environments. The communication protocol, used by DIM, is based on a subscription to "services." For example, a DIM server publishes data to a service and a client can then subscribe to that "services". The DIM system was developed at CERN to control large exper-
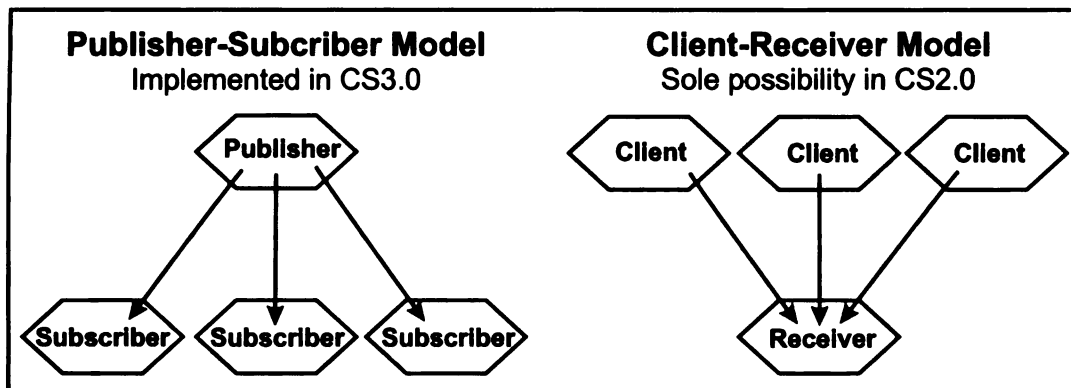
Figure A.2: A schematic comparison of a publisher-subscriber based communication and a client-receiver based communication.

iments with many variables and users. On the other hand, the previous LabVIEW based communication scheme was designed for smaller systems. For instance, LabVIEW can handle a 1,000 process variables but requires 3-4 minutes to allocate the necessary memory whereas DIM can create 10,000 process variables in 4 seconds.

The new GSI CS offers another advantage as a new communication method was added. In the previous version of the GSI CS the sole form of communication was a client-receiver model. In this type of communication commands are sent directly from a client to a receiver. This restricts communication to a one-on-one basis. The publisher-subscriber communication protocol, used by DIM, gives the new GSI CS several advantages over its predecessors. In the new communication scheme, the client receives a notification when a "services" has been updated. Thus removing the need for clients to constantly poll variables for updates and reducing the overhead on the client. This type of communication allows a single publisher to easily distribute information to multiple clients at the same time. A pictorial representation of these two differing communication types can be seen in Figure A.2.

A.2.2 Design Changes

The general infrastructure of the LEBIT control system was changed to improve the stability and maintainability of the system. A comparison of the old and new systems
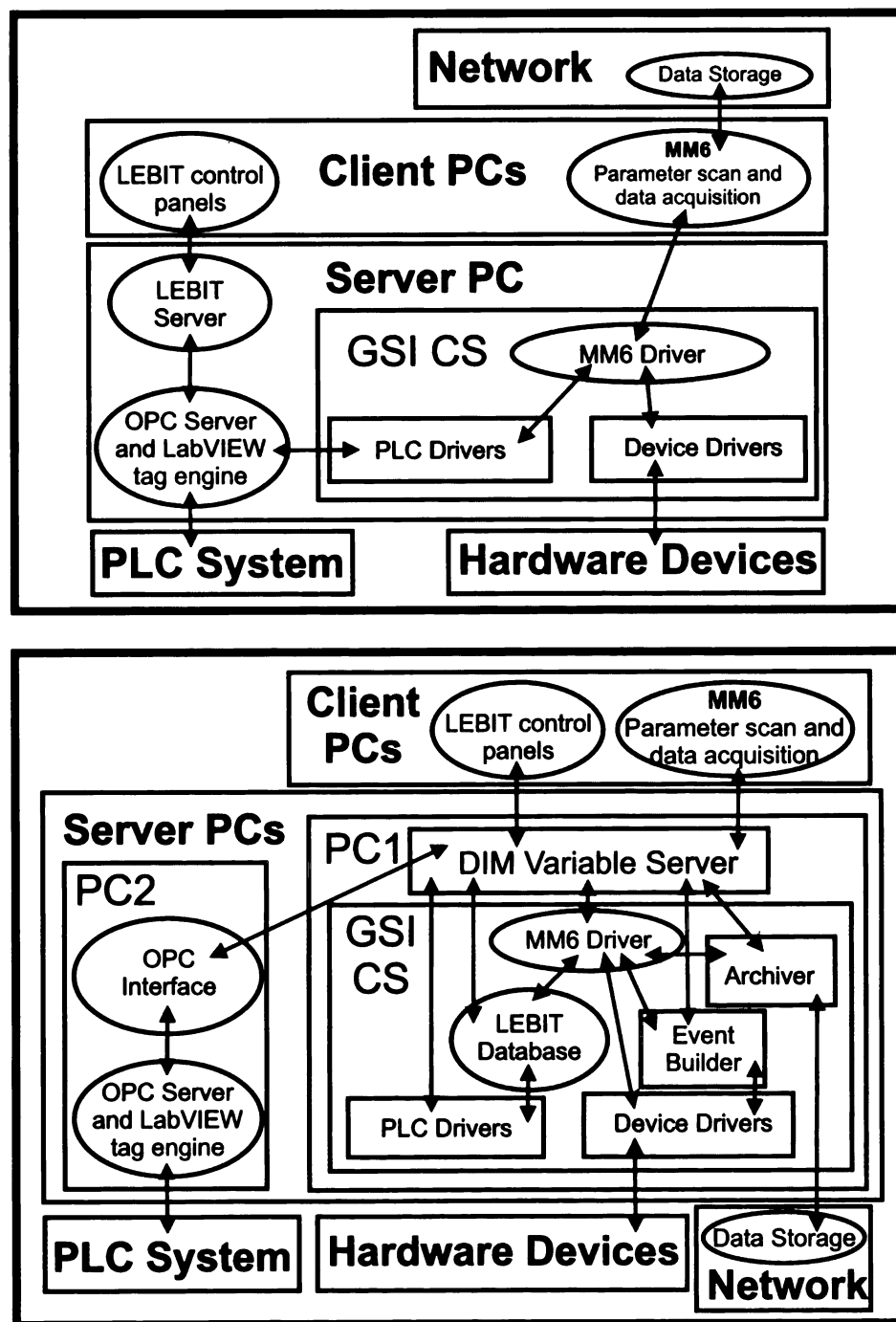
Figure A.3: A flowchart comparison of the old LEBIT control system (top) and the new LEBIT control system (bottom).

can be seen in Figure A.3. In the new system the LEBIT server was integrated into the GSI CS server. Thus removing the need for duplicate coding and consolidating all information into one server. Another infrastructure change was made to the data storage procedure. In the previous LEBIT control system, Figure A.3, the data acquired during a measurement was stored by MM6. This means that if the communication between the client and server computer times out or MM6 crashes the measurement is stopped. With the new changes the data acquired during a measurement is stored by an Archiver on the GSI CS. The new infrastructure has the advantage of being to operate without a connection to MM6. This means even if MM6 crashes the system will continue taking and recording data until MM6 is used to specifically stop the cycle.

Appendix B

Manual for Operating the LEBIT Control System

B.1 Starting the Control System

B.1.1 Start the DIM Name Server

On the **lebit-balcony** pc run DNS.exe through the shortcut folder or at

C:\lebicon\dim\bin\dns.exe

B.1.2 Start the Domain Management System Server

1. On the **lebit-balcony** pc run DMSServer.exe through the shortcut folder or at

    C:\lebicon\cs\binaries\DomainManagementSystem\DMSServer.exe

    (a) If the shortcut is used the correct setting file will automatically load

    (b) If the shortcut is not used, the setting file DMS__Server.xml must be loaded

2. Click the UPDATE DOMAIN button

B.1.3 Start the Domain Management System Client

1. On the **lebit-balcony** and **lebit-3** pc run DMSClient.exe through the shortcut folder or at C:\lebicon\cs\binaries\DomainManagementSystem\DMSClient.exe

   (a) If the shortcut is used it will automatically set the domain and node name

   (b) If the shortcut is not used, set the domain name to "KSTest" and the node of the DMS Server to "lebit-balcony"

2. Click the Set button

3. On the **lebit-balcony** pc the client will load NodeMon.exe and CSSQLServer.exe

4. On the **lebit-3** pc the client will load NodeMon.exe and CS_DSC.exe (the OPC-Interface)

5. Wait until all executables are finished loading

B.1.4 Start the LEBIT Server

1. On the **lebit-balcony** pc run CS_LEBIT.exe through the shortcut folder or at C:\lebicon\cs\binaries\CS\CS_LEBIT.exe

   (a) If the shortcut is used it will automatically set all variables

   (b) If the shortcut is not used

      i. Set the Data Source to "Process"

      ii. Leave the sqlServerNode blank (if empty it will use the local node)

      iii. Set the systemID to "TestSystem"

      iv. Set the domainName to "KSTest"

2. Click the Set button

B.2   Troubleshooting the Server

1. Check for any error messages on the **lebit-balcony** and **lebit-3** pcs

2. Check to make sure the light on the LEBIT server front panel turns green

3. If the light is red or any other problems occurs here are a couple of diagnostic tools

    (a) Click the Inspector button on the LEBIT server to view the state of a driver

        i. In the Inspector panel use the drop down menu select to "event error" or "periodic error"

    (b) To check the connection between the **lebit-balcony** and **lebit-3** pc load DMSViewer.exe through the shortcut folder or at

        C:\lebicon\cs\binaries\DomainManagementSystem\DMSClient.exe

    (c) Load DID.exe through the shortcut folder or at

        C:\lebicon\dim\bin\DID.exe to determine the state of a DIM variable

B.3   Log File Information

B.3.1   The Server

1. Two new log files are created every time the server is restarted

2. One log file records all analog (voltage related) set value changes and the other records all digital (vacuum related) set value changes

3. The voltage related log files are located at C:\lebicon\Logs\PLC on the **lebit-balcony** pc

4. The vacuum related log files are located at C:\lebicon\Logs\Vacuum on the **lebit-balcony** pc

B.3.2 Logging the Target Monitor

1. On the **lebit-balcony** pc run the Target Monitor.vi through the shortcut folder or at C:\lebicon\Control\TGMON\Target Monitor.vi

2. This program will only log the target monitor, the update interval can be changed using the scan interval box

3. Log files are located at C:\lebicon\Logs\Target Monitor

B.3.3 Logging Set and Monitor Values

1. On the **lebit-3** pc run the Signal Monitor6a.vi through the shortcut folder or at C:\lebicon\Control\Signal Monitor\Signal Monitor6a.vi

2. This program can log any set value or monitor value controlled by the LEBIT server

    (a) Enter the nicknames of the set value or monitor value to be logged in the PLC signal names array

3. Using this program the Magnet Pressure can also be logged

    (a) Enter "Magnet Pressure" into the special signal names array

4. Log files are located at C:\lebicon\logFiles\Signal Monitor

B.4 Starting the Magnet Pressure Regulation

1. To regulate the pressure in the superconducting magnet the pressure must be read from the Setra (the digital pressure gauge) and entered into the PID controller feedback loop

2. On the **lebit-3** pc run the acquireSetra.vi located in the shortcut folder or at C:\lebicon\Control\Setra\acquireSetra.vi

3. See section B.8.3 for more details on PID Loops

B.5   Starting the Data Dumper

1. The Data Dumper will log all monitor values at a given time interval

2. On the **lebit-3** pc run the DataDump.vi through the shortcut folder or at C:\lebicon\Control\DataDump\DataDump.vi

3. Set the Update Period (the default time is 60 s) to the desired update interval and press the RUN button

4. The logs file are located at C:\lebicon\logFiles\DataDump

B.6   Starting the Magnet Field Decay Compensator

1. The magnet field decay compensator counteracts the natural decay in the magnetic field by running current through a wire wrapped around the magnets bore tube

2. Turn ON the blue power supply labeled the "Magnet Field Decay Compensator"

3. Set the gray box below the LN2 level display to "PLC"

4. Set the gray box next to BOB6 to "MAG"

5. On the **lebit-3** pc run the MagnetComp.vi through the shortcut folder or at C:\lebicon\Control\UseFullVI's\MagnetComp.vi

B.6.1 Ramping Compensation

1. Set the switch on the program to "Ramping"

2. Set the desired slope and update interval

3. Click the RUN button

4. Note: If you stop the program the power supply will stay at the current voltage

B.6.2 Manual Compensation

1. Set the switch on the program to "Manual"

2. Click the RUN button

3. Set the box labelled "Manual PLC Voltage" to the desired voltage

B.7 Using the Decay Counter

1. The Decay Counter will log all decays (counts) in a given time

2. On the **lebit-balcony** pc run the DecayCounter.vi through the shortcut folder or at C:\lebicon\Control\BETA\DecayCounter.vi

3. Set the drop down menu labeled Counters to the desired channel

4. Enter the desired time range and interval in the "Measurement Time (s)" and "Time Step" box respectively

5. Click the RUN button to start

6. Note: Individual time steps with more counts then the value set in "Discriminator (High)" box will be replaced with the value set in the AveCnts box and the discriminated total will be displayed in the DiscData box

7. Log files are located at C:\lebicon\Logs\DecayCounter

B.8 The Programmable Logic Controller (PLC) System

B.8.1 The LEBIT PLC System

1. Communication with the PLC system goes through the DirectSOFT32 Data Server on the **lebit-3** pc (this is automatically started by the OPCInterface)

2. The DirectSOFT32 Data Server can be accessed through the shortcut folder or through the windows control bar at Start→Program→DirectSOFT32→ DirectSOFT Data Server Tools→DirectSOFT32 Data Server

3. The LEBIT system consists of 4 individual CPUs

   (a) N4Topic - This controls the Gas Cell and IonGuide voltages

   (b) G2Topic - This controls the Penning Trap injection, ejection and trap voltages

   (c) BTopic - This controls the HV1, Buncher and HV2 voltages

      i. BTopic is special in that G1 cpu remotely controls the PLC systems in HV1 and HV2

   (d) VTopic - This controls the relays for the LEBIT Vacuum system

B.8.2 Editing a PLC

1. The control code for a PLC cpu can be viewed and edited using the DirectSOFT32 Program

2. The DirectSOFT32 Program can be accessed through the shortcut folder or through the windows control bar as Start→Program→DirectSOFT32→ DirectSOFT Program Tools→DirectSOFT32 Program

119

3. After starting the DirectSOFT32 Program a PLC project can be opened through file menu as File→Open Project

4. The LEBIT System PLC projects are located at C:\DirectSOFT32\Projects\LEBITProjects

   (a) N4Topic Project Name - N4 PLC Control

   (b) G2Topic Project Name - G2 PLC Control

   (c) BTopic Project Name - HV1&HV2&BUN PLC Control

   (d) VTopic Project Name - LEBITV Vacuum PLC Control

Monitor Voltage Equation

Monitor Value = [(Value to PLC + Offset) * Scale] (see section B.10.2 for more details on how the scale and offset are calculated)

Set Voltage Equation

PLC Output Value = [(Set Value / Scale) - Offset] (see section B.10.2 for more details on how the scale and offset are calculated)

Manual Reading or Writing PLC Variables

1. To write to a PLC variable

   (a) PLC variables can be changed manually through LabVIEW using the Set.vi through the shortcut folder or at C:\lebicon\Control\UseFullVI's\Set.vi

   (b) To change a PLC variable directly use the DirectSOFT32 Program

      i. First open the project of the desired PLC System

      ii. Next open the Data View window (Debug→DataView→New)

      iii. Next enter the name of the desired element in the DataView window

iv. Next set the mode to Read/Write Mode

v. The status will display the current value

vi. The value can be changed using the Edits box and the "Write Current Edits" button

2. To read to a PLC variable

   (a) PLC variables can be read through LabVIEW using the Read.vi through the shortcut folder or at C:\lebicon\Control\UseFullVI's\Read.vi

   (b) A PLC variable can be read directly the using the DirectSOFT32 Program

      i. First open the project of the desired PLC System

      ii. Next open the Data View window (Debug→DataView→New)

      iii. Next enter the name of the desired element

      iv. The status will display the current value

B.8.3 Proportional Integral Derivative (PID) Controller

1. The LEBIT system has 3 PID Controllers

   (a) The Mass Filter Amplitude Controller

      i. Regulates the mass filter amplitude

      ii. The PID loop is located in N4 PLC Control

      iii. The Set Point address is N4-V4002

      iv. The Process Variable address is N4-V4003

      v. The Bias Value address is N4-V4004

      vi. The Output address is N4-V4005

   (b) The Buncher Pressure Controller

      i. Regulates the helium and neon pressure in the cooler

    ii. The PID loop is located in G2 PLC Control

    iii. The Set Point address is G2-V2042

    iv. The Process Variable address is G2-V2043

    v. The Bias Value address is G2-V2044

    vi. The Output address is G2-V2045

(c) The Magnet Pressure Controller

    i. Regulates the pressure in the superconducting magnet

    ii. The PID loop is located in G2 PLC Control

    iii. The Set Point address is G2-V2002

    iv. The Process Variable address is G2-V2003

    v. The Bias Value address is G2-V2004

    vi. The Output address is G2-V2005

2. The PID Loop Freeze

(a) The PID loop freezes when the output of the PID loop has been disconnect the from input of the system for a significant period of time

(b) When the PID loop is disconnected the Integration term (the Bias Value) in the PID loop becomes excessively small or large

(c) Try changing the Bias Value value

(d) Try changing the Set Point value

B.9   The Control System (process) Database

The control system database contains information used by the control system drivers

B.9.1 Accessing the Control System Database

1. The control system database can be accessed using the Control System Database Tools (CSDBTools.exe)

2. CSDBTools.exe can be accessed through the the shortcut folder or at C:\lebicon\cs\binaries\CSDBTools\CSDBTools.exe

    (a) To access the control system database click the "DB and Tag tool" button

    (b) Next click the Connect button to access the "process" database

B.9.2 Editing the Control System Database

1. For example to add an Arbitrary Frequency Generator (AFG) to MRCLEAN

    (a) Access the control system database as described in section B.9.1

    (b) Select the class MrClean

    (c) Select the instance MrClean

    (d) Click the edit instances button

    (e) In the Attribute drop down menu select the Interface to which the AFG will be added (for instance Interface5)

    (f) Click the set values button

    (g) Click the InstanceName

    (h) Enter the name of the AFG instance to be added in the Set Values command line (for example AFG6)

    (i) Click the apply button

    (j) Click the done button

    (k) Click the DONE (write to db) button

B.10 The LEBIT Address Database

The LEBIT address database contains information on the voltages and relays controlled by LEBIT PLC system

B.10.1 Accessing the LEBIT System Address Database

1. The LEBIT system address database addresses.mdb can be accessed through the shortcut folder or at C:\lebicon\dBase\addresses.mdb

2. Click on tblDevices

B.10.2 LEBIT System Address Database Layout

Upper Level

1. Each PLC module has its own header in the database

2. The Description provides information on what each module controls

3. The DeviceTypeID gives the type of PLC module contained in a given slot

   (a) F4-08AD - 8 channel bipolar analog input (12-bit)

   (b) F4-08THM - 8 channel bipolar analog input (16-bit)

   (c) F4-16DA-2 - 16 channel unipolar analog output (12-bit)

   (d) F4-04DA-2 - 4 channel bipolar analog output(12-bit)

   (e) F4-04DAS-2 - 4 channel unipolar analog output(16-bit)

   (f) D4-16NE3 - 16 channel digital input

   (g) D4-16TD2 - 16 channel digital output

   (h) NOPLC - variables not associated with a PLC

4. Using the RackID, Base and Slot one can determine the location of a module

5. The BaseAddress contains the address used to build the PLC address associated with a particular Channel

Lower Level - General

1. Each rung in the lower level of the database associates the Nickname of a variable with the information necessary to address, locate and scale a channel on a PLC module

   (a) A Nickname with a "-M" at the end corresponds to a monitor value

   (b) A Nickname with a "-S" at the end corresponds to a set value

2. PanelDep - Tells which control panel the variable is associated with: bob1tobun, bun, buntopenning, ionguide, n4tobob1, pennningeject, penning, gascell, testionsource, mcp&phosvol, Vacuum, Cleaning&Misc

3. Channel - Tells which channel in the PLC module the variable is associated with

   (a) The Channel plus the BaseAddress gives the PLC address for that particular set or monitor value

Table B.1: A table for the G1B2 module showing how to calculate the PLC addresses for a given Channel and BaseAddress

Channel	BaseAddress	LabVIEW TAG	PLC Topic	Mon or Set PLC Address
1	B-v10160	B-v10160	BTopic	v10160
2	B-v10160	B-v10162	BTopic	v10162
3	B-v10160	B-v10164	BTopic	v10164
4	B-v10160	B-v10166	BTopic	v10166
5	B-v10160	B-v10170	BTopic	v10170
6	B-v10160	B-v10172	BTopic	v10172
7	B-v10160	B-v10174	BTopic	v10174
8	B-v10160	B-v10176	BTopic	v10176

4. Special - Used to describe any feature out of the ordinary associated with the variable

Lower Level - Analog Modules

1. PLClo - Sets the min input or output voltage for that PLC channel

2. PLChi - Sets the max input or output voltage for that PLC channel

3. Using NomScale, NomOffset, CorrScale and CorrOffset the Scale and Offset for a channel can be determined

    (a) Offset = NomOffset - CorrOffset

Table B.2: A table for the G1B2 module showing how to calculate the PLC addresses for the Offset of a given Channel and BaseAddress

Channel	BaseAddress	LabVIEW TAG	PLC Topic	Offset PLC Address
1	B-v10160	B-v11160	BTopic	v11160
2	B-v10160	B-v11162	BTopic	v11162
3	B-v10160	B-v11164	BTopic	v11164
4	B-v10160	B-v11166	BTopic	v11166
5	B-v10160	B-v11170	BTopic	v11170
6	B-v10160	B-v11172	BTopic	v11172
7	B-v10160	B-v11174	BTopic	v11174
8	B-v10160	B-v11176	BTopic	v11176

    (b) Scale = NomScale * CorrScale

Table B.3: A table for the G1B2 module showing how to calculate the PLC addresses for the Scale of a given Channel and BaseAddress

Channel	BaseAddress	LabVIEW TAG	PLC Topic	Scale PLC Address
1	B-v10160	B-v12160	BTopic	v12160
2	B-v10160	B-v12162	BTopic	v12162
3	B-v10160	B-v12164	BTopic	v12164
4	B-v10160	B-v12166	BTopic	v12166
5	B-v10160	B-v12170	BTopic	v12170
6	B-v10160	B-v12172	BTopic	v12172
7	B-v10160	B-v12174	BTopic	v12174
8	B-v10160	B-v12176	BTopic	v12176

(c) see sections B.8.2 and B.8.2 for more details on the Scale and Offset

4. Monitor - Allows the user to duplicate a PLC monitor value

   (a) For instance by setting the Monitor value of HypCorrTubeATrap-M, HypCorrTubeAEj-M and HypCorrTubeAInj-M (which don't have an associated PLC Monitor) to HypCorrTubeA-M the PLC monitor value from HypCorrTubeA-M will be copied to HypCorrTubeATrap-M, HypCorrTubeAEj-M and HypCorrTubeAInj-M

5. Base - Name of the variable which controls the base voltage of the set value

   (a) Set Value to PLC = Set Value + Base

Lower Level - Digital Modules

1. For Monitor Values - VTopic

   (a) A digital Monitor channel where the Special value = Enable means that variable has associated safety requirements, shown in Figure B.1

      i. A digital Monitor of this type has an associated variable which tells if any safety requirement for this channel have been violated

   (b) In general turning a turbo pump on, opening or closing a prevac line, opening or closing a section valve, opening or closing a pump valve have associated safety requirements

Table B.4: A table for the VACC4 module showing how to calculate the Enable Address for a given BaseAddress and Channel

Nickname	Channel	BaseAddress	Special	Enable Address
N4VAC-M	1	V-X360		N/A
TSTFVAin-M	3	V-X360	Enable	C-X364
TSTFVAout-M	4	V-X360	Enable	C-X366
TSTFVBin-M	5	V-X360	Enable	C-X370
TSTFVBout-M	6	V-X360	Enable	C-X372
TSTGVPin-M	7	V-X360		N/A
TSTGVPout-M	8	V-X360		N/A
TSTGVSin-M	9	V-X360	Enable	C-X400
TSTGVSout-M	10	V-X360	Enable	C-X402
TSTTPin-M	11	V-X360		N/A
TSTTPout-M	12	V-X360	Enable	C-X406

2. For Set Values - VTopic

   (a) PLClo - Contains a value that can be used to determine the force relay off
       PLC Address

       i. This must be used to turn off a relay where a safety requirement has
          not been met

   (b) PLChi - Contains a value that can be used to determine the force relay on
       PLC Address

       i. This must be used to turn on a relay where a safety requirement has
          not been met

Table B.5: A table for the VACD2 module showing how to calculate the force relay off PLC address and force relay on PLC address for a given PLClo and PLChi respectively

Channel	PLClo	PLChi	Off PLC Address	On PLC Address
1	1220	1221	c1220	c1221
2	1222	1223	c1222	c1223
3	1224	1225	c1224	c1225
5	1232	1233	c1232	c1233
8	0	0	N/A	N/A
11	0	0	N/A	N/A
14	0	0	N/A	N/A
15	1264	1265	c1264	c1265

Category	Device	State	1	2	3	4	5	6	7	8	9	10	11	12	13	14	15	16	17	18	19	20	21	22	23	24	25	26
Action	GVS	open	1	1	1	1																						
	GVS	close						1																				
	GVP	open								1	1																	
	GVP	close											1															
	FVA	open												1														
	FVA	close														1												
	FVB	open															1											
	FVB	close																	1									
	TP	start																		1								
	TP	stop																				1						
Forced Action	GVS	close																					1	1	1			
	GVP	close																								1		
	FVA	close																									1	
	FVB	close																										1
Condition	AUTO																						1	1	1	1	1	1
Condition	GVS	open						1															1	1	1			
	GVS	closed	1	1	1	1																						
	GVP	open										1																
	GVP	closed								1	1																	
	FVA	open								1				1			1											
	FVA	closed											1															
	FVB	open								1						1												
	FVB	closed													1													
	FVAA	open																										
	FVAA	closed											1															
	FVBB	open																										
	FVBB	closed													1													
	FVAPi	OK								1		1				1												
	FVBPi	OK									1				1													
	Pe	OK	1		1																							
	Pi	OK		1		1		1	1											0								
	Pe+1	OK	1			1																						
	Pi+1	OK		1	1														0									
	TP	RUN								1	1																	
	TP	RUN>5m								1	1																	
	TP	Fail																							1	1	1	1

Figure B.1: Vacuum Safety Requirements

Appendix C

Summary of ORNL MTOF Simulations

MSU MTOF optics optimization (Geometry #1)

Simulations and write-up by V. A. Shchepunov [90]

C.1 Simplifications

Only DC-field of the buncher is calculated. The presence of the RF electrodes is taken into account reducing the DC field of the electrodes Trap1 through Trap6 by factor of 4. Contributions into the field from other electrodes are not reduced (even if electrode Trap7, for example, is partly shielded by RF-electrodes). Such simplification can result in deviations of optimized mirror voltage settings from "true values", since higher order ToF aberrations are sensitive to field details at the initial bunch position (electrodes from Trap4 through BunEx2).

Similarly, optimal settings are sensitive to initial bunch position, which is supposed to be in the exact middle of the electrode Trap5 (Z_{ini}=60 mm).

Evaluation of time spreads and mass resolving powers for large numbers of laps is performed analytically using calculated 5th order transfer maps. Such a map trun-

cation may result in big evaluation errors at larger energy spreads. It does not seem, **however, that** such truncation is essential for energy spreads under consideration **(dKz0/K0** $<$ Z0 $\cdot$ E/K0 $= \pm 0.6 \cdot 9.14/2000 = \pm 0.28\%$).

C.2   Optimization

Voltages of the MTOF mirror electrodes were adjusted to minimize time spread due **to ToF** optical aberrations dT_{aber} at the MCP (or BNG) position $Z_{final} = 2504$ **mm behind** MTOF for a given number of laps Nlaps between mirrors. Mass resolving power M/dM is evaluated as $0.5 \cdot T_{flight}/dT_{total}$ where time spread $dT_{total} = \sqrt{dT_{aber}^2 + \tau^2}$ and turn-around time $\tau[ns] = 288 \cdot \sqrt{dKz0[eV] \cdot A[amu]}/E[V/mm]$, dT_{aberr} calculated by the optimizing program.

As a preliminary step, voltages of the buncher extraction electrodes Trap5, Trap7, BunEx1, BunEx2 were adjusted at constant other settings (see column "Initial" in Table C.1) to minimize dT_{aber} for Nlaps $= 59$, $T_{flight} \approx 804$ μsec, A $= 39$ amu. After that, settings found for Trap5, Trap7, BunEx1, BunEx2 were fixed, and voltages of the mirror electrodes MI2&ME2 through MI5&ME5 were used in all subsequent optimizations for Nlaps $= 59$, 120, 240, 480, 720 and 960. Settings for the Trap5, Trap7, BunEx1, BunEx2 (column "Optimized" in Table C.1) correspond to extraction field E $= 9.14$ V/mm.

During optimization, initial ion cloud size was dX0 $=$ dY0 $=$ dZ0 $= \pm 0.60$ mm and energy spread dKx0 $=$ dKy0 $=$ dKz0 $= 0.050$ eV (see Table 1). Estimated dT_{aber} and M/dM are presented in Tables C.2 and C.3. Optimal voltage settings are given in Table C.4.

dT_{aber} and M/dM were also evaluated for larger ion cloud size dX0 $=$ dY0 $=$ dZ0 $= \pm 0.80$ mm at fixed optimal voltages (without re-optimization). Similarly, without re-optimization, dT_{aber} and M/dM were evaluated at smaller extraction field E $= 7.26$ V/mm for both dX0 $=$ dY0 $=$ dZ0 $= \pm 0.60$ and $= \pm 0.80$ mm.

C.3   Results

Results of calculations are presented in Tables C.1, C.2, C.3, and C.4 and in Figures C.1 and C.2. Main results, namely M/dM and dT_{aber} for dX0 = dY0 = dZ0 = ±0.60 mm and E = 9.14V/mm, are shown with red solid lines in Figures C.1 and C.2. As one can see, (M/dM) achieves its maximum value of around 76,000 at Nlaps ≈ 720 (T_{flight} = 9455 μs). This saturation is, first of all, caused by ToF chromatic aberrations of odd powers $(t|\delta)$, $(t|\delta^3)$, $t|\delta^5)$, etc (where δ = dKz0/K0 = E · dZ0/K0 = longitudinal energy spread due to longitudinal ion cloud size dZ0).

Dashed lines correspond to extraction at smaller extraction field E = 7.26 V/mm. As on can see, the smaller extraction field provides higher mass resolving powers at large numbers of laps. This is a general dependency for MTOFs.

Blue lines show M/dM and dT_{aber} for larger dX0 = dY0 = dZ0 = ±0.80 mm. This data is presented to demonstrate sensitivity of resolution to the initial ion cloud size. The deterioration of resolution at Nlaps > 480 is caused again by larger chromatic aberrations $(t|\delta)$, $(t|\delta^3)$, $t|\delta^5)$, etc (larger dZ0), as well as by aberrations characterizing dependency of flight time on dX0, dY0 and δ of different power.

In general, the present MTOF system demonstrates relatively small energy acceptance dK/K0 < 0.6-0.8% or around, caused probably by the long injection flight path between the buncher and the mirrors. At the same time, high values of mass resolving power can be achieved for small initial ion cloud size. (Longer cooling in the buncher is desirable before ejection.)

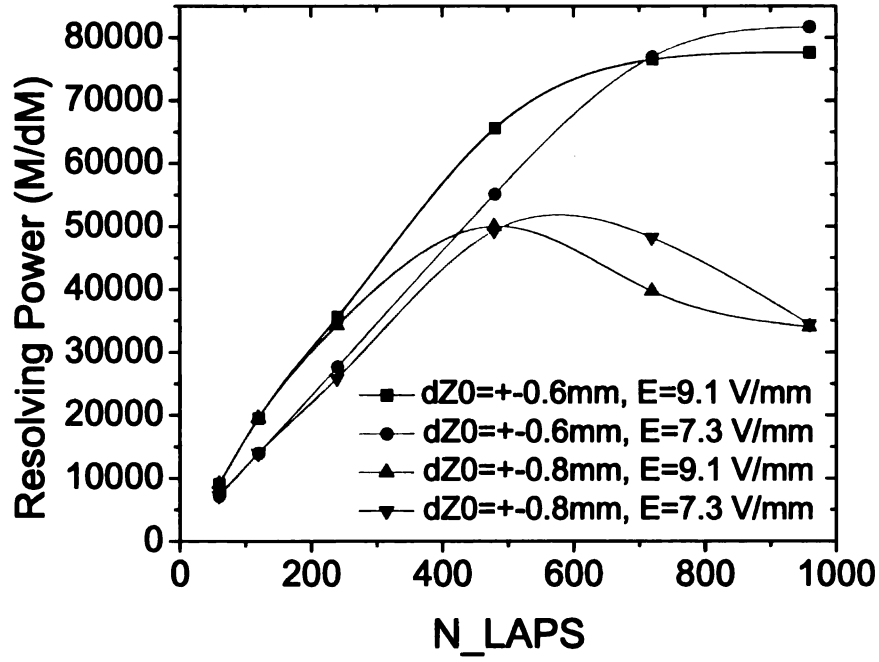Figure C.1: Mass resolving power versus number of laps. Voltage settings are optimized for E = 9.1 V/mm and dZ0 = ±0.60 mm. Other initial beam parameters see in Table C.1.
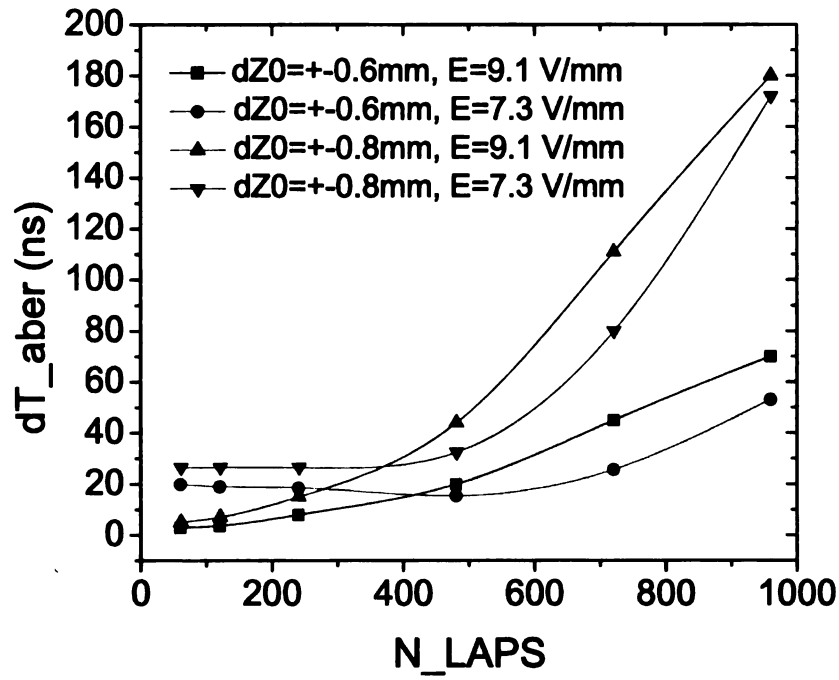

Figure C.2: Time spread caused by ToF aberrations versus number of laps.

Table C.1: Initial beam parameters and optimal voltage settings for Nlaps = 59 and E = 9.14 V/mm.

Parameter	Unit	Value	
Mass	a.m.u.	**39**	
$\Delta x_{ini} = \Delta y_{ini}$	mm	±0.60/±0.80	
Δz_{ini}	mm	±0.60/±0.80	
δK_{ini}	eV	0.050	
Z_{ini}	mm	60.	
Z_{final}	mm	2504.	
E	V/mm	9.14 (7.26)	
τ (turn-around time)	ns	44.0 (55.4)	
Δt_{aberr}	ns	3.07 (19.7)	
T_{flight}	μsec	804.12 (804.24)	
M/dM	1	9115 (6840)	
Tune Q	1	1/3	
		Initial	Optimized
Trap 3		10	10
Trap 4		400	400 (300)
Trap 5		-50	-99.2
Trap 6		-400	-400 (-300)
Trap 7		-200	-284.54
BunEx1		-200	-302.3
BunEx2		-500	-496.3
TransTube		-1300	-1300
BunLens	Volt	-3500	-3500
DriftTube		-2000	-2000
EL6		-3650	-3650
BOB4DEF		-2000	-2000
MI1&ME1		600/-800	600/-800
MI2&ME2		181.25	107.89
MI3&ME3		-237.5	-451.90
MI4&ME4		-656.25	-15.70
MI5&ME5		-1075	-2323.87
MI6&ME6		-2000	-2000
MI7&ME7		-4000	-4000
Mirror DT		-2000	-2000

134

Table C.2: Time resolution, mass resolving power and voltage settings optimized for E = 9.14 V/mm, dX0 = dY0 = dZ0 = 0.60 mm, dKx0 = dKy0 = dKz0 = 0.050 eV. See voltage settings in Table C.4.

N_{laps}	T_{flight} [µs]	dT_{aber} [ns]	dT_{total} [ns]	M/dM	dT_{aber} [ns]	dT_{total} [ns]	M/dM
		dZ0=±0.60mm			dZ0=±0.80mm		
59	804.12	3.07	44.11	9115	5.33	44.32	9070
120	1603.01	4.07	44.19	18140	7.16	44.58	17980
240	3174	7.61	44.65	35540	15.03	46.50	34130
480	6314.52	20.01	48.34	65320	45.02	62.95	50150
720	9455	43.71	62.02	76220	110.71	119.14	39680
960	12595.3	69.05	81.88	76910	180.71	185.99	33860

Table C.3: Time resolution and mass resolving power at E = 7.26 V/mm. Initial beam parameters are as in Table C.2, voltage settings see in Table C.4.

N_{laps}	T_{flight} [µs]	dT_{aber} [ns]	dT_{total} [ns]	M/dM	dT_{aber} [ns]	dT_{total} [ns]	M/dM
		dZ0=±0.60mm			dZ0=±0.80mm		
59	804.24	19.71	58.80	6840	26.46	61.39	6550
120	1603.13	19.53	58.74	13650	26.28	61.32	13070
240	3174.12	18.78	58.50	27130	27.20	61.72	25720
480	6314.64	15.69	57.58	54830	32.28	64.12	49240
720	9455.12	26.21	61.29	77140	80.54	97.75	48360
960	12595.4	53.69	77.15	81630	171.8	180.5	34880

Table C.4: Voltage settings optimized for E = 9.14 V/mm and dX0 = dY0 = dZ0 = 0.60mm, dKx0 = dKy0 = dKz0 = 0.050 eV.

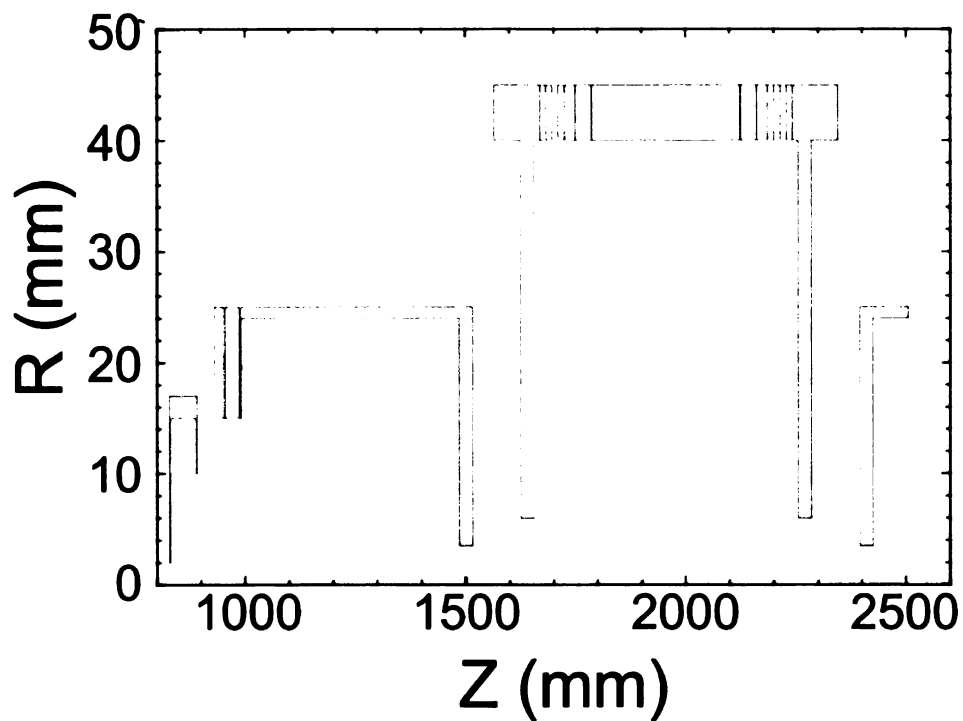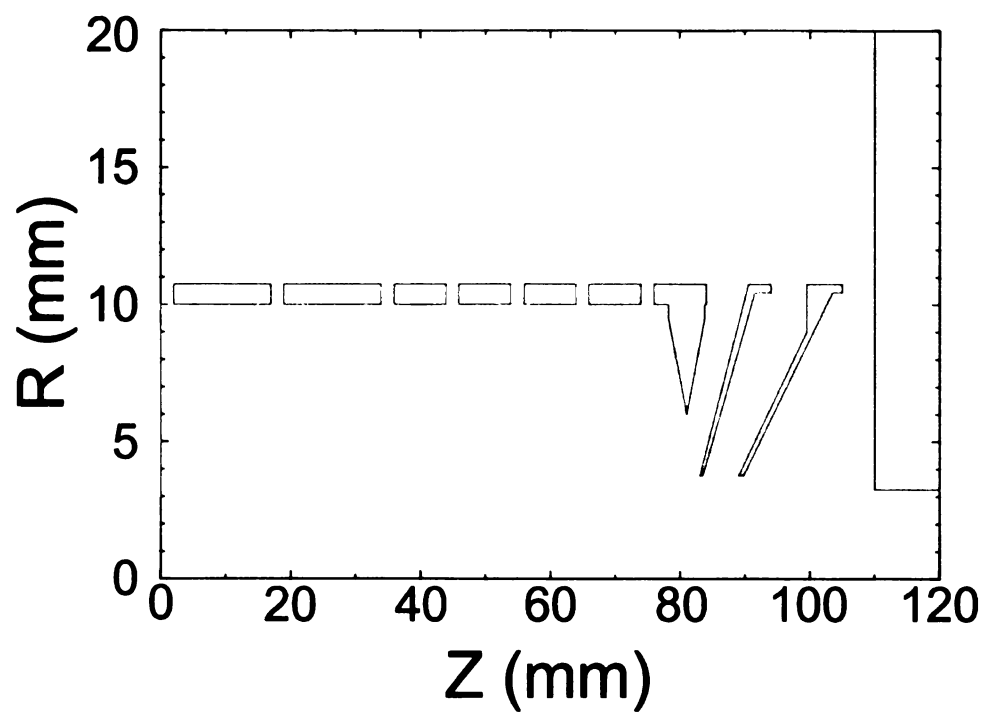| N_{laps}	T_{flight} [µs]	MI2 ME2	MI3 ME3	MI4 ME4	MI5 ME5
		[Volt]			
59	804.12	107.89	-451.903	-15.697	-2323.873
120	1603.01	98.817	-479.825	57.584	-2571.362
240	3174	88.843	-479.167	74.127	-2695.151
480	6314.52	75.48	-461.574	62.627	-2765.884
720	9455	75.038	-461.668	62.776	-2788.193
960	12595.3	74.962	-461.734	62.53	-2799.704

Figure C.3: Electrodes of the MTOF.

Figure C.4: Electrodes of the LEBIT buncher.

Bibliography

[1] B. A. Brown, R. R. C. Clement, W.A. Richter, et al. *Phys. Rev. C*, 65:045802, 2002.

[2] A. H. Wapstra, G. Audi, and C. Thibault. *Nucl. Phys.*, A729:337, 2003.

[3] D. G. Jenkins, N. S. Kelsall, C. J. Lister, et al. *Phys. Rev. C*, 65:064307, 2002.

[4] J. Savory, P. Schury, C. Bachelet, et al. *Phys. Lett. A*, 102:132501, 2009.

[5] P. Schury, G. Bollen, D.A. Davies, et al. *Phys. Rev. C*, 75:055801, 2007.

[6] J. A. Clark, G. Savard, K. S. Sharma, et al. *Phys. Rev. Lett.*, 92:192501, 2004.

[7] H. Schatz, A. Aprahamian, V. Barnard, et al. *Phys. Rev. Lett.*, 86:3471, 2001.

[8] G. F. Lima, A. Lépine-Szily, G. Audi, et al. *Phys. Rev. C*, 65:044618, 2002.

[9] A. Wöhr, A. Aprahamiana, P. Boutachkova, et al. *Nucl. Phys.*, A742:349, 2004.

[10] M. B. Gomez-Hornillos, M. Chartier, W. Mittig, et al. *Phys. Rev. C.*, 78:014311, 2008.

[11] M. Hausmann, J. Stadlmann, F. Attallah, et al. *Hyp. Int.*, 132:289, 2001.

[12] M. Chartier, W. Mittig, N. A. Orr, et al. *Nucl. Phys. A*, 637:3, 1998.

[13] B. E. Tomlin, C. J. Barton, N. V. Zamfir, et al. *Phys. Rev. C*, 63:034314, 2001.

[14] C.N. Davids. Proceeding 6th Inter. Conf. on Atomic Masses and Fund. Constants (AMCO-6), page 419, 1980.

[15] P. Wilhelms J. Oberheide and M. Zimmer. *Meas. Sci. Technol.*, 8:351, 1997.

[16] M . Galanti, R. Gott, and J. F. Renaud. *Rev. Sci . Instr.*, 42:1818, 1971.

[17] G. Carter and J. S. Colligon. *Ion bombardment of solids*. American Elsevier Pub. Co., 1968.

[18] L. A. Dietz and J. C. Sheffield. *J. Appl. Phys.*, 46:4361, 1975.

[19] E. Haseltine. *Discover Magazine*, 2:37, 2002.

[20] E. M. Burbidge, G. R. Burbidge, W. A. Fowler, and F. Hoyle. *Rev. Mod. Phys.*, 29:58, 1957.

[21] R.D. Hoffman, S.E. Woosley, G.M. Fuller, et al. *Astrophys. J.*, 460:478, 1996.

[22] N. N. Weinberg, L. Bildsten, and H. Schatz. *Astrophys. J.*, 639:1018, 2006.

[23] Ronald E. Taam. *Ann. Rev. Nucl. Part. Sci.*, 35:1, 1985.

[24] H. Schatz, A. Aprahamian, J. Görres, et al. *Phys. Rep.*, 294:167, 1998.

[25] O. Koike, M. Hashimoto, K. Arai, and S. Wanajo. *Astron. Astrophys.*, 342:464, 1999.

[26] W. H. G. Lewin, J. van Paradijs, and R.E. Taam. *Space Sci. Rev.*, 62:223, 1993.

[27] F. Ozel. *Nature*, 441:115, 2006.

[28] D. K. Galloway, D. Psaltis M. P. Muno, and D. Chakrabarty. *Astrophys. J.*, 639:1033, 2005.

[29] S. Gupta, E. F. Brown, H. Schatz, et al. *Astrophys. J.*, 662:1188, 2007.

[30] H. Schatz. *Int. J. Mass Spectrom.*, 251:293 – 299, 2006.

[31] A. S. Lalleman, G. Auger, W. Mittig, et al. *Hyp. Int.*, 132:315, 2001.

[32] J. A. Clark, K. S. Sharma, G. Savard, et al. *Phys. Rev. C*, 75:032801, 2007.

[33] C. Guénaut, G Audi, D. Beck, et al. *Phys. Rev. C*, 75:044303, 2007.

[34] D. Rodríguez, V.S. Kolhinen, G. Audi, et al. *Phys. Rev. Lett.*, 93:161104, 2004.

[35] T. Eronen, V. Elomaa, U. Hager, et al. *Phys. Lett. B*, 636:191–196, 2006.

[36] A. Rogers, M. A. Famiano, M. S. Wallace, et al. Experimental Exploration of [69]Br and the rp-Process [68]Se Waiting Point. *2008 APS April Meeting and HEDP/HEDLA Meeting.*

[37] D. Lunney, J.M. Peasron, and C. Thibault. *Rev. Mod. Phys.*, 75:1021, 2003.

[38] G. Bollen, D. Davies, M. Facina, et al. *Phys. Rev. Lett.*, 96:152501, 2006.

[39] R. Ringle, T. Sun, G. Bollen, et al. *Phys. Rev. C*, 75:055503, 2007.

[40] M. Smith, M. Brodeur, T. Brunner, et al. *Phys. Rev. Lett.*, 101:202501, 2008.

[41] W. Shi, M. Redshaw, and E.G. Myers. *Phys. Rev. A*, 72:022510, 2005.

[42] D.J. Morrissey, B.M. Sherrill, M. Steiner, et al. *Nucl. Instr. and Meth.*, B204:90, 2003.

[43] M. Block, C. Bachelet, G. Bollen, et al. *Phys. Rev. Lett.*, 100:132501, 2008.

[44] L. Weissman, P.A. Lofy, D.A. Davies, et al. *Nucl. Phys.*, A746:655c – 658c, 2004.

[45] S. Schwarz, G. Bollen, D. Lawton, et al. *Nucl. Instr. and Meth.*, B204:474, 2003.

[46] Ryan Ringle. *Design of LEBIT Penning Trap and Mass Measurement of ^{38}Ca.* PhD thesis, Michigan State University, 2006.

[47] R. Ringle, G. Bollen, A. Prinke, et al. *Nucl. Instr. and Meth. A*, 604:536, 2009.

[48] M. König, G. Bollen, H.-J. Kluge, et al. *Int. J. Mass Spectrom. Ion. Procress*, 142:95, 1995.

[49] G. Bollen, R. B. Moore, G. Savard, and H. Stolzenberg. *J. Appl. Phy.*, 68:4355–4374, 1990.

[50] R. Ringle, P. Schury, T. Sun, et al. *Int. J. Mass Spectrom.*, 251:300, 2006.

[51] Tao Sun. *High Precision Mass Measurments of ^{37}Ca and Developement for LEBIT.* PhD thesis, Michigan State University, 2006.

[52] H. Weick, H. Geissel, C. Scheidenberger, et al. *Nucl. Instr. and Meth. B*, 164-165:168, 2000.

[53] L. Weissman, D. A. Davies, P. A. Lofy, and D. J. Morrissey. *Nucl. Instr. and Meth. A*, 531:416, 2004.

[54] Pete Schury. *High Precision Mass Measurements Near N=Z=33.* PhD thesis, Michigan State University, 2007.

[55] H.G. Dehmelt. *Advan. At. Mol. Phys.*, 3:53, 1967.

[56] P. H. Dawson, editor. *Quadrupole Mass Spectrometry and its Applications.* AIP Press, 1995.

[57] W. Paul and H. Steinwedel. *Z. Naturforsh. A*, 8:448, 1953.

[58] T Sun, S. Schwarz, G. Bollen, et al. *Eur. Phys. J. A*, 25, s01:61–62, 2005.

[59] P. Schury et al. *Hyp. Int.*, 173:165, 2006.

[60] G. Gabrielse and J. Tan. *J. Appl. Phys.*, 63:5143, 1988.

[61] R. Ringle, G. Bollen, A. Prinke, et al. *Int. J. Mass Spectrom.*, 263, 2007.

[62] N. Daly. *Rev. Sci. Instrum.*, 31:264, 1960.

[63] R.S. Brown and G. Gabrielse. *Rev. Mod. Phys.*, 58:233, 1986.

[64] G. Bollen, S. Becker, H.-J. Kluge, et al. *Nucl. Instr. and Meth. A*, 368:675, 1996.

[65] G. Bollen, H.-J. Kluge, M. König, et al. *Phys. Rev. C*, 46:R2140, 1992.

[66] G. Graff, H. Kalinowsky, and J. Traut. *Z. Phys. A*, 297:35, 1980.

[67] R. Ringle, G. Bollen, P. Schury, et al. *Int. J. Mass Spectrom.*, 262:34, 2007.

[68] G. Gabrielse. *Int. J. Mass Spectrom.*, 279:107, 2009.

[69] A. Piechaczek, E. F. Zganjar, J. C. Batchelder, et al. *Phys. Rev. C*, 62:054317, 2000.

[70] B. Vosicki, T. Bjornstad, and L. C. Carraz. *Nucl. Instrum. Methods*, 186:307, 1981.

[71] G. Audi and A. H. Wapstra. *Nucl. Phys. A*, A565:1, 1993.

[72] D.S. Brenner, C. Wesselborg, R.F. Casten, et al. *Phys. Lett. B*, 243:1, 1990.

[73] P. Van Isacker, D.D. Warner, and D. S. Brenner. *Phys. Rev. Lett.*, 74:4607, 1995.

[74] E.P. Wigner. *Phys. Rev.*, 51:106, 1937.

[75] T. Rauscher and F.-K. Thielemann. *At. Data Nucl. Data Tables*, 75:1, 2000.

[76] S. E. Woosley, A. Heger, A. Cumming, et al. *Astrophys. J. Suppl. Ser.*, 151:75, 204.

[77] J. L. Wiza. *Nucl. Instr. and Meth.*, 162:587, 1979.

[78] D. A. Dahl. *Int. J. Mass Spectrom.*, 200:3, 2000.

[79] L. A. Dietz and J. C. Sheffield. *Rev. Sci. Instrum.*, 44:183, 1975.

[80] S. Schwarz. *Manipulation of Radioactive Ion Beams using a Paul Trap and Direct Mass Measurements of Neutron-Deficient Mercury Isotopes at the ISOLTRAP-Experiment.* PhD thesis, Fachbereich Physik der Johannes Gutenberg-Universitat, 1998.

[81] R. J. Cotter. *Time-of-Flight Mass Spectrometry.* American Chemical Society, 1997.

[82] W. C. Wiley and I. H. McLaren. *Rev. Sci. Instrum.*, 26:1150, 1955.

[83] R. B. Moore, A. M. Ghalambor Dezfuli, P. Varfalvy, and H. Zhao. *Physica Scripta.*, T59:93, 1995.

[84] A. Casares, A. Kholomeev, H. Wollnik, et al. *Int. J. Mass Spectrom.*, 206:267, 2000.

[85] A. Piechaczek, V. Shchepunov, H. K. Carter, et al. *Nucl. Instr. and Meth. B*, 266:4510, 2008.

[86] Y. Ishida, M. Wada, Y. Matsuo, et al. *Nucl. Instr. and Meth. B*, 468:219, 2004.

[87] W. R. Plass, T. Dickel, M. Petrick, et al. *Nucl. Instr. and Meth. B*, 219:4560, 2008.

[88] B. A. Mamyrin. *Int. J. Mass Spectrom.*, 206:251, 2000.

[89] V. A. Shchepunov and H. Wollnik. Non-linear beam dynamics in high resolution multi-pass time of flight mass seperator. In *Prooceedings of 2005 Particle Accelerator Conference*, 2005.

[90] V. A. Shchepunov and A. Piechaczek. private communication.

[91] J. Hardy and I. Towner. *Phys. Rev. C*, 71:055501, 2005.